MODELING FIBER DAMAGE DURING PROCESSING OF LONG FIBER-REINFORCED THERMOPLASTIC COMPOSITES

by

Abrahan Bechara Senior

A dissertation submitted in partial fulfillment of
the requirements for the degree of

Doctor of Philosophy

(Mechanical Engineering)

at the

UNIVERSITY OF WISCONSIN–MADISON

2021

Date of final oral examination: 05/03/2021

The dissertation is approved by the following members of the Final Oral Committee:

Tim A. Osswald, Professor, Mechanical Engineering
Lih-Sheng (Tom) Turng, Professor, Mechanical Engineering
Pavana Prabhakar, Assistant Professor, Civil and Environmental Engineering
Alejandro Roldán-Alzate, Assistant Professor, Mechanical Engineering
Lianyi Chen, Assistant Professor, Mechanical Engineering

© Copyright by Abrahan Bechara 2021

All rights reserved

Abstract

When processing long fiber-reinforced thermoplastics, the length of the fibers decreases inevitably, which ultimately affects the mechanical performance of the finished part. Since few modeling techniques can accurately predict fiber damage during injection molding, a new approach for modeling this phenomenon is presented. First, fiber failure is characterized, and the material's strength distribution is quantified. Then, multiple controlled studies are performed to determine correlations between processing conditions, material properties, and fiber length reduction. As approximately 50% of the total damage occurs during melting, the kinetics of fiber damage in conjunction with dispersion are explored. Based on the findings, fiber failure is modeled using solid mechanics in combination with an approximation of Stokes' Law. Fiber-fiber interactions are accounted for and correlated with the fiber volume fraction via fitting of experimental data. The finished model is implemented as a post processing tool for injection molding simulations using COMSOL Multiphysics.

Acknowledgements

First, I would like to express my gratitude to my advisor Prof. Tim A. Osswald for his continuous motivation, and immense knowledge. Without his guidance I would have not been able to successfully reach this goal. I also would like to express my great appreciation to Prof. Pavana Prabhakar, Prof. Lih-Sheng (Tom) Turng, Prof. Alejandro Roldan, and Prof. Lianyi Chen for serving on my dissertation committee and for their continuous advice.

I want to express my appreciation to all undergraduate students that I mentored throughout my research work and who assisted with various aspects of this project, including Taylor Anderson, Amber Westlund, James Sitter, Deshan Cai, Michael Tuchler, Saivya Chauhan, Garrett Gueltzow, Farlod Diaz, Ameya Kulkarni and Elizabeth Gardner. I would like to thank all current and former members of the Polymer Engineering Center that made my time here an unforgettable experience. In particular, I want to thank Roberto Monroy, Camilo Perez, John Puentes and Fred Montero.

In addition, I would like to thank my current and former fellow graduate students in the "Fibers Group" who I worked closely with, including Sebastian Goris, Andres Tapia, Ian Walter, Tina Chang, Hakan Celik, Camila Montoya and Kelsey Hacker. I would like to express my most sincere gratitude to Sara Simon, Allen Roman and Hector Perez who helped with critical feedback, discussions of ideas and collaborations in the field of fiber-reinforced composites.

Most importantly, I would like to thank my family, who gave me unconditional support and infinite love during this challenging journey.

Table of Contents

Abstract……...i

Acknowledgements……..ii

Table of Contents……iii

List of Figures v

List of Tables viii

List of Abbreviations ix

List of symbols xi

1 Introduction 1

1.1 Long fiber-reinforced thermoplastics 2

1.2 Motivation and objectives 5

1.3 Structure and Scope 8

2 State of the Art 10

2.1 Fiber microstructure measurements 10

2.1.1 Micro CT analysis 10

2.1.2 Fiber Length 11

2.1.3 Fiber dispersion 13

2.2 Studies on Fiber breakage 14

2.3 Studies on fiber dispersion 18

2.4 Prediction of fiber damage 20

3 Fiber Breakage 27

3.1 Single fiber failure 27

3.2 Fiber attrition kinetics 36

3.2.1 Length decay over time 37

3.2.2 Steady state length 38

3.2.3 Attrition rate 39

3.3 Results 40

3.3.1 Length decay over time 40

3.3.2 Steady state length 41
3.3.3 Attrition rate 42
3.4 Fiber damage during dispersion 44
3.4.1 Impact on steady state length 44
3.4.2 Impact on attrition rate 47
3.5 Measuring fiber length through the thickness of molded components 50
3.5.1 Shell Extraction and Experimental Validation 52
3.5.2 Injection Molding Plaques 55
3.5.3 Microstructural Analysis 56
3.5.4 Comparison with Length Prediction Model 59
3.5.5 Impact on Stiffness 61
4 Modeling Fiber Damage 65
4.1 Model development 65
4.1.1 Equilibrium length 66
4.1.2 Breakage rate 68
4.1.3 Constitutive model 69
4.2 Model validation 74
4.3 Computational implementation 77
4.4 Conclusions 83
5 Summary 86
5.1 Recommendations for future work 87
5.2 Publications 88
6 References 89

List of Figures

Figure 1.1 Passenger car fuel economy, normalized to CAFE [1] 1
Figure 1.2 a) 1930 GM truck metallic dashboard b) 2018 McLaren 570s IM dashboard ... 3
Figure 1.3: Normalized mechanical properties as a function of fiber aspect ratio [3]. 4
Figure 1.4 Discontinuous fiber composite main microstructural variables and their interactions..... 6
Figure 1.5: LFT pellet fabrication process, a) Pultrusion process, b) Wire coating process. 7
Figure 1.6: Breakage and dispersion kinetics during plastication. 8
Figure 2.1 Overview of the steps of the employed fiber length measurement technique 13
Figure 2.2 Steps employed to measure fiber dispersion during plastication..... 14
Figure 2.3, Left: Fiber attrition mechanisms, Right: Attrition mechanisms and corresponding fiber length [48]..... 16
Figure 2.4: Fiber length reduction along the plastication unit [29]. 17
Figure 2.5: Cross section of fiber bundle showing the presence of voids [28]. 19
Figure 2.6 Compressive load on fiber on the onset of buckling under simple shear flow 20
Figure 2.7: Rotation orbits for fibers of varying flexibility [22]. 21
Figure 2.8 Illustration of expected fiber length reduction over time according to Shon's model..... 23
Figure 2.9: a) Center gated disk mold, b) Fiber length distribution at location B [19]. ... 24
Figure 3.1 Before and after fiber fracture, a) Knot test, b) Loop test 29
Figure 3.2 High speed recording set up for loop test 29
Figure 3.3 Loop failure photograph recorded at 1500fps a) Before rupture, b) After rupture 30
Figure 3.4 Loop test, a) Experiment set up, b) Captured loop image..... 31
Figure 3.5 Critical radius distribution resulting from the loop test, Weibull distribution fitted to experimental data (in red)..... 32
Figure 3.6 Large deformation simulation of glass fiber under bending load 34
Figure 3.7 Ultimate stress determined from the critical radius experiment 35
Figure 3.8. Illustration of the Couette rheometer setup for the study of fiber breakage. 37
Figure 3.9. μCT slice of fiber dispersion for different resident times. 39

Figure 3.10. Fiber length reduction over time for PPGF30 at 250°C..... 41
Figure 3.11. Outcome of the DOE for the steady state length showing the obtained weight-average fiber length LW, ∞ 41
Figure 3.12. Result of the statistical analysis showing main effect plots on LW, ∞..... 42
Figure 3.13. Outcome of experimental plan 3 showing the effect of shear rate on fiber attrition rate. 43
Figure 3.14. Average initial slope as a function of shear rate. 43
Figure 3.15 Schematic of the defined processing speed and residence time for fiber dispersion experiment 45
Figure 3.16 Measured residual fiber length for pre-dispersion and regular Couette runs 46
Figure 3.17 Fiber length distribution for pre-dispersion and regular Couette runs..... 47
Figure 3.18 Fiber breakage mechanisms under different dispersion stages a) Undispersed fiber bundles, b) Fully dispersed fibers 48
Figure 3.19 Illustration of the impact fiber dispersion has on length reduction over time in the Couette rheometer..... 49
Figure 3.20 Schematic of a core–shell structure..... 51
Figure 3.21 Sample preparation method for artificial core–shell plates..... 53
Figure 3.22 Artificial core–shell plate microstructure: (a) through-thickness fiber orientation distribution (FOD); and (b) fiber length values for individual core and shell layers 54
Figure 3.23 Illustration of the plaque geometry and illustration of the sample locations for microstructure analysis..... 56
Figure 3.24 Reconstruction of fiber structure from micro-computed tomography (μCT) analysis using VG StudioMAX: (a) 2-3 plane cross section; and (b) 1-2 plane section A-A 57
Figure 3.25 Injection molded plaque microstructure: (a) through-thickness FOD; and (b) through-thickness fiber content (FC)..... 58
Figure 3.26 Experimentally determined through-thickness fiber length distribution (FLD) for the injection molded plaque. Dashed lines show global fiber length measured over the whole part's thickness..... 59
Figure 3.27 Comparison of experimental and predicted through-thickness FLD..... 61
Figure 3.28 Aspect ratio distribution for the global sample, and the core and shell regions..... 63
Figure 3.29 Stress–strain curves for representative volume element (RVE) with global fiber length and with varying fiber length. 64
Figure 4.1. Illustration of a fiber experiencing distributed load due to drag force..... 67

Figure 4.2. Average parameter λ as function of fiber concentration 68
Figure 4.3. Result of the statistical analysis showing main effect plots on kf 69
Figure 4.4 Cumulative probability distribution functions compared to experiments fiber length, part 1 71
Figure 4.5 Cumulative probability distribution functions compared to experiments fiber length, part 2 72
Figure 4.6 Comparison between target LN and recovered LN for various PDFs 72
Figure 4.7 Comparison between target LW and recovered LW for various PDFs 73
Figure 4.8 Loss function comparison for various PDFs versus experimental data 73
Figure 4.9 Fiber length decay for experiment employing the Couette rheometer and fiber breakage model 75
Figure 4.10 Recovered fiber length distribution employing Burr PDF versus experimental distribution 76
Figure 4.11 3D view of partial filling of center gated disk 77
Figure 4.12 Left, 2D view of partial mold filling. Right, average fiber length along mold cavity 79
Figure 4.13 Illustration of the plaque geometry and illustration of the sample locations for fiber length analysis 80
Figure 4.14Fiber length measured along the mold cavity 81
Figure 4.15 Left, μCT orientation analysis. Right, boundary condition for fiber breakage model 82
Figure 4.16 Fiber length surface plot for mold filling sequence 82
Figure 4.17 Average fiber length as function of filling time for location A, B and C 83

List of Tables

Table 2.1 Overview of fiber length measurement via micro-computed tomography (μCT) in recently published studies 11
Table 3.1 Glass fiber properties 27
Table 3.2. Experimental plan1: Length decay over time 38
Table 3.3. Experimental plan 2: Impact of process variables on equilibrium length 38
Table 3.4. Experimental plan 3: Impact of shear and fiber concentration on attrition rate. 40
Table 3.5 Fiber breakage rate comparison between dispersed and undispersed fibers .. 48
Table 3.6 Average fiber length of compression molded plates 54
Table 3.7 Processing conditions for injection molding (IM) trials 55
Table 3.8 Input values for Phelps–Tucker model parameters 60
Table 3.9 Longitudinal and transverse Young's modulus for the core and shell layers . 63
Table 4.1 Evaluated probability distribution function parameters and their role 71
Table 4.2 Processing conditions for Couette experiment 74
Table 4.3 Processing conditions for injection molding (IM) simulation 78

List of Abbreviations

2D	Two Dimensional
3D	Three-Dimensional
μCT	Micro-Computed Tomography
CAFÉ	Corporate Average Fuel Economy standards
CFC	Continuous Fiber Composites
CLD	Cumulative Length Distribution
DOE	Design of Experiments
FC	Fiber Concentration
FLD	Fiber Length Distribution
FOD	Fiber Orientation Distribution
GF	Glass fibers
GM	General Motors
LFT	Long-Fiber Thermoplastic Composites
mpg	Miles Per Gallon
OEM	Original Equipment Manufacturer
PA	Polyamide
PBT	Polybutylene Terephthalate
PC	Polycarbonate
PC	Polycarbonate
PDF	Probability Density Function
PET	Polyethylene Terephthalate
PP	Polypropylene
PPA	Polyphthalamide
PPGF20	20 wt% Fiber-Reinforced PP

PPGF30	30 wt% Fiber-Reinforced PP
PPGF40	40 wt% Fiber-Reinforced PP
PPS	Polyphenylene Sulfide
PS	Polystyrene
PTFE	Polytetrafluoroethylene
ROI	Region of Interest
RPM	Rotations per Minute
RVE	Representative Volume Element
SFT	Short Fiber Thermoplastic Composites
SPR	Sliding Plate Rheometer
UV	Ultraviolet
UW-Madison	University of Wisconsin-Madison
wt%	Weight Percent

List of symbols

Symbol	Meaning
L	Fiber Length
D	Fiber Diameter
L_∞	Equilibrium fiber length
L_N	Number-Average Fiber Length
L_W	Weight-Average Fiber Length
N_i	Number of Fibers of Length i
l_i	Fiber length i
m_0	Weighted Fiber Population after Matrix Burn-Off
m_1	Weight of Fiber Bundles
ε	Fiber Dispersion
$\dot{\gamma}$	Shear rate
η	Viscosity
E_f	Young's Modulus
k_f	Fiber Breakup rate constant
F_{crit}	Critical Buckling Force
$\dot{\gamma}_{crit}$	Critical Flow Regimen
ζ	Fiber Drag Coefficient
C_B	Fiber Breakage Coefficient
S	Shape Factor
η_m	Matrix Viscosity
η_s	Suspension Viscosity
Bi	Buckling number
P_i	Probability of fibers breaking

R_{ik}	Probability of daughter fibers
N_k	Number of Fibers of Length k
B_u	Dimensionless Buckling Number
C_i	Isotropic Rotary Diffusion Parameter
σ_h	Hydrodynamic stresses
σ_c	Cohesive stress
σ	Normal stress
α	Shape parameter for Weibull
β	Scale parameter for Weibull
r_{crit}	Critical Radius of Curvature
r_d	Fiber Cross-Sectional Radius
I	Moment of Inertia
F	Force
θ	Inclination
Ω	Rotational speed
T	Torque
t	Time
s	Seconds
ϕ_K	Fiber Content
A_{11}	Fiber Orientation tensor in flow direction
A_{22}	Fiber Orientation tensor in crossflow direction
A_{33}	Fiber Orientation tensor in thickness direction
$\mathbf{E_{11}}$	Stiffness component in direction 1
$\mathbf{E_{22}}$	Stiffness component in direction 2
w	Distributed load
U_o	Uniform Speed
σ_{max}	Maximum Hydrodynamic Stress

d_f	Fiber Diameter
σ_{ut}	Ultimate strength
h	Characteristic Distance
λ	Dimensionless parameter for interactions
ξ	Fitting parameter for breakage rate
∇	Divergence operator
L_0	Initial Fiber Length
L_{ub}	Unbreakable Length
k	Breakage Rate Coefficient?
t_R	Residence Time
vf	Volume Fraction

1 Introduction

The use of polymer composites has been rapidly increasing in the automotive industry over the past decades; mainly due to a market push for more fuel-efficient vehicles, regulatory changes, and the advent of e-mobility. The passenger fuel economy historical performance has been steadily rising since the 1990s and it seats at a global average of 40 miles per gallon (mpg) as of May 2020. Nevertheless, regulatory zones have ever increasing standards for automakers; Europe for example aims to reach 81mpg by 2030 (Figure 1.1). Improvement of the engine's efficiency, reduction of mechanical losses and light weighting are all methods for increasing fuel efficiency. The latter has been the driver for much of the technological development and research advancement in the field of polymer composites. Automakers, OEMs, and material suppliers have spent quartzous amounts of time and resources improving the performance and reducing the cost of components manufactured with this type of materials.

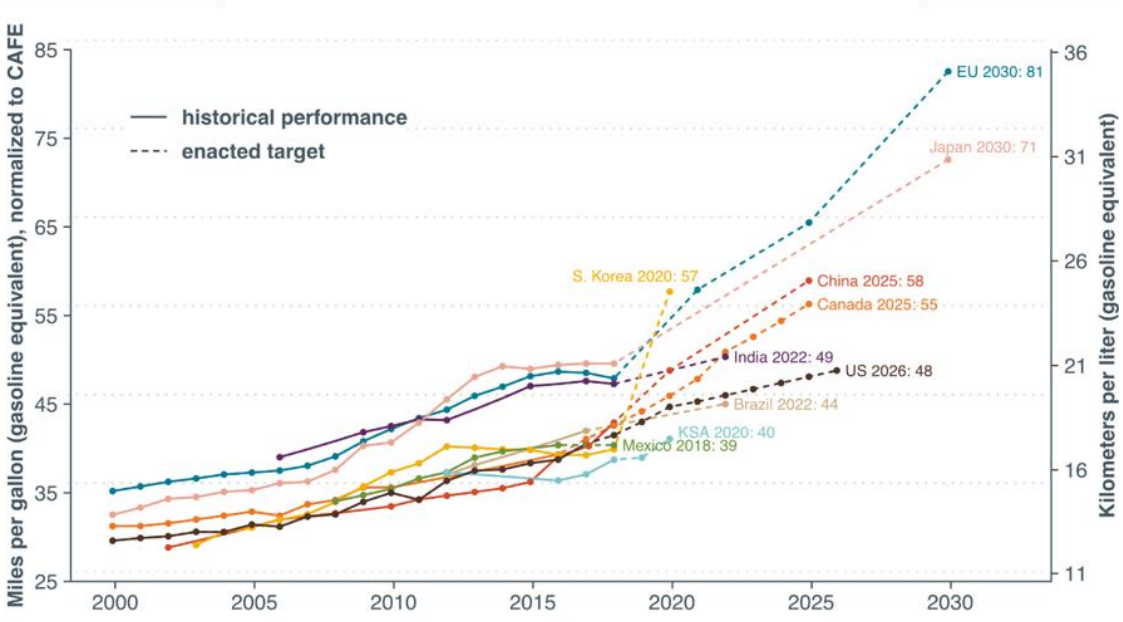

Figure 1.1 Passenger car fuel economy, normalized to CAFE [1]

For polymer composites, the properties of the bulk material depend on three main factors: the individual properties of its constituents, the bonding between them and their arrangement in the finished part [2]. While continuous fiber composites (CFC) show the greatest improvement in material properties compared to the neat matrix material, such improvement is offset by the slow production cycle times and high manufacturing costs. Short fiber thermoplastic composites (SFTs) on the other hand can be injection molded, a process which reduces cycle times and cost when compared with CFC production methods, while allowing for increased part complexity. Compared to the neat polymer, SFTs exhibit increased stiffness, strength and decreased thermal expansion. However, these materials do not offer the same material property improvements as their continuous-fiber counterparts [3]. Long-fiber thermoplastic composites (LFTs) bridge the gap between short- and continuous-fiber thermoplastic composites, offering better mechanical properties than SFTs, while retaining the ability to be injection molded [4].

1.1 Long fiber-reinforced thermoplastics

LFTs were first developed in the mid-1980s by the Imperial Chemical Industries of the United Kingdom under the trade name of Verton, and initially consisted of a PA66 matrix reinforced with 30% weight of glass fibers 10 mm in length [5]. While the most common reinforcing material for LFTs is glass, carbon fiber has also been used [4,18,19]. Carbon fibers might offer superior properties, however, the cost increase does not justify their use as a replacement for glass at this point [8]. The matrix material for LFTs is an engineering thermoplastic, most commonly PP or PA. Still, other engineering thermoplastics have been used: PP [21,22], PET and PBT [11], PPA, PC, PPS and blends of PC or PA66 with PTFE [12]. The introduction of this particular composite technology has allowed for great leaps in weight reduction and feature complexity. To illustrate this, Figure 1.2 shows the stripped dashboard of a 1930 GM truck and a 2018 McLaren 570s.

The addition of electronic controls and various amenities has pushed designers to create components with increasing geometrical complexity, making injection molding the go to technology for manufacturing them.

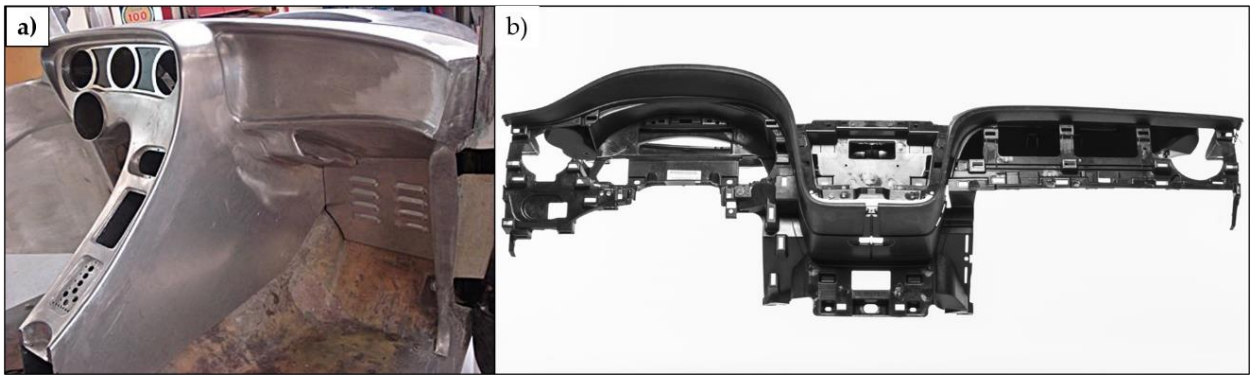

Figure 1.2 a) 1930 GM truck metallic dashboard b) 2018 McLaren 570s IM dashboard

However, with discontinuous fibers composites (LFTs and SFTs) the injection molding process restructures the arrangement of the reinforcing fibers in the finished part [2-5]. This arrangement is characterized by three important microstructural variables: fiber orientation distribution (FOD), fiber length distribution (FLD), and fiber content (FC) [14]. Since LFTs' main advantage is the high aspect ratio of their fibers, a main concern for manufactures is preserving this length throughout the molding process.

When processing LFTs it is important that glass fibers be well dispersed but retain a high aspect ratio, as the mechanical properties of discontinuous fiber composites depend upon the transferal of stresses from the matrix to the glass fibers [1,2,4]. If a fiber's aspect ratio (L/D) goes much below the critical aspect ratio [13], they run the risk of becoming harmful to the composite's integrity. This is because fiber end faces can act as stress concentrators since they are often de-bonded on account of not being covered by the sizing [15].

Thomason et al., conducted extensive studies on the relationship between fiber structure and mechanical properties and published their work between 1996 [16] and

2009 [17]. Their results suggest that the modulus of the composite plateaus when L/D approaches 50, while other properties such as tensile strength and impact strength can still grow with fiber length and plateau much later when L/D reaches values of 400 and 1000, respectively. Schemme et al. summarized Thomason's work on a graph of some normalized mechanical properties as a function of fiber aspect ratio (Figure 1.3) [3]. Schemme's graph only provides a qualitative picture of the relationship between fiber aspect ratio and mechanical properties, since a universal validity has not been proven yet. One reason being Thomason's experimental data does not consider process induced variations of orientation or volume fraction based on the change in aspect ratio.

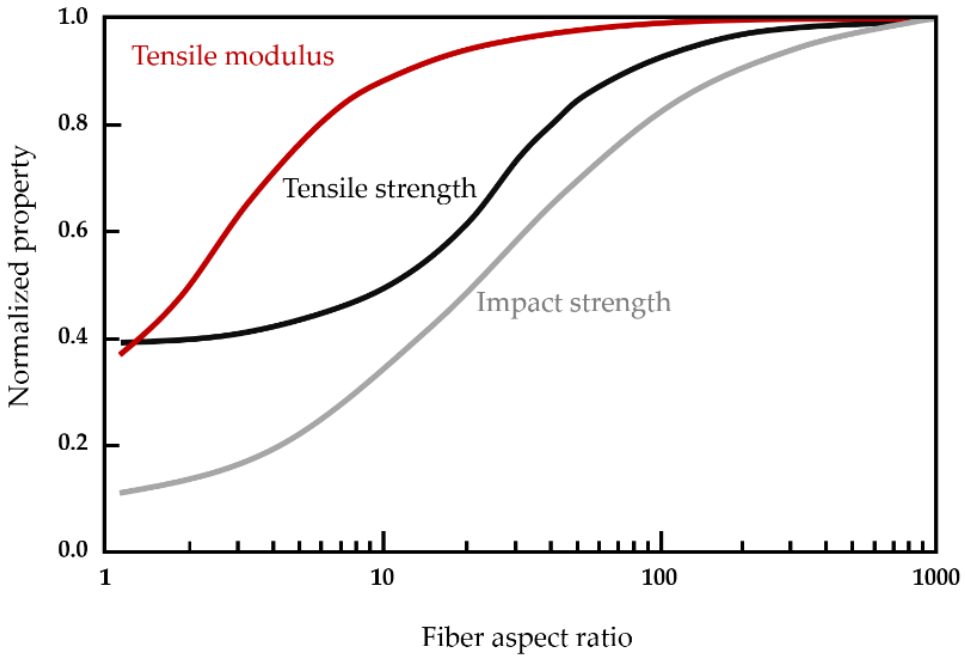

Figure 1.3: Normalized mechanical properties as a function of fiber aspect ratio [3].

The changes in microstructure introduce a critical initial step in the design stages: accurately predicting the microstructure from processing conditions and materials properties. This approach is commonly referred to as simulation chain, which couples manufacturing and structural mechanical simulations.

1.2 Motivation and objectives

While the development of anisotropy and the reduction of fiber length are major factors that determine the mechanical properties and the dimensional stability of an injection molded component, only the first one has been comprehensibly described and, to a certain extent, successfully modeled [3]. In the case of length reduction, up until 2010 most literature provided ample anecdotal evidence for the relationship between processing conditions and fiber damage. However, few models with quantitative prediction capabilities were presented. Shon et al., provided an empirical relation for compounding devices in which an average fiber length L decreases toward an equilibrium value L_∞ following an exponential decay function; though no explanation was given on how to predict the model parameters [18].

Only in 2013, a model was presented by Phelps et al., which considered mechanical and phenomenological arguments to predict fiber length degradation in the mold cavity [19]. This model has been adopted as the standard approach and implemented by most commercial software companies. The model is developed under two main premises: 1) Fibers break due to buckling caused by compressive hydrodynamic stresses, 2) Fiber length degradation has negligible dependence on fiber volume fraction.

Recent studies in which fibers were processed under controlled conditions have shown there is a strong relationship between volume fraction and fiber damage [9-10]. Additionally, in the case of LFTs (focus of this work) literature shows that fiber breakage is the result of distributed bending loads causing large deformations, state that can hardly be achieved in buckling [22]. Much of the complexity in modeling either of the microstructural variables lies in the fact that they are inter-related at all times; furthermore, each microstructural variable affects the suspension rheology which in turn affects the flow behavior during processing. Many studies have been conducted on such

interrelations [23,24]; Figure 1.4 summarizes the main interactions between microstructural variables observed during processing.

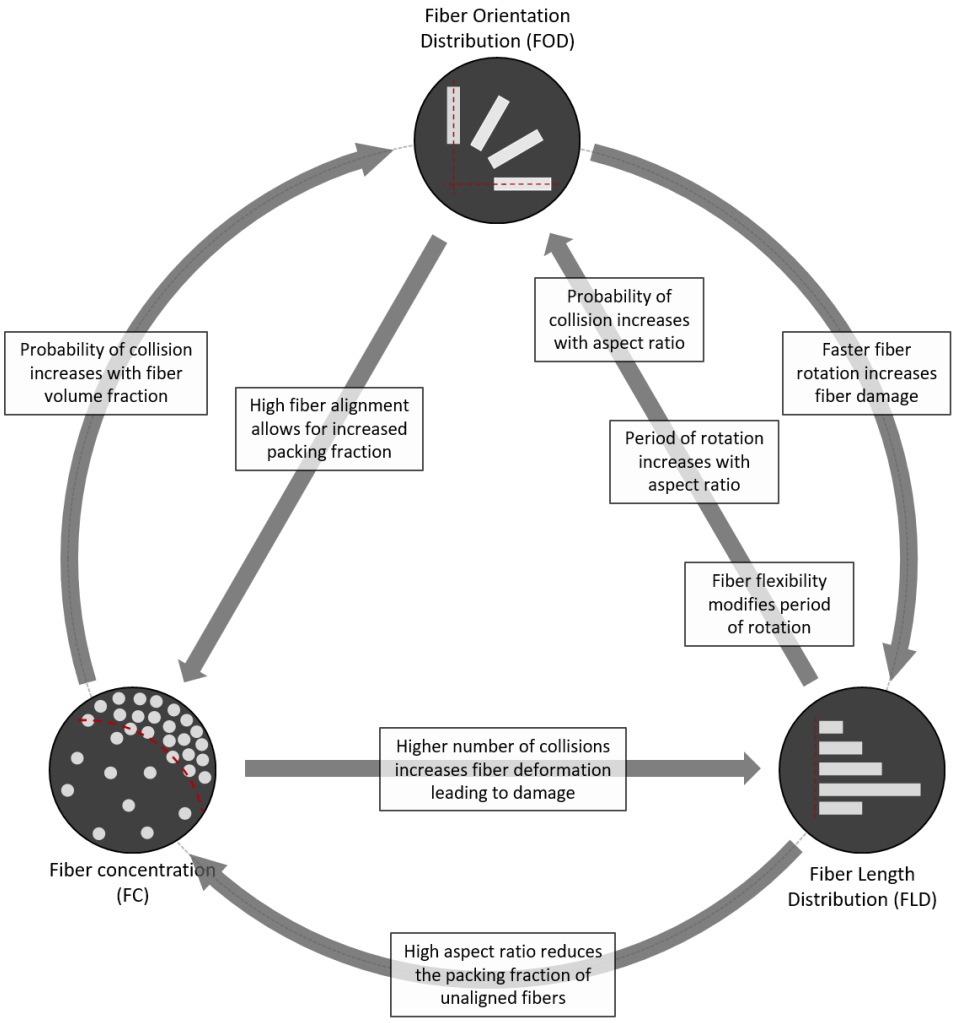

Figure 1.4 Discontinuous fiber composite main microstructural variables and their interactions

The ability to predict fiber damage, based on processing conditions and material qualities is required for describing the thermomechanical properties of the bulk material, which in turn are needed for structural analysis. While simulation is a great tool which offers support in these stages of the design process, it is crucial that reasonable modeling approaches are chosen and that the simplifying assumptions are permissible [25]. Considering the findings of recent studies on fiber attrition, we develop a new approach for modeling fiber length degradation [9-10]. One that considers the effect of fiber-fiber

interactions (volume fraction) and is based on a more precise mechanical description of fiber breakage.

Much of the work done to investigate and model the effects of processing on fiber orientation and length degradation focuses on the effect of flow fields upon the suspension of individual fibers [3,13,14]. Comparatively, little work has been done focusing on the transition of fiber bundles into a suspension of individual fibers [28]. This poses an additional complexity for the study of LFTs since the pellet manufacturing method leaves fibers bundled up surrounded by the polymer matrix. LFT pellets are produced either by pultrusion or a coating process. Pultruded LFT pellets are manufactured by pulling 20-40 thin rovings of fibers through a pultrusion die (Figure 1.5Figure 1.5, a). The extrudate is cooled, dried, and cut; resulting in a pellet with small bundles of fibers distributed over the entire cross section. For coated LFT pellets a single large roving, with around 3000 fibers, is first impregnated with wax, then pulled through a die in a 'wire coating' fashion. This process usually includes a sizing die to maintain the circular shape. In the final pellet, the unimpregnated fibers gather in a large bundle in the center of the cross section (Figure 1.5, b).

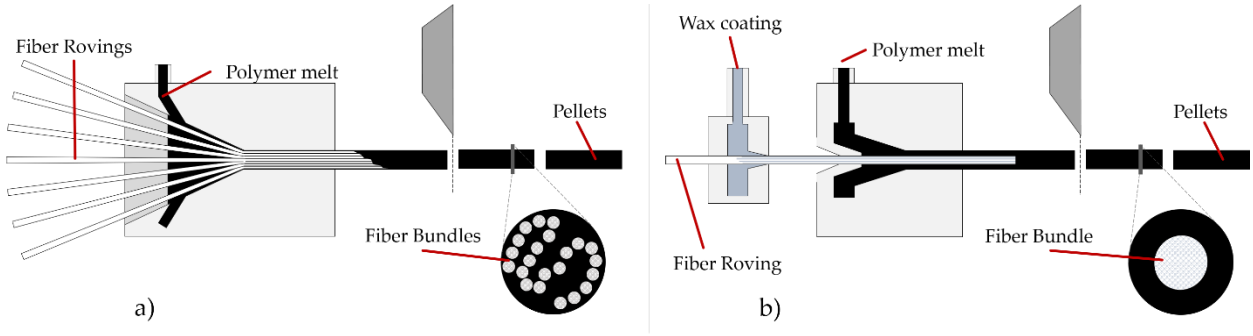

Figure 1.5: LFT pellet fabrication process, a) Pultrusion process, b) Wire coating process.

While pultrusion achieves greater fiber impregnation than coating, both types of pellets require a specific amount of strain to transition into a disperse suspension; strain which mainly occurs during melting in the plastication unit (Figure 1.6, bottom) [28].

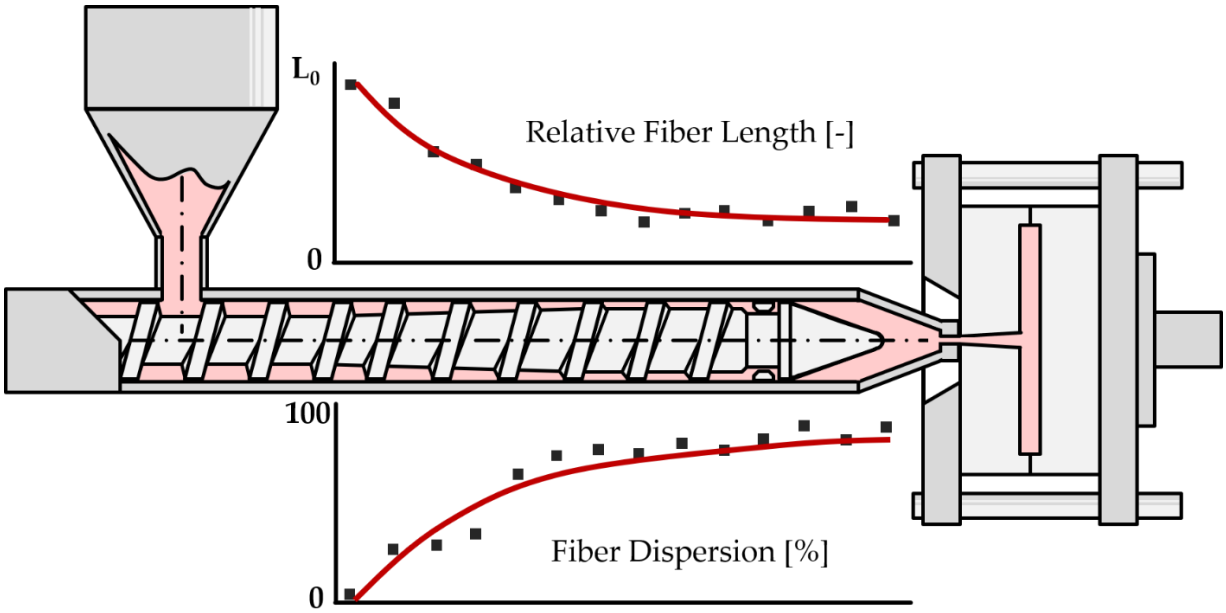

Figure 1.6: Breakage and dispersion kinetics during plastication.

Figure 1.6, top, illustrates the extent of damage sustained by the fibers through the injection molding process of long glass fiber-reinforced thermoplastics. Starting with an initial length of 10-20 mm, fiber attrition causes a degradation of the fiber length down to 50% of the initial length in the plastication unit. In the purged material, the fiber length can be less than 40% of the initial length and, ultimately, the length in the molded part can be reduced to less than 20% [16,17]. The region with the highest rate of breakage coincides with the transition from the heterogeneous mix of polymer and fiber bundles to a suspension of individual fibers. This fact compels us to consider how fiber dispersion might impact damage.

1.3 Structure and Scope

Since the fiber damage phenomena are fundamentally caused by competing internal forces and external stresses, the general approach to modeling it, will be the following. First, the unit of analysis will be studied and the internal characteristics which play a role

in the phenomena will be quantified. Second, experimental investigations on how the flow interacts with the unit of analysis will be conducted to obtain a comprehensive view of the kinetics of each process. Finally, expressions relating the kinetics and unit will be proposed and validated.

When modeling fiber attrition the unit of analysis is the fiber, and the objective is predicting the change in its length as it breaks due to hydrodynamic stresses. To achieve this, the following approach will be taken:

i. The fiber's critical curvature prior to failure will be measured via loop test. The resulting curvature data will be used to determine the fiber's ultimate strength.
ii. Fiber length reduction over time data will be obtained employing a Couette rheometer to impose a simple shear flow on the filled polymer. These experiments are designed to isolate effects that are encountered in the processing of LFTs.
iii. A mathematical model to describe the phenomenological trends will be proposed and mechanical arguments will be presented to explain the model parameters. Additional Couette experiments will be used to evaluate the model's performance.
iv. Finally, a flow solver (COMSOL Multiphysics) will be used in conjunction with the model to predict fiber length reduction during mold filling.

Much of the planned work requires the development of new measurement techniques specifically tailored for LFTs and the variables being modeled. Therefore, when necessary, these methods will be presented and validated before using them in the experimental studies.

2 State of the Art

2.1 Fiber microstructure measurements

The performance of a discontinuous fiber reinforced components depends on the microstructure developed during processing. Quantifying the microstructure is indispensable for understanding the process-microstructure relationship. In this section, the most commonly used method for fiber characterization will be presented.

2.1.1 Micro CT analysis

To understand the changes in fiber configuration and predict filler properties, first the fiber microstructure needs to be fully characterized. Through-thickness FOD and FC have great impact on the mechanical properties and thermal behavior of molded products. Until recently, the determination of FOD involved physically sectioning the sample and analyzing the cross section via optical microscopy [31]. In the analyzed cross section, fibers are seen as ellipses and fiber orientation is quantified by measuring the aspect ratio and inclination of the ellipse's major axis. Similarly, FC has been obtained by quantifying the area fraction of the cross section covered by fibers. Alternatively, through-thickness FC can also be determined by milling thin layers and quantifying the fiber weight fraction via pyrolysis [32].

μCT technology has gained traction as a method to obtain FOD and FC in a fast and accurate way; it is a non-destructive testing method based on X-ray imaging to inspect the internal structure of a sample. The X-ray projections are used to reconstruct the scanned sample in 3D, after which an analysis is performed to obtain through thickness values of fiber volume fraction and second-order orientation tensor components.

2.1.2 Fiber Length

Although modern measurement techniques can accurately capture the local changes in FOD and FC through the thickness of molded parts [32, 33], current techniques to measure FLD for LFTs are limited to reporting the global fiber length over the whole part's thickness. Various studies have reported FLD measurements via μCT (Table 2.1); but as high resolution is needed to differentiate individual fibers (four voxels per fiber diameter [34]), the size of the evaluated volume is limited to a few millimeters. Yet, parts molded with LFTs can still have fibers in the 10–15 mm range [35–37], far longer than what can be capture with μCT.

Table 2.1 Overview of fiber length measurement via micro-computed tomography (μCT) in recently published studies

Material	Sampled size	Voxel size (μm)	Max fiber length detected (μm)	Reference
PP-GF	138 × 413×129 μm^3	8.73	7000	Teßmann et al.[38]
PP-GF20	Ø 4 × 1.5 mm^3	3	4000	Pinter et al.[39]
PP-GF1	4 × 2 × 2 mm^3	2	1650	Salaberger et al.[40]
Wood fiber-lignin	4 × 2 × 2 mm^3	2.4	4000	Miettinen et al.[41]
PP-GF24	1.5 mm thick	2	1000	Köpplmayr et al.[42]
PA66-GF35	1255×1343×1883 μm^3	1	1000	Hessman et al.[43]
PP-GF10-60	-	3	2000	Kastner et al.[44]

FLD data are often given as an average value. In the case of LFTs, to properly describe this type of distributions both the number- and the weight-average should be reported. Similar to the molecular weight distribution, the number-average fiber length L_N is expressed as

$$L_N = \frac{\sum N_i l_i}{\sum N_i}, \qquad 2.1$$

the weight-average fiber length L_W as

$$L_W = \frac{\sum N_i l_i^2}{\sum N_i}, \qquad 2.2$$

Measuring the fiber length for discontinuous fiber composites is a time-consuming task since even small samples contain millions of fibers [37]. As noted by Goris et al., the lack of consensus in techniques for measuring fiber length distribution in LFTs has slowed down the efforts for understanding process induced damage [45]. The Polymer Engineering Center at UW-Madison, has developed a fiber length measurement technique adapting features from various measurement methods, aiming to reduce the manual input [37]. It ensures reliable results by sampling 10.000 to 100.000 fibers and extracting at least three samples for each test condition. The main steps of the technique are depicted in Figure 2.1. A 30-mm diameter disk is cut out from the composite part and the matrix is removed via pyrolysis at 500°C for 2.0h. A representative subsample is extracted employing a variation of the epoxy-plug method described by Kunc [35], where UV curable resin is used instead of an epoxy. The subsample is carefully removed with tweezers and a second pyrolysis is performed to remove the resin. The loose fibers are dispersed inside a chamber using an ionized air stream and fall onto an optical glass sheet. The sheet with the fibers is scanned using a flatbed scanner (Epson Perfection V750 PRO; Seiko Epson Corporation, Nagano, Japan). The obtained digital image is optimized in Photoshop and analyzed using a Marching Ball algorithm based on the work of Wang [46]. The result is a FLD and its average values L_N and L_W.

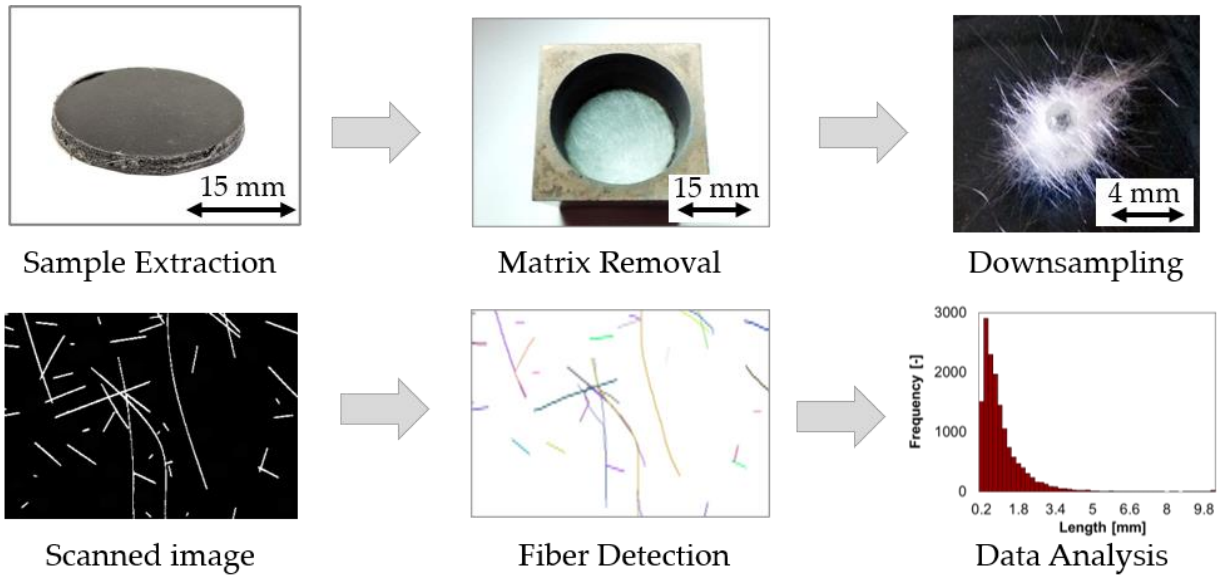

Figure 2.1 Overview of the steps of the employed fiber length measurement technique

The down sampling step is introduced for two reasons. First, even a small sample contains millions of fibers, processing and counting such quantity is cumbersome and based on Goris' study, unnecessary as a smaller subset yields the same results. Second, fibers at the boundary of the sample have been damaged in the extraction step and need to be removed. It is known that the down-sampling step skews the FLD since it preferentially captures longer fibers; thus, the Kunc correction is applied to the FLD data [35].

2.1.3 Fiber dispersion

Although dispersion traditionally refers to the change in filler concentration during mixing [47], in the case of LFTs dispersions refers to the deformation and breakup of fiber bundles into a suspension of individual fibers fully impregnated by the polymer melt. Most studies on the subject report a qualitative measurement of dispersion by counting the fraction of undispersed bundles after a certain amount of shearing [28, 48].

In their work Ren and Dai use a quantitative technique to measure dispersion [49]. After burning the matrix, the total fiber population is weighted and denoted m_0, the

sample is then placed onto a black optical- grade sheet and the fiber bundles are manually sorted out, the weight of the fiber bundles is denoted as m_1. Figure 2.2 illustrates the procedure.

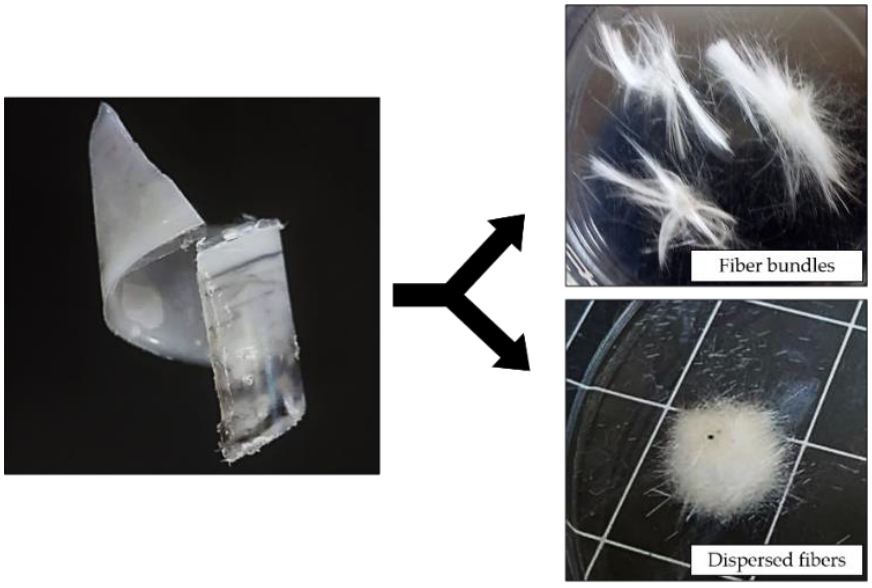

Figure 2.2 Steps employed to measure fiber dispersion during plastication

Fiber dispersion ε is the percentage of individual fibers present in the original sample and is determined following equation 2.3:

$$\varepsilon = \left(1 - \frac{m_1}{m_0}\right) \times 100\% \qquad 2.3$$

2.2 Studies on Fiber breakage

In 1983 von Turkovich et al., conducted compounding of SFTs experiments in a single screw extruder and found that most fiber length degradation occurred in the melting, with only minor attrition in the feed or the conveying zone [50]. They concluded that fiber breakage is a result of distributed bending loads deforming a fiber. These loads can result from hydrodynamic forces, or from interactions with neighboring fibers in more concentrated suspensions [50].

The fibers in LFTs initially have the length of the pellet, and while fibers may break during any stage of the injection molding process, Bailey et al., found that the most significant damage happens before the polymer melt enters the mold [9].

Following Bailey et al., findings most studies focused on examining fiber breakage as a function of processing parameters such as injection speed, screw back pressure, gate size, and nozzle design. Vu-Khanh et al., found that, of these parameters, only gate size had a clear influence on the fiber length in the finished part [11]. Their results also showed that matrix viscosity may have an influence in fiber attrition as moldings made with a PP matrix had average fiber lengths two to three times greater than with PA matrices.

Rohde et al. performed a full factorial DOE varying processing parameters such as injection speed, screw back pressure, holding pressure and screw speed.[51] Their results clearly show a strong influence of back pressure on fiber length. An increase in back pressure from 50 to 80 bar reduced the fiber length in the mold cavity by approximately 30%. The other individual factors had no statistically significant impact on fiber length. Nevertheless, the authors state that it is difficult to isolate the mechanisms that cause fiber attrition due to the complex phase change and shear history that is present in the injection molding process.

In 1994 Wolf pointed out the difference between compounding SFTs and plastication of LFTs [48]. He used a single screw extruder to process pultruded PA66 pellets (Verton) and studied fiber damage in the melting zone. He identified six fiber attrition mechanisms and their direct impact on the fiber length distribution (Figure 2.3). His results suggest that most severe damage occurs at the barrel interface and the trailing flight; fibers measured at these locations represented most of the lower values in the fiber length distribution. Damage in the melt pool was less severe leading to longer fibers.

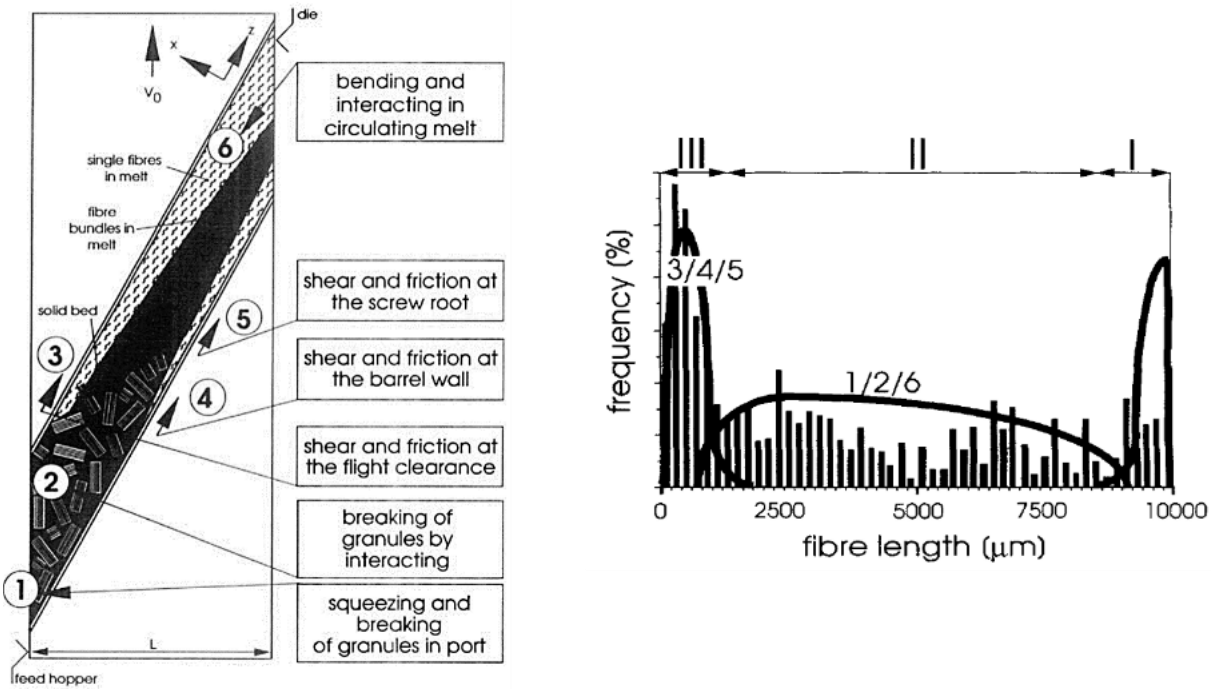

Figure 2.3, Left: Fiber attrition mechanisms, Right: Attrition mechanisms and corresponding fiber length [48].

Wolf proposed reducing the temperature gradient by preheating the pellets as a technique for preventing attrition [48]. A reduction of shear stress also mitigated damage at the compression and metering zones. Inoue et al., found that the screw geometry in the compression zone has a substantial impact on fiber attrition [52]. They found an optimized screw design (Dulmadge [53] with a variable pitch) reduced the fiber breakage compared to a standard screw.

In 2005, Lafranche et al., in a similar way to Wolf, measured the fiber length at different zones of the screw in the plastication unit [29]. Their results suggest that the most severe fiber degradation occurs in the compression zone. Figure 2.4 summarizes the fiber length history along the process.

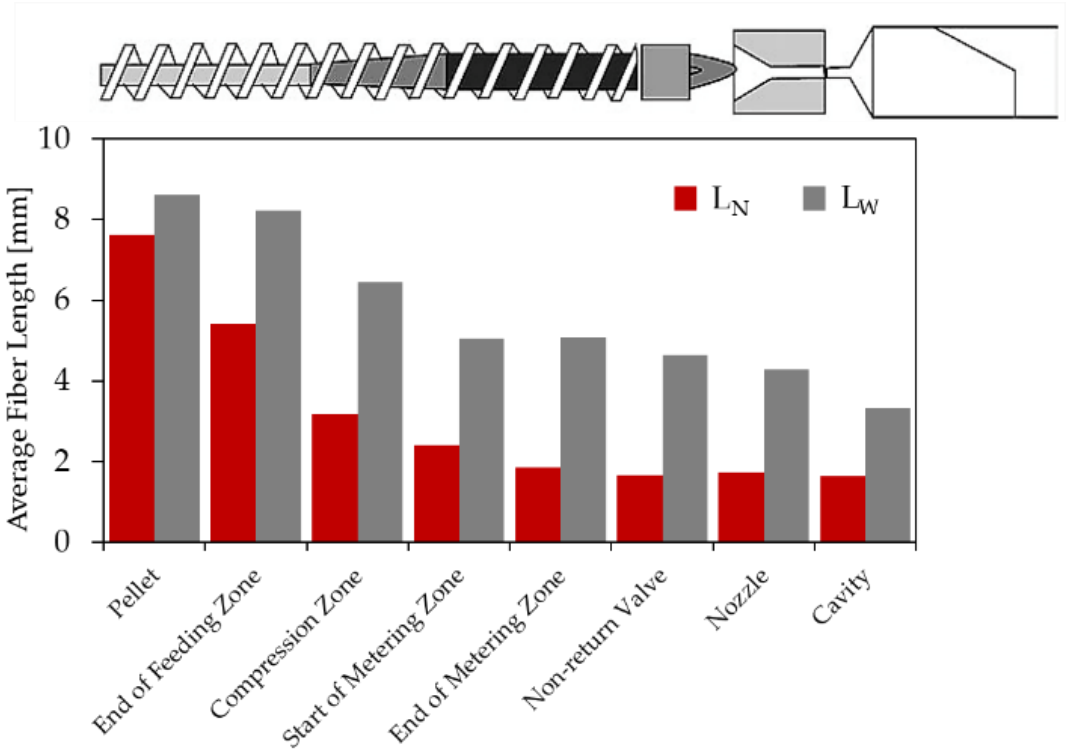

Figure 2.4: Fiber length reduction along the plastication unit [29].

O'Regan et al., found fiber lengths vary through the injection molded part thickness [54]. Bailey et al., reported mean fiber lengths in the inner core to be three times those of the skin layer, a phenomenon attributed to the high shear rates in the skin during mold filling [9]. Phelps et al., mentioned this fact as one of their motivations for developing a shear dependent fiber breakage model [19]. In their experiments with a 180 mm diameter center-gated disk and glass fiber-reinforced PP with 40%wt fiber concentration, mean fiber length (L_W) decreased 20 % over a length of 90 mm.

In a more recent study, Goris analyzed the full microstructure (FOD, FC and FLD) of injection molded plaques of size 102 x 305 x 2.85 mm3 [30]. He used various concentrations (5 – 60%wt) of glass fibers in a PP matrix. He reported a decrease in fiber length inside the cavity as a function of flow length only for low concentrations (5 and 10%wt). In his experiments, commercial grades (20, 30, 40 and 60%wt) did not show a correlation between flow length and fiber length reduction.

Both, Phelps and Goris, observed a slight increase in length towards the end of the cavity when looking at L_W; this suggests some long fibers make it to the end of the cavity almost undamaged [8,33].

2.3 Studies on fiber dispersion

While studies on dispersion and mixing of agglomerates are abundant [47], little work exists on the characterization of fiber dispersion for LFTs. In 2014 Ren et al., investigated the dispersion and breakage during processing of direct long fiber (D-LFT) reinforced polypropylene containing 30%wt glass fibers [49]. They identified two mechanisms of dispersion that are analog to the processing of LFTs:

i. Occasionally, fiber bundles separate into smaller 'daughter' bundles.
ii. Individual fibers are sheared off the bundles continuously throughout the whole dispersion process.

This second mechanism requires the melt to penetrate and impregnate the bundle. They concluded that fibers that are not wetted by melt suffer more breakage during the initial stage of dispersion.

Kuroda et al., investigated the initial mechanisms of dispersion for chopped glass fibers in a PS matrix and found that two types of dispersion mechanisms occur in a stochastic manner [28]:

i. Rupture (separation into daughter bundles).
ii. Erosion (separation of individual fibers).

They indicated that these mechanisms were dependent on the bundle morphology, pointing out that notches and voids in the fiber network are likely sites of rupture initiation and propagation (**Error! Reference source not found.**).

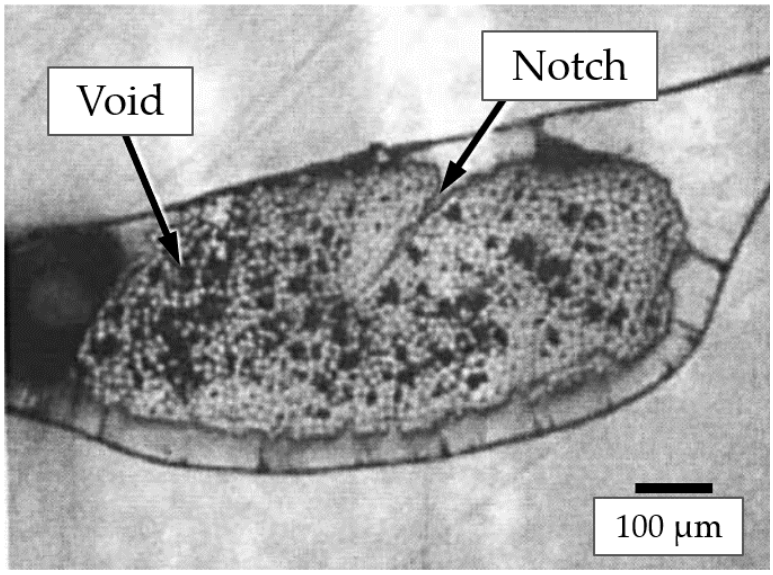

Figure 2.5: Cross section of fiber bundle showing the presence of voids [28].

Kuroda et al., reported dispersion by tracking the fraction of undispersed bundles as a function of total strain [28]. Ren et al., defined dispersion as the weight fraction of fibers in the disperse phase, and measured it by burning off the matrix, weighting the sample; then removing with twicers the undispersed bundles and weighting the remaining fibers [49]. Finally, Inoue et al., in a very interesting way, measure dispersion in the mold cavity by quantifying the fractal dimension in a binarized micrograph [52]. They confirmed that processing parameters which minimized fiber damage or promote good fiber dispersion are in conflict. High shear stress regions increased fiber dispersion, however decreased residual fiber length, thus making the simultaneous improvement of both properties challenging.

2.4 Prediction of fiber damage

In 1922 Jeffery solved the Stokes equations of motion for a single, force-free, rigid, ellipsoidal particle in a low Reynolds number flow and derived an equation that described the motion of such particle in a shear flow [55]. His work is the base for all modeling approaches for fiber motion and therefore fundamental for understanding how hydrodynamic stresses lead to fiber deformation and then breakage. His derivation shows ellipsoidal particles have a period of rotation which is proportional to the aspect ratio and inversely proportional to the rate of deformation, the trajectory described by the ellipsoid ends is known as Jeffery's orbit.

In 1938 Burgers expanded the solution to a slender cylinder and determined the distributed load acting on its surface during the period of rotation [56]. A couple decades later Forgacs et al., conducted various experimental studies with particles such as spheres, discs, flexible fibers and ellipsoids [36,37]. Their results validated Jeffery's theory and Burger's force derivation.

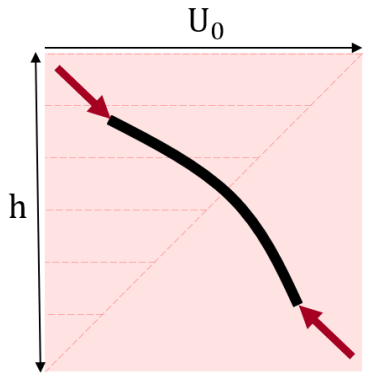

Figure 2.6 Compressive load on fiber on the onset of buckling under simple shear flow

Forgacs et al., used Burgers' formulation along with Euler's beam theory, to derive an equation to estimate the critical product $\dot{\gamma}\eta$, at which a fiber with Young's modulus E and aspect ratio L/D would start to buckle:

$$(\dot{\gamma}\eta)_{crit} = \frac{E(\ln 2\,(L/D) - 1.75)}{2\,(L/D)^4} \qquad 2.4$$

They concluded fibers withstand a load cycle of tension and compression depending on the fiber orientation respect to the flow (Figure 2.6). By increasing the flexibility of the fibers (Dacron, Rayon and Nylon) Forgacs et al., identified various orbits, these are depicted in Figure 2.7:

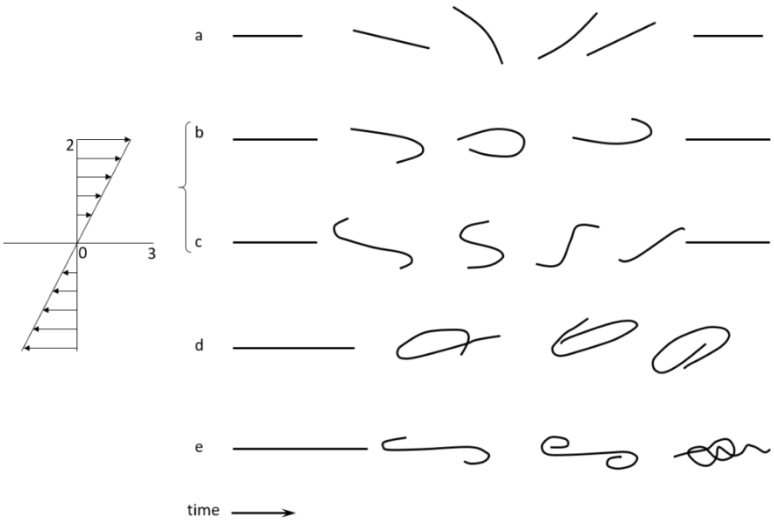

Figure 2.7: Rotation orbits for fibers of varying flexibility [22].

i. Springy regime (a): Orbits where the critical condition for bending is slightly exceeded. When the fiber reached the angle where the compression is the highest (-45°) it will bend as a leaf-spring.

ii. Snake regime (b, c): When the flexibility is further increased the tips of the fibers seem to be moving independently, causing the fiber to bend and then straighten again. When the fiber was highly symmetric the fiber would form an S.

iii. Coil regime (d, e): If the flexibility is further increased, fibers will experience coiled orbits with or without entanglements.

In 1981 Salinas et al., reproduced Forgacs et al., experiments with reinforcing fibrous materials, including glass fibers with aspect ratio from 280 to 680 [22]. They found fibers broke under the snake rotation regime when the minimum radii of curvature were reached. Only very stiff or brittle materials (Carbon fiber type 1, crocidolite) were predicted to break on the springy regime. They derived an empirical expression for the critical product $\dot{\gamma}\eta$ at which a fiber with Young's modulus E and aspect ratio L/D would break:

$$\frac{E}{\dot{\gamma}\eta} = A\,(L/D\,)^{B}\exp(C\,(L/D)\,) \qquad 2.5$$

In 2005 Shon et al., studied fiber breakage during compounding of SFTs [18]. They evaluated various combinations of mixing elements and their impact on fiber length reduction as a function of axial distance in a counter-rotating twin screw extruder. Partly based on the assumption that fiber damage is caused by buckling, they postulate a fiber break-up kinetic model in which an average fiber length L decreased exponentially toward a residual length following:

$$\frac{dL}{dt} = -k_f L - L_\infty \approx -k_f L \qquad 2.6$$

where k_f is the fiber breakup rate constant and L_∞ is the fiber length at which there is no more buckling (Figure 2.8). They did not attempt to derive expressions for either of the variables in their model and just determine them by fitting the curve to the experimental data. Bumm et al. later extended Shon et al.'s work and derived expressions for both parameters based on Euler's buckling theory [59].

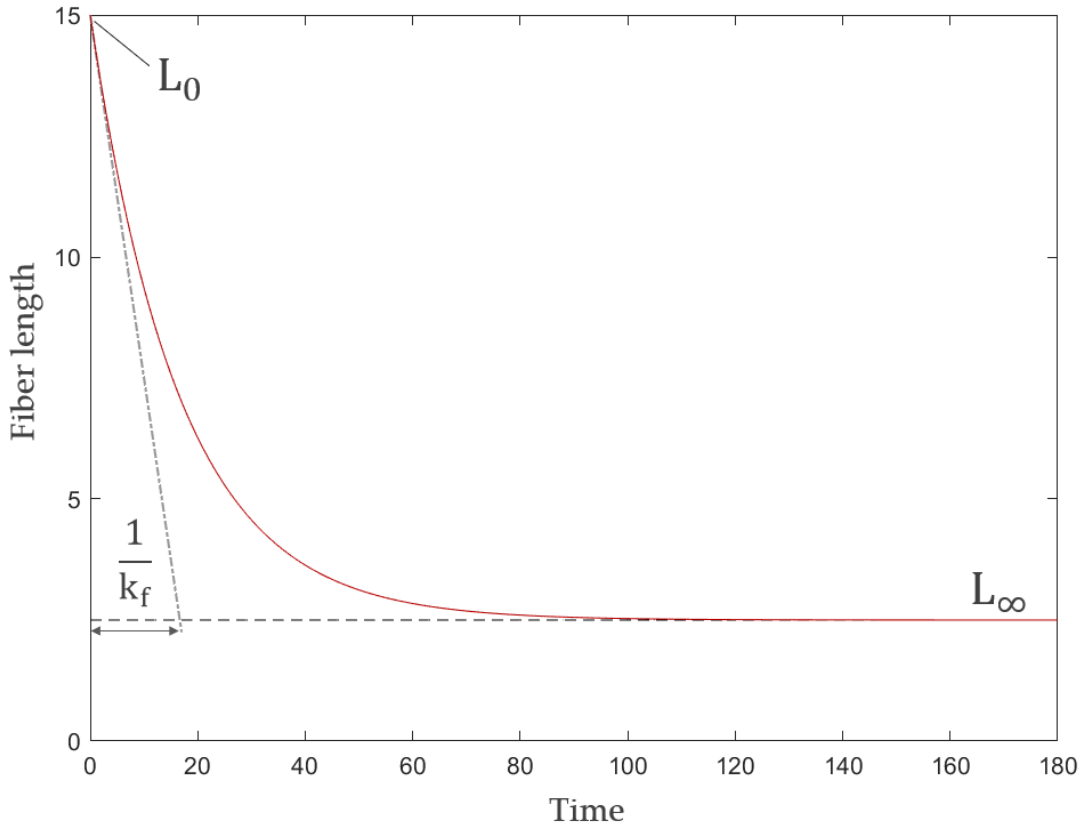

Figure 2.8 Illustration of expected fiber length reduction over time according to Shon's model

In 2013, Phelps et al., developed a continuum model based on the slender body theory of Forgacs and Mason [8,37]. They start by defining the critical force needed to cause buckling (F_{crit}) and the critical flow regimen ($\dot{\gamma}_{crit}$) which would cause buckling as a function of fiber characteristics and flow parameters:

$$F_{crit} = \frac{\pi^3 E_f D^4}{64 L_i^2} \qquad \dot{\gamma}_{crit} = \frac{\pi^3 E_f D^4}{4\zeta \eta_m L_i^4} \qquad 2.7$$

where E_f is the Young's modulus, D and L_i are the diameter and length of the fiber, respectively, η_m is the viscosity of the matrix and ζ is the drag coefficient.

During the fiber's period of rotation, it will be under compressive stresses, which will lead to buckling if they surpass the critical load. A ratio between the hydrodynamic

loads and the critical buckling load is proposed as $Bi = F_h/F_{crit}$. This dimensionless variable for fiber buckling can be expressed as

$$B_i = \frac{4\zeta\eta_m\dot{\gamma}L_i^4}{\pi^3 E_f D^4} \qquad 2.8$$

and it defines the threshold ($Bi > 1$) above which breakage will occur. With the mechanics of breakage defined, the authors move on to defining a state equation in which the number of fibers of length i (N_i) changes over time following

$$\frac{dN_i}{dt} = -P_i N_i + \sum_k R_{ik} N_k \qquad 2.9$$

The first term on the right describes the fibers that break into smaller 'daughter' fibers. While the second term corresponds to longer fibers which after breaking end up of size i. This state equation is implemented as a postprocessing tools for a center gated disk filling simulation and the model parameters are optimized so the predicted length distribution matches the experimental measurement (Figure 2.9).

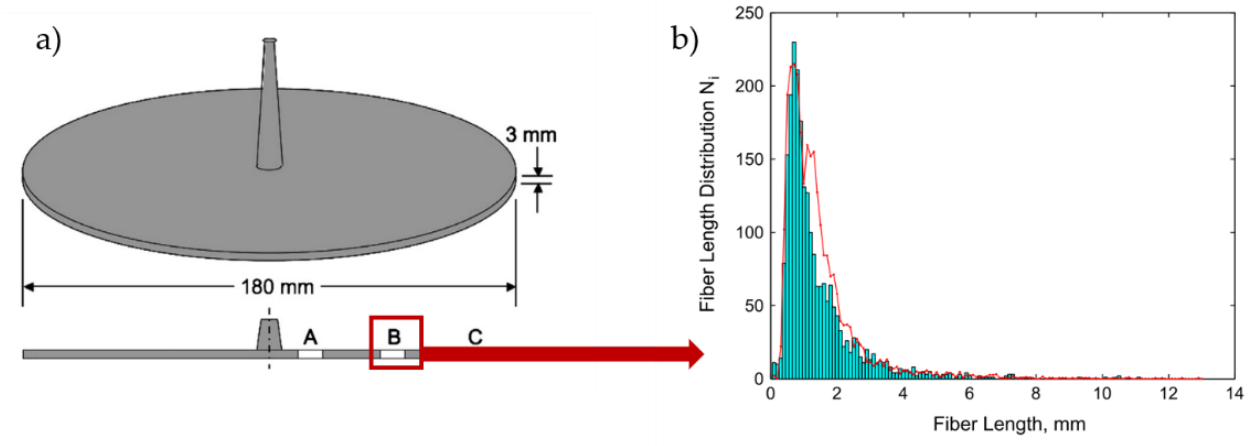

Figure 2.9: a) Center gated disk mold, b) Fiber length distribution at location B [19].

This approach does not account for the dependence of fiber breakage on the fiber volume fraction, ignoring fiber-fiber interactions as a source of damage. However, it has a very well-structured computation algorithm that, in the authors' own words, allows

further development if further knowledge is available on the physics of fiber failure. Phelps et al.'s model is currently the standard method for predicting fiber damage during injection molding in commercial software.

Durin et al, proposed a similar model for fiber attrition during compounding of short fibers [26, 60]. Rather than tracking the changes in average fiber length over time, they wrote a conservation equation for the complete fiber length distribution based on a breakage probability. Following Forgacs and Masons analysis, fiber buckling is determined to be the mechanism by which fibers break. A dimensionless buckling number B_u defines the critical conditions under which a fiber would buckle and eventually fail. This number is a function of the product $\dot{\gamma}\eta$, the fiber's stiffness and aspect ratio. The model does not consider fiber-fiber interactions to have influence on fiber failure. Durin et al.'s model has also been implemented in commercial software for twin screw extrusion.

Chen et al. studied breakage on a capillary rheometer and proposed a breakage model based on semi-flexible orientation of the fibers [61]. Following Salinas and Pittman's conclusions, they argue fibers break due to large deformations when the minimum radius of curvature is reached. In their model fiber-fiber interactions are indirectly accounted for by the isotropic rotary diffusion parameter C_i in the orientation model [36]. Moritzer et al. conducted fiber breakage experiments under simple shear employing a Couette device and pre-compounded polypropylene with short fibers [62]. Their results corroborate Shon et al.'s proposed kinetics. They observed fiber concentration influenced both the breakage rate and the residual length L_∞. After performing a dimensional analysis, they propose a phenomenological model which accounts for hydrodynamic stresses, fiber concentration and fiber properties. Goris conducted similar experiments with coated LFT pellets and observed similar behavior [21].

In recent years, direct particle simulations have been used to study in detail the mechanisms of fiber breakage. Sasayama et al. simulated fiber breakage under simple shear flow considering fiber-fiber interaction [63]. Their results show that the fiber length decreases with the product $\dot{\gamma}\eta$. They present a very interesting depiction of how fiber-fiber interaction can lead to breakage. Chang et al. built a failure criterion based on a critical radius distribution obtained via loop test measurements, similar to Salinas and Pittman [64]. The introduction of this failure distribution in their direct particle simulation improved their fiber length prediction when compared to Couette experiments. These approaches are somewhat limited due to their computational cost, so it is unlikely they will be used to predict fiber length in real components. However, they have great potential as numerical rheometers since the coupled effects of fiber orientation, fiber length and fiber concentration can be studied.

3 Fiber Breakage

As shown by Thomason, mechanical properties of components molded with LFTs benefit from increased fiber length. That is the reason why it is essential to understand what kind of mechanisms cause the reduction of the fiber-length during processing. Fundamentally, the actual phenomenon and the progress of fiber attrition can be reduced to a solid mechanics problem, upon which classical material and deformation theories can be used to analyze the internal material state and the external conditions that cause failure. In the following section, the internal material state will be studied, and the outcome data will be used to construct a failure criterion.

3.1 Single fiber failure

The reinforcing fibers in LFT materials are commonly E-glass, this material is mostly used in the automotive industry for its cost effectiveness; its mechanical properties locate it on the mid-range of the silica-base reinforcing fibers [2]. Nominal properties according to the fiber supplier are listed in Table 3.1.

Table 3.1 Glass fiber properties

Variable	Value
Density [g/cm^3]	2.56
Ultimate strength [MPa]	2600
Young's Modulus [GPa]	73
Diameter [μm]	19±1

Various researchers have demonstrated that fibers moving within a viscous flow will be subjected to stresses that cause bending deformation [22, 57, 58]. Once the internal state of stress due to this deformation reaches the material's ultimate strength, failure

occurs. Additionally, the material's strength is strongly related to the number and distribution of the micromechanical defects along its surface [65]. Nominal mechanical properties are determined by uniaxial tensile loading, which causes an internal state of stress constant over the entire length of the fiber. In the case of beam deflection caused by applied forces, the fraction of stress varies over the length of the fiber. Thus, fewer material defects are subjected to high loads. In addition, beam flexure causes a non-uniform distributed state of stress, where the highest stresses occur in the outer surface. Therefore, the uniaxially determined fiber strength is insufficient for describing the failure of the fiber under bending and underestimates the maximum bearable load [68, 69].

A method to characterize the material properties of glass fibers was presented by Sinclair. The strength of individual fibers is measured by twisting the fiber into a loop and pulling its ends away from each other so that eventually rupture happens [67]. The diameter of the loop before failure describes the critical curvature, from which the strength can be determined [68–71]. A significant challenge in this type of characterization is to ensure that the experimental conditions are constant. During the test, the loop shape of the fiber must be maintained flat to measure accurately and achieve repeatable results. Two different ways to meet this requirement are shown in Figure 3.1. On the left, the fiber has been twisted into a knot. Upon pulling, the friction and local curvature around the knot base leads to early failure. The post fracture photograph is overlapped with the knot prior to failure. It can be observed where rupture occurred. Strength determined through this method would be underestimated similarly to the uniaxial test.

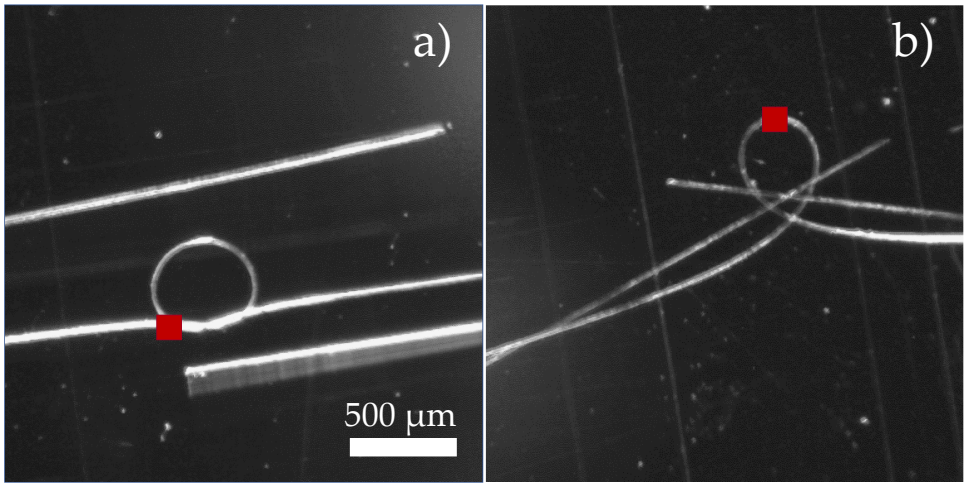

Figure 3.1 Before and after fiber fracture, a) Knot test, b) Loop test

On the right, the fiber has been twisted into a loop and placed between two microscope slides to prevent the loop from unfolding. Ideally, with this method one should have more control over location of fracture, however, friction at the base of the loop can still occur and fibers could fail before reaching the critical stress. To verify the exact location of rupture various loop tests were performed and recorded in high speed. Figure 3.2 shows the experimental set up.

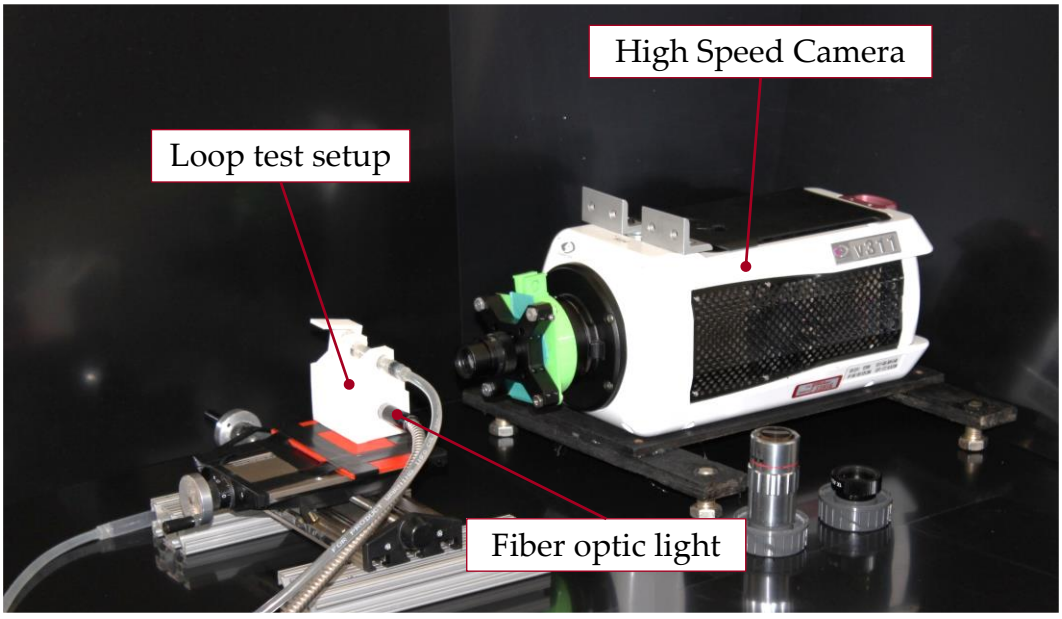

Figure 3.2 High speed recording set up for loop test

A digital, high-speed v311 Phantom video camara was employed; a rate of 1500 frames per second was used to capture the exact instant when fibers broke. At this frame rate, the camera sensor requires large amounts of light bouncing off of the fiber to have a high-quality capture.

A fiber optic light dimed through a diffusion glass was used to light up the frame where the test was performed. To decrease the friction effects between the fiber and the glass plates, especially in the region where the fiber overlaps with itself, a film of glycerin was placed between the microscope slides. This allowed the fiber to move freely. However, since the glycerin and fibers had similar refraction indices, the fibers were dyed with black ink prior to testing.

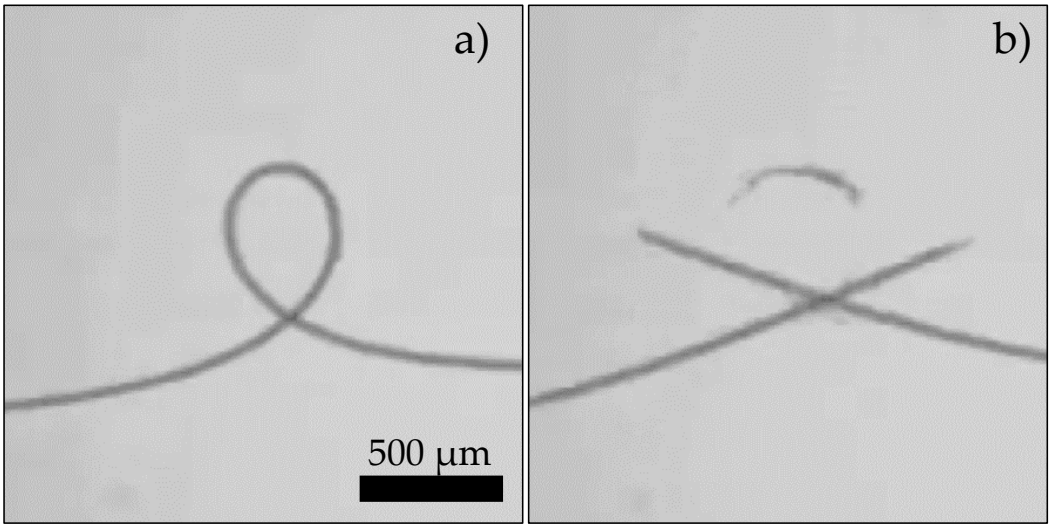

Figure 3.3 Loop failure photograph recorded at 1500 fps a) Before rupture, b) After rupture

Figure 3.3 shows the frames before and after fracture for one of the tests. It confirms the loop test is appropriate to measure the material's strength, since rupture occurred at the top of the loop. The introduction of the glycerin film is key in obtaining reliable results.

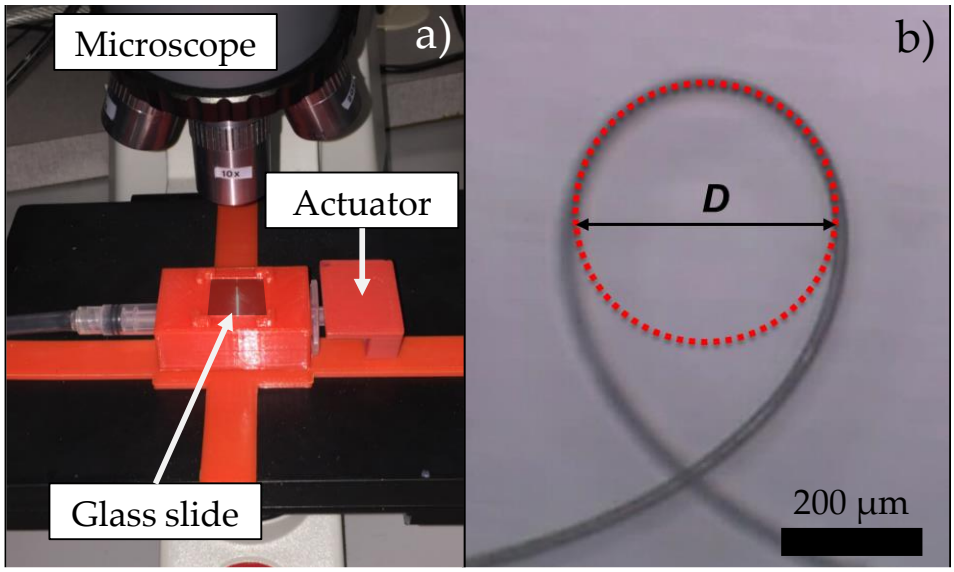

Figure 3.4 Loop test, a) Experiment set up, b) Captured loop image

The loop test set up was modified to fit a laboratory microscope (Figure 3.4). During testing, the deformation of the fiber was recorded and the frame right before the fiber breakage occurs was evaluated by measuring the outer diameter of the fiber loop. A total of 50 experiments were performed and obtained an average value of 204.6 µm (arithmetic mean) for the critical radius of curvature. The values vary from 119 to 371 µm. The static distribution is not Gaussian distributed.

Since the strength of the material is strongly dependent on the micro defects in the material, the strength or the critical radius of curvature of the material can be characterized with the Weibull distribution model [65]. The Weibull distribution is often used for reliability analyses and the measuring of failure critical values of materials and structures [70]. It describes the probability continuously and is entirely determined by two parameters, α and β. The probability density function of a Weibull distribution f (x;α, β) for a random variable x, which represents the characteristic attribute, is given by:

$$f(x;\alpha,\beta) = \frac{\beta}{\alpha} \cdot \left(\frac{x}{\alpha}\right)^{\beta-1} \cdot e^{-\left(\frac{x}{\alpha}\right)^{\beta}} \qquad 3.1$$

Figure 3.5 presents the experimental measurements for the critical radius of curvature and the best fit obtained for the Weibull probability distribution function.

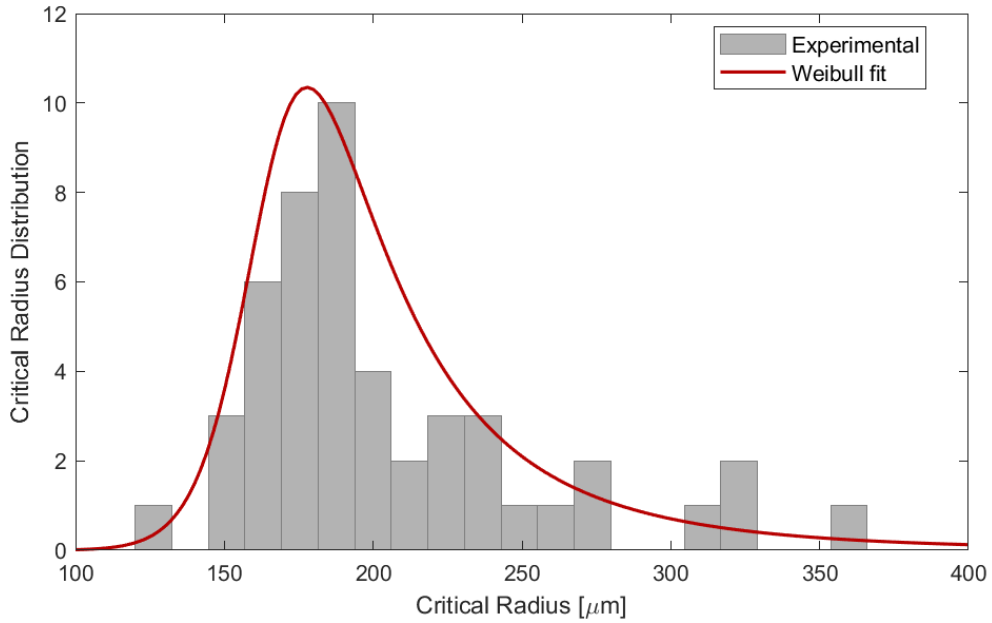

Figure 3.5 Critical radius distribution resulting from the loop test, Weibull distribution fitted to experimental data (in red)

In order to understand the deformation of the fiber during the single fiber loop test the theory of deflected beams is discussed. For this purpose, a fixed clamped cantilever beam loaded with force is considered. Bending theories are composed of three principles [73–75]. The material model establishes the direct relationship between a strain and the resultant stress and is described by the stiffness properties of the material. The kinematics describe the overall deformation of the structure. Furthermore, the mechanical equilibrium of the structure must be considered [72]. In general, the models for the mechanics of beams are differentiated into shear-stiff and shear-soft theories [74, 75]. The classic approach of Euler-Bernoulli to describe the bending behavior neglects the shear deformation, and the deflection of the beam is considered as pure bending. The shear distortion can be regarded with the theory of Timoshenko [72].

The single fiber loop test is mainly characterized by geometric nonlinearity since the deformations of the tested fibers are large and the position of the force application point constantly changes during the test. The material behavior however can be considered as linear elastic. This leads to a straightforward determination of the ultimate strength, at least under the Euler-Bernoulli formulation given by:

$$\frac{r_{crit}}{r_d} = \frac{E}{\sigma_u} \tag{3.2}$$

Where r_{crit} is the critical radius of curvature and r_d is the fibers cross-sectional radius.

To determine the strength according to the non-linear formulation, the problem can be approach geometrically in a Cartesian coordinate system. With the arc length s as the control variable, which is needed since the exact expression for the curvature is evaluated to describe the local bending state of the beam [74]. Due to the symmetry of the loop shape, only half of the fiber is part of the calculations. The differential equation of the deflection curve of a beam subjected to a force F in x-direction can be expressed as follows:

$$EI \cdot \frac{d\theta}{ds} = -F \cdot y \tag{3.3}$$

The elongation of the beam can be neglected because the elongation is very small in comparison to the deflection of the beam. To obtain a differential equation that is only a function of the variable s and the inclination θ , the geometric relation dy/ds = sinθ is used.

$$EI \cdot \frac{d^2\theta}{ds^2} = -F \cdot \sin(\theta) \tag{3.4}$$

This differential equation can be transformed and solved with the help of elliptical integrals. However, an alternative approach is using large deformation mechanics simulation to determine the shape of the deformed fiber, then using a semi-analytical solution of this large deformation problem by tracking the inclination of the fibers end.

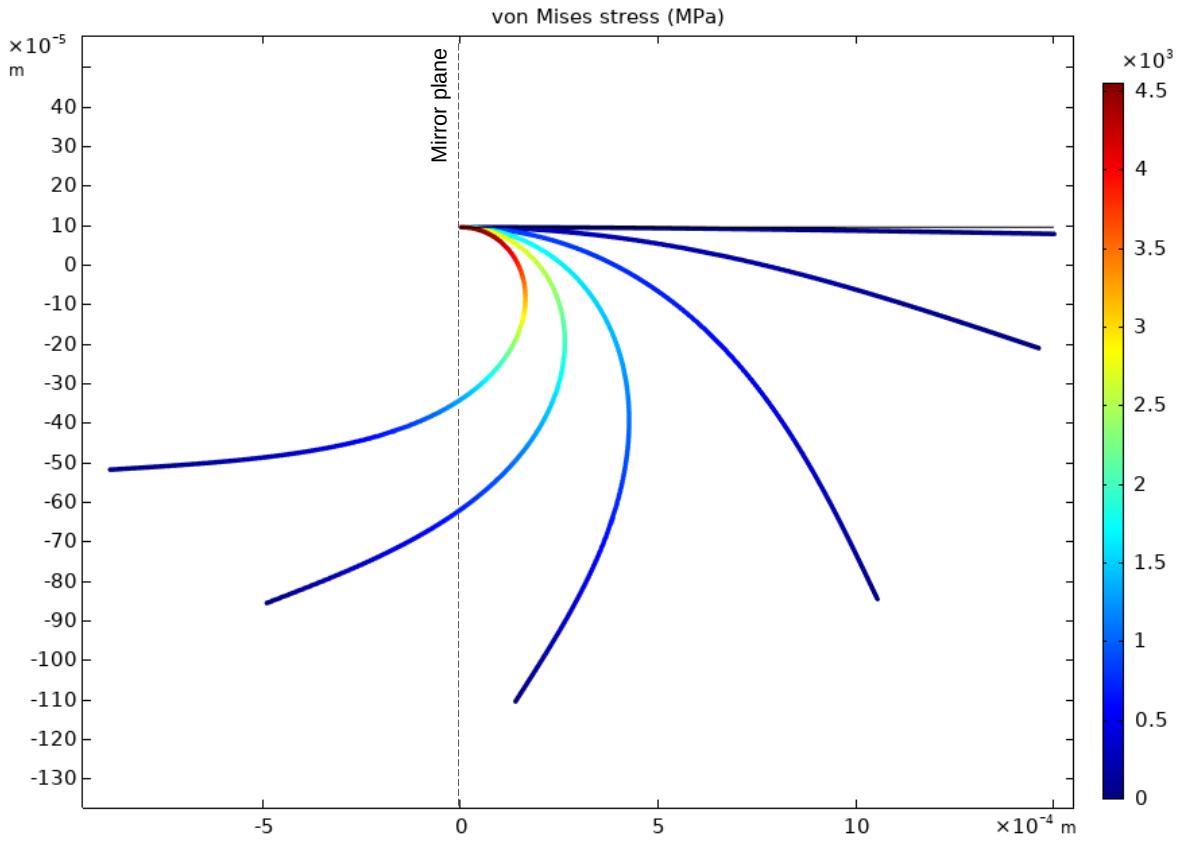

Figure 3.6 Large deformation simulation of glass fiber under bending load

Figure 3.6 presents the large deformation simulation results of the fiber under incremental loading steps. The von Mises stress calculated during bending corresponds to the Euler-Bernoulli formulation, and matches exactly the curve defined by equation 3.2. The geometry of the deformed fiber was also used to determine the ultimate strength according to the large deformation mechanics. The comparison between both formulations is presented in Figure 3.7.

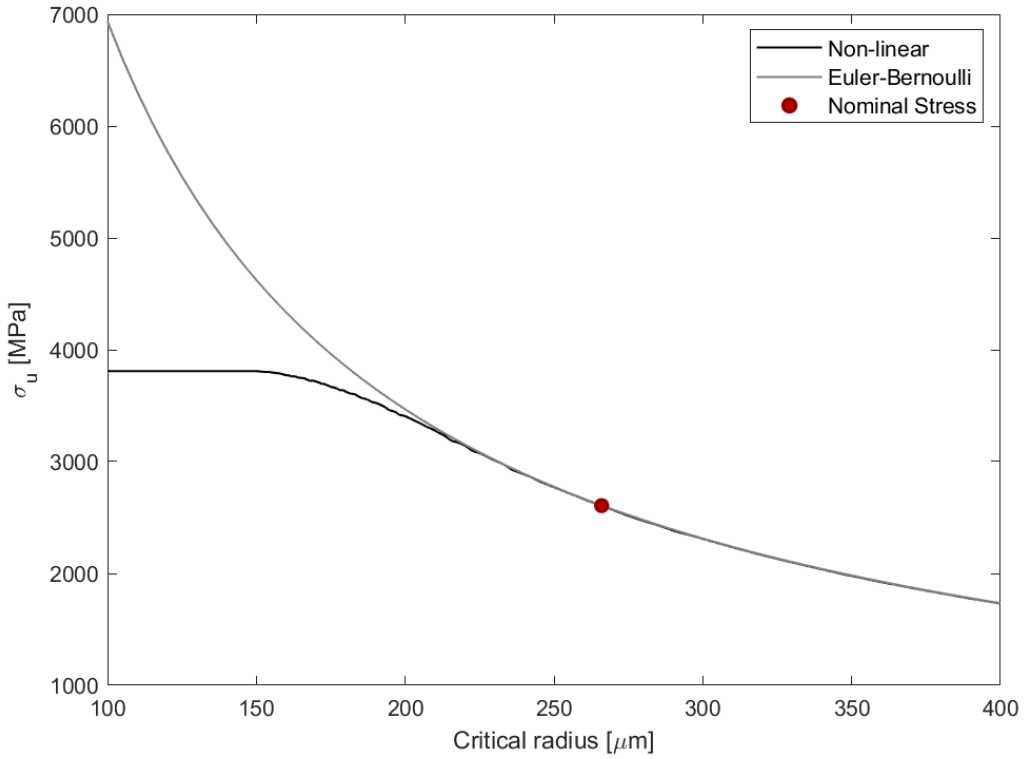

Figure 3.7 Ultimate stress determined from the critical radius experiment

The stress is plotted over the range of radii determined form the loop test (100-400μm). Initially we can observe that the critical radius corresponding to the nominal stress is about 60μm higher than the arithmetic mean of the distribution. Meaning, the fibers in average can withstand more stress than what is nominally anticipated under uniaxial loading. Both formulations overlap for most of the range and only divert for extremely large deformations (i.e., small radii). Based on this, we can assume the linear elastic formulation is sufficient to represent the internal material state of the fibers. This formulation will be used on the model development as the failure criterion for fiber rupture under external stresses. The next section focuses on those external stresses and how they modify the kinetic behavior of the attrition process.

3.2 Fiber attrition kinetics

Investigating the underlying physics of fiber breakage experimentally in an injection molding process or during compounding in a twin-screw extruder is challenging, because of the complex and changing flow conditions that the fibers are exposed to throughout the various stages of the process. Consequently, in this work a Couette rheometer was used to study fiber breakage under simple shear and controlled processing conditions [21]. Important process and material variables are studied, and their impact on fiber damage is measured. The material used in the following studies is long glass fiber-reinforced polypropylene (PPGF, SABIC® STAMAX™). The material is supplied as coated fiber pellets with a length of 15mm, and nominal glass fiber content of 20%, 30% and 40% by weight (PPGF20, PPGF30 and PPGF40).

The Couette device consists of concentric inner and outer cylinders with an annular gap, as shown in Figure 3.8. While the inner cylinder rotates at a defined speed Ω (or torque T), the outer cylinder is stationary, exposing the material to a simple shear flow within the annular gap. The temperature is controlled through insulated heater bands surrounding the outer cylinder and a thermocouple measuring the melt temperature. The dimensions of the Couette rheometer were selected to be characteristic of the conditions during plastication in injection molding. The diameter of the inner cylinder is 35mm, the annular gap is 5mm, and the length of the annular volume is 80mm (Figure 3.8). The inner cylinder is driven by a Plasti Corder™ torque rheometer (C.W. Brabender Instruments Inc., Hackensack, NJ), controlling the rotational speed.

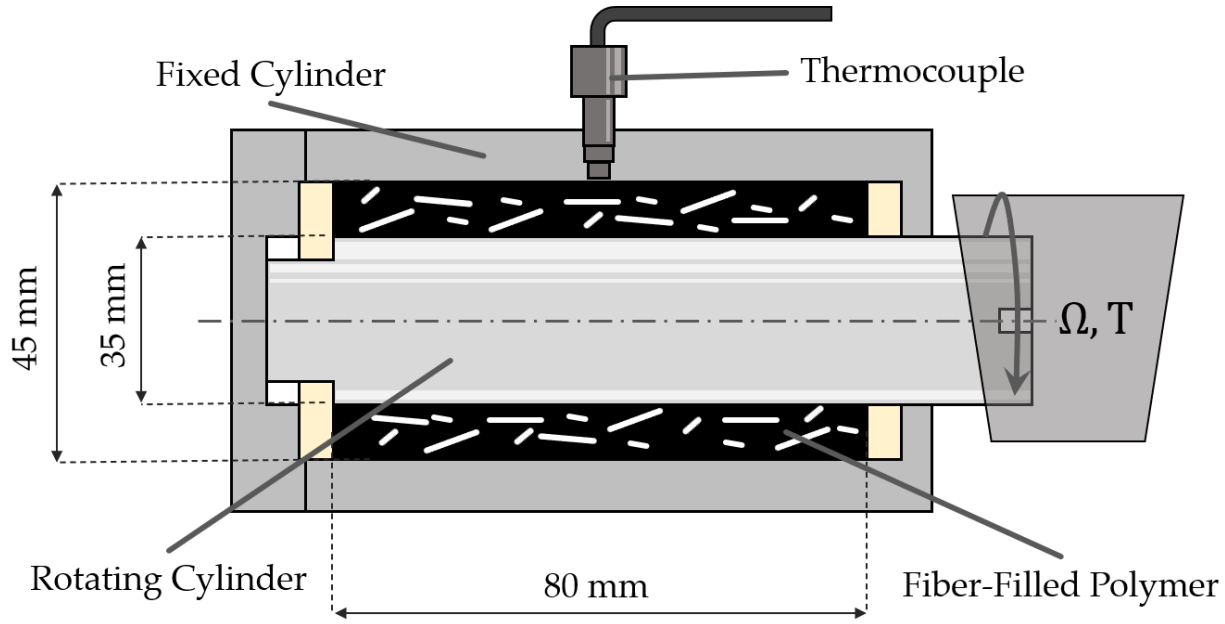

Figure 3.8. Illustration of the Couette rheometer setup for the study of fiber breakage.

Based on the fiber break-up model suggest by Shon et al., a set of studies were conducted with the Couette rheometer to understand the kinetics of fiber length degradation, and to isolate the effects that processing conditions have on the steady state fiber length (L_∞) and the breakage rate coefficient (k_f). After each experiment, the material was removed from the Couette and the fiber length was measured employing the technique developed at the Polymer Engineering Center.

3.2.1 Length decay over time

The first study explored the fiber length degradation over time for various processing speeds while the fiber content and melt temperature were kept constant (Table 3.2). The material was sheared for increasing intervals of time starting with 20s until 300s. This set of experiments allow the characterization of fiber length degradation as a function of residence time. Hence the overall kinetic can be observed and general conclusions can be drawn.

Table 3.2. Experimental plan1: Length decay over time

Variable	Levels
Fiber content [%wt]	30
Melt temperature [°C]	250
Rotational speed [rpm]	50, 100,150
Residence time [s]	20 to 300

3.2.2 Steady state length

The second set of experiments aimed to study the impact different variables have on the residual fiber length, that is, the length at which no additional amount of shearing time will cause additional fiber breakage; or as described by Shon et al., the fiber length at which there is no more buckling. For each variant in this study, the residence time and processing speed were selected to ensure L_∞ was reached based on the results of the first experimental plan. This study was designed as a full factorial DOE with three factors and three levels, as shown in Table 3.3. The melt temperature was varied between 220°C and 280°C, representing the limits of the processing temperature range suggested by the material supplier [75]. Hence, the obtained measurements represent the most severe impact that can be expected from this factor.

Table 3.3. Experimental plan 2: Impact of process variables on equilibrium length

Variable	Levels
Fiber content [%wt]	20, 30, 40
Melt temperature [°C]	220, 250, 280
Rotational speed [rpm]	150
Residence time [s]	300

3.2.3 Attrition rate

The objective of this third set of experiments is to identify the influence processing conditions have on the breakage rate. Based on the exponential decay kinetics observed in previous studies, the greatest change in fiber length occurs early in the shearing cycle. This means that the fast changes in fiber length at the start of shearing will give us the best insight on the dynamic behavior.

However, because our interest is formulating a model for fiber attrition for a homogeneous suspension, the fact that in the initial pellet the fibers and matrix are not mixed introduces additional variability into the study. To illustrate this fact, Figure 3.9 shows a sequence of μCT images of PPGF40 pellets before shearing and after 5s, 12s and 20s of shearing. It is evident that perhaps before 12s what we have is still a heterogenous mix of fiber bundles and polymer matrix rather than a suspension as observed after 20s.

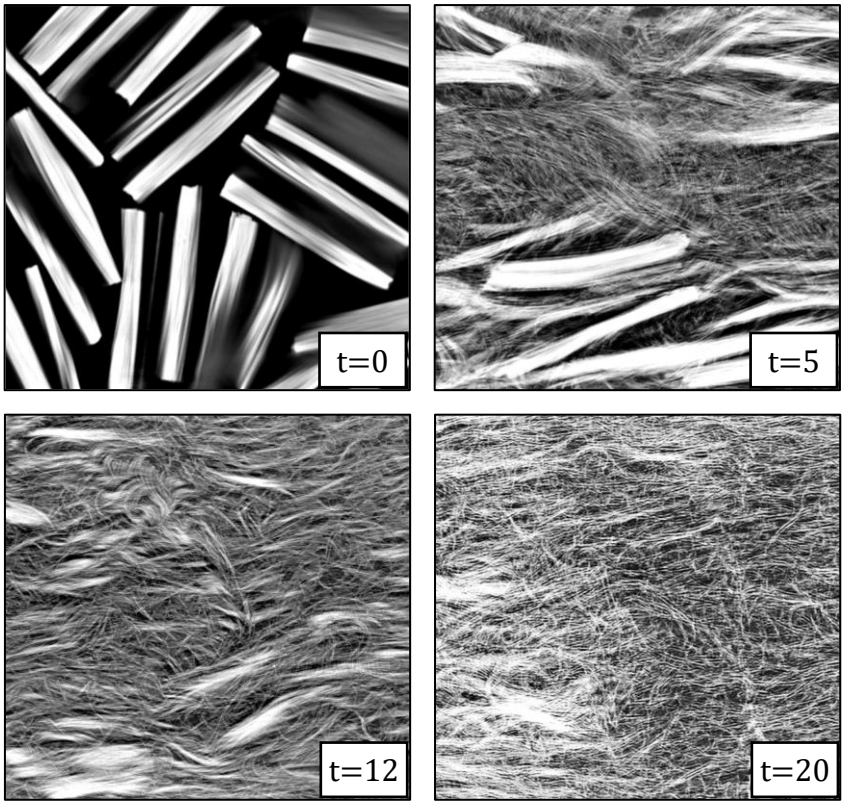

Figure 3.9. μCT slice of fiber dispersion for different resident times.

To address this issue a pre-dispersion step was introduced to disperse the bundle of fibers without causing excessive damage. This step involved shearing the polymer melt for 2s with a shear rate of $50s^{-1}$. The experiments were performed using high shear Couette rheometer at SABIC®, Geleen. With this equipment high rates of deformation could be imposed on the polymer melt for short spans of time. Temperature remained constant, while fiber content and processing speed were varied as shown in Table 3.4.

Table 3.4. Experimental plan 3: Impact of shear and fiber concentration on attrition rate.

Variable	Levels
Fiber content [%wt]	20, 30, 40
Melt temperature [°C]	250
Shear rate [s-1]	300, 500, 700
Residence time [s]	2

3.3 Results

The results are presented in three sections corresponding to the three experimental studies. When evaluating the results, fiber length is presented in terms of the weight-average L_W. The number-average fiber length (L_N) is also needed to reconstruct the FLD, however as both variables show the same trends with respect to the processing parameters, we have decided to present the results in terms of L_W as it is more representative of the length variable in LFTs.

3.3.1 Length decay over time

Figure 3.10 shows the reduction in fiber length as a function of residence time for PPGF30 with a melt temperature of 250°C at different shearing speeds. For these processing conditions, L_W decreased from 15mm down to 1.6mm - 0.8mm after residence times between 180s and 300s. Overall, the results confirm the expected exponential decay

with a severe length reduction of the fibers occurring within the first 50s of processing. As expected, an increment in processing speed increases the rate at which the fibers break and also decreases the residual/equilibrium length [62, 78].

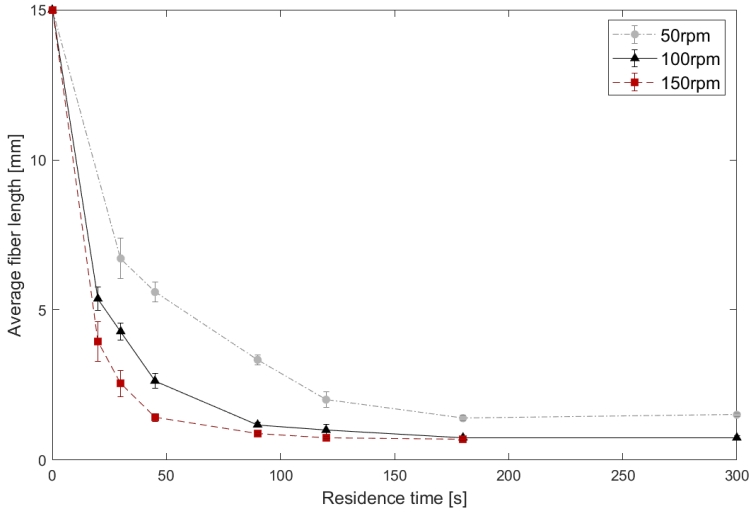

Figure 3.10. Fiber length reduction over time for PPGF30 at 250°C

3.3.2 Steady state length

The investigation of the impact of processing conditions and fiber concentration on L_∞ allows a direct analysis of the mechanisms that drive fiber damage, because it excludes the transient attrition at lower residence times. Figure 3.11 presents the results of the DOE.

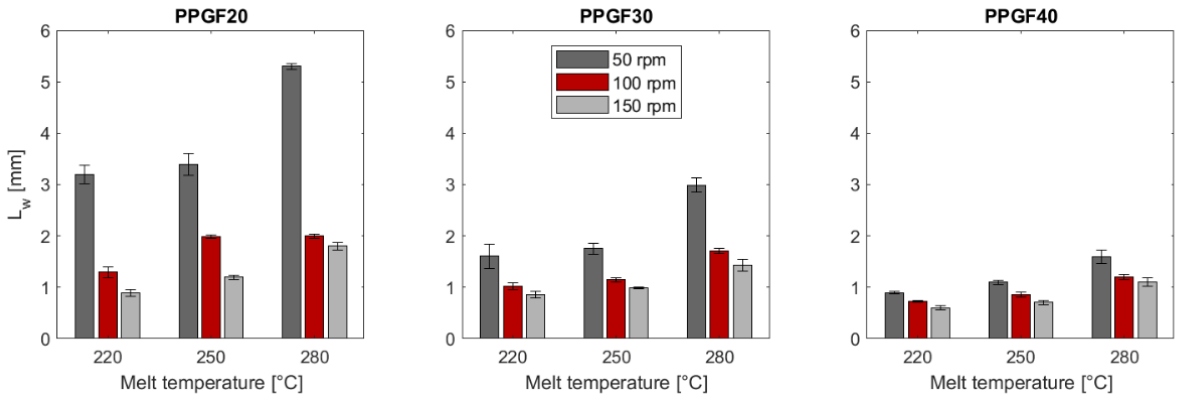

Figure 3.11. Outcome of the DOE for the steady state length showing the obtained weight-average fiber length $L_{W,\infty}$

An analysis of variance was applied to the measurements to determine differences in means between the factors and the level of the factors of the DOE. Figure 3.12 shows the main effect plots with respect to $L_{W,\infty}$. All three factors influence $L_{W,\infty}$ and have a statistically significant impact on the process-induced fiber breakage.

The melt temperature affects the suspension viscosity and, consequently, the stresses that the fibers are exposed to during processing. This dependency is evident in the obtained results, as the increase in temperature results in longer equilibrium length across all other factors. Processing speed also had the expected effect on the equilibrium length. As the rate of deformation increases the hydrodynamic stress experienced by the fibers increases forcing the equilibrium length to go down. In all trials, an increased fiber concentration resulted in reduced $L_{W,\infty}$. An increment in fiber content implies an increase in one of the breakage mechanisms, namely, fiber-fiber interactions. This result is important, since it indicates that fiber concentration is a variable which plays a role in the kinetics of damage and should be included our modeling efforts.

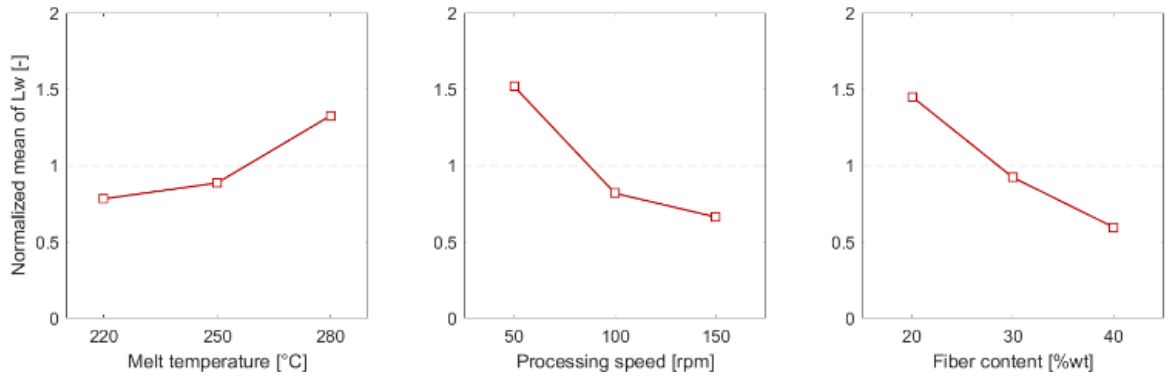

Figure 3.12. Result of the statistical analysis showing main effect plots on $L_{W,\infty}$

3.3.3 Attrition rate

Figure 3.13 shows the decrease in length for a short span of time for PPGF20, PPGF30 and PPGF40. Here, the impact of the pre-dispersion step is evident, the length was

reduced from its initial value of 15mm to 7mm approximately. However, it is still constant for each fiber concentration which is important for our analysis.

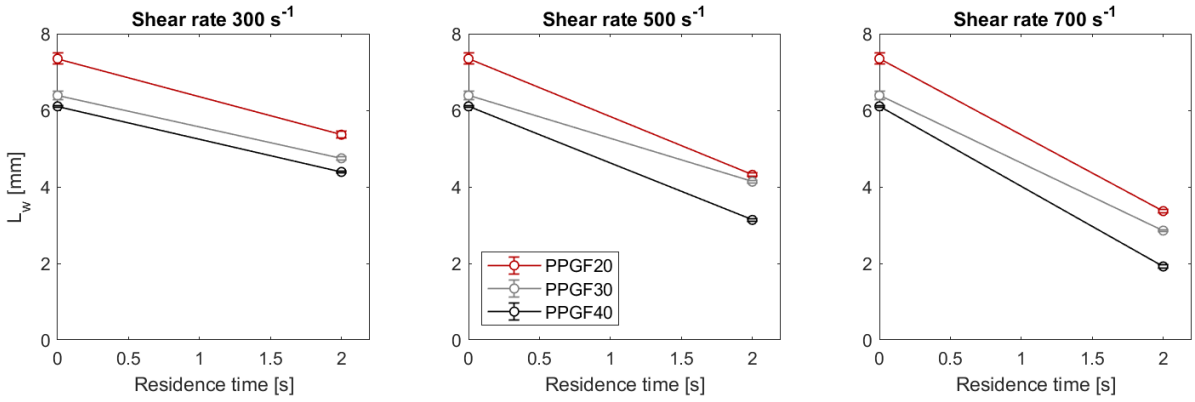

Figure 3.13. Outcome of experimental plan 3 showing the effect of shear rate on fiber attrition rate.

As observed in the first study, the attrition rate increases with the rate of deformation. The fiber length after shearing the sample at $700s^{-1}$ is nearly half of the length after shearing at $300s^{-1}$. Although the slope depends on the initial length, and the initial length changes between fiber concentrations we can observe the lines are nearly parallel, which suggests that the fiber content might not have a strong impact on the rate at which fibers break.

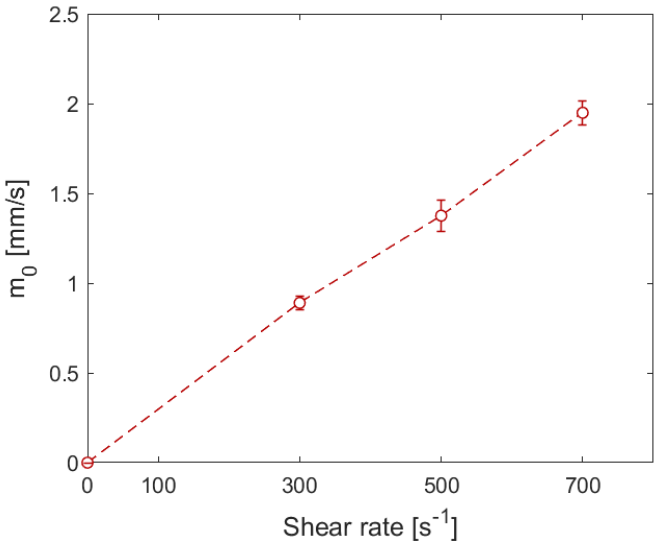

Figure 3.14. Average initial slope as a function of shear rate.

Plotting the average initial slope as function of the shear rate shows a linear proportionality between the variables, especially when including the data point at the origin; since, if the fibers are subjected to no shear there will be no damage and the slope will be zero (Figure 3.14).

3.4 Fiber damage during dispersion

There are two main drivers for wanting to study the effect of dispersion on fiber damage during processing of LFTs. First, previous work has shown that fiber damage is reduced when there is good fiber impregnation by the polymer matrix during plastication [28, 49]. One reason being friction between dry fibers is an additional source of damage. Also, early fiber damage occurs predominantly in the melting zone at the solid-melt interface, this means that fibers embedded in partially molten pellets will sustain damage even before any dispersion has taken place. Hence, optimizing dispersion while reducing fiber damage is key for increasing the mechanical performance of components molded with LFTs. Second, as previously discussed, the fiber concentration has an impact in the level of fiber damage; since in LFT pellets fibers and matrix are initially separated there is a transition stage where the fiber concentration is constantly changing within the suspension, potentially modifying the attrition kinetics. In the following section, the impact that dispersion has on the different aspects of fiber the attrition kinetics will be studied.

3.4.1 Impact on steady state length

In work by Wolf and Gupta et al., fiber length was measured along the melting zone of a single screw extruder [48], [77]. Both researchers observed that a large population of very short fibers originated from the damage occurring at the interface between the bed of solids and the melt pool. In contrast, moderate fiber damage was observed inside the

melt pool where fibers were already dispersed and fully surrounded by the matrix. Since the Couette experiments are conducted under constant melt temperature, we are virtually removing any effect melting might have on the breakage phenomena. Thus, in order to evaluate the impact dispersion has on the residual length L_∞ a similar approach to the one explored in section 3.2.3 will be taken.

The Couette device was used to shear PPGF30 coated pellets for a total residence time of 300s. The rotational speed was set to 150 rpm and temperature was fixed at 250°C. From the set of experiments used to determine the length decay over time (Section 3.2.1), we know that under these conditions L_∞ will be reached. A second variation of the test conditions involved introducing a low shear pre-dispersion step. For this step, the speed was set to 5 rpm for 95s, and then increased to 150 rpm for 300s approximately. Figure 3.15 shows each of the shearing cycles. The area under each curve is the same, since for a valid comparison the total strain needs to be equal for both test variations.

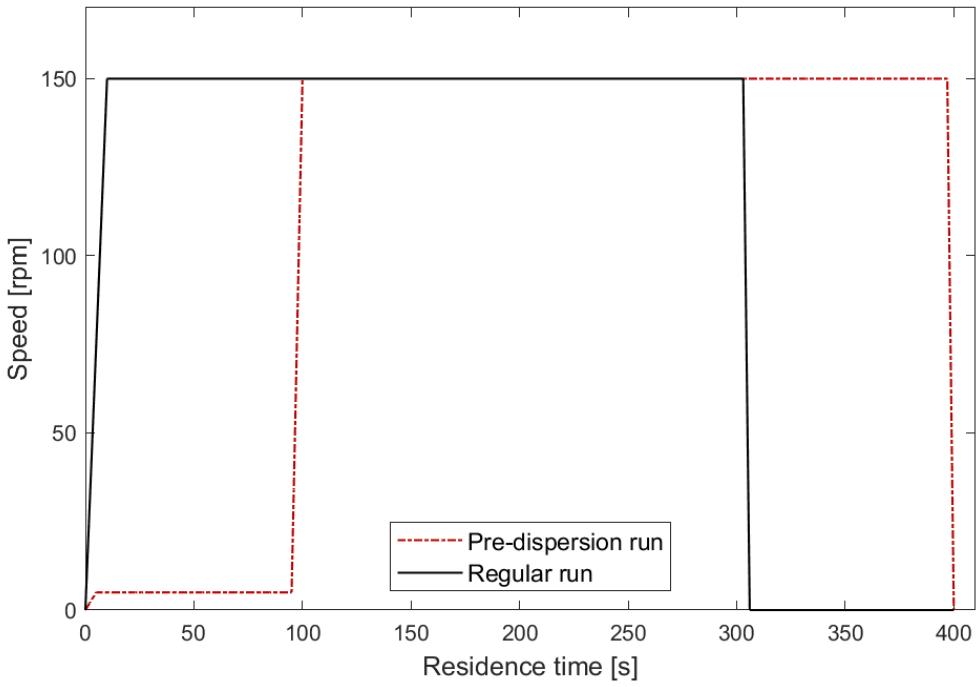

Figure 3.15 Schematic of the defined processing speed and residence time for fiber dispersion experiment

After shearing, the fiber-filled polymer was allowed to cool down, extracted from the Couette and fiber length was measured. The measurement results are presented in Figure 3.16, where both length averages L_N and L_W are compared for each test condition.

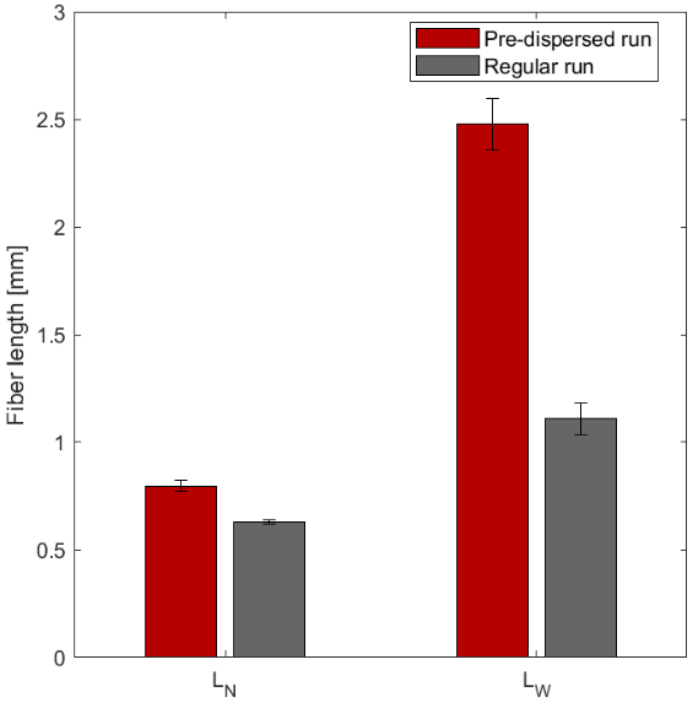

Figure 3.16 Measured residual fiber length for pre-dispersion and regular Couette runs

A clear increase in the equilibrium length is observed when the pre-dispersion step is introduced. While L_N rose close to 25%, L_W more than doubled. This marked difference between L_N and L_W implies that the resulting fiber population after the pre-dispersion run contains a considerable number of mid to long range fibers. To better illustrate this fact, Figure 3.17 present the FLD for one of the measurements.

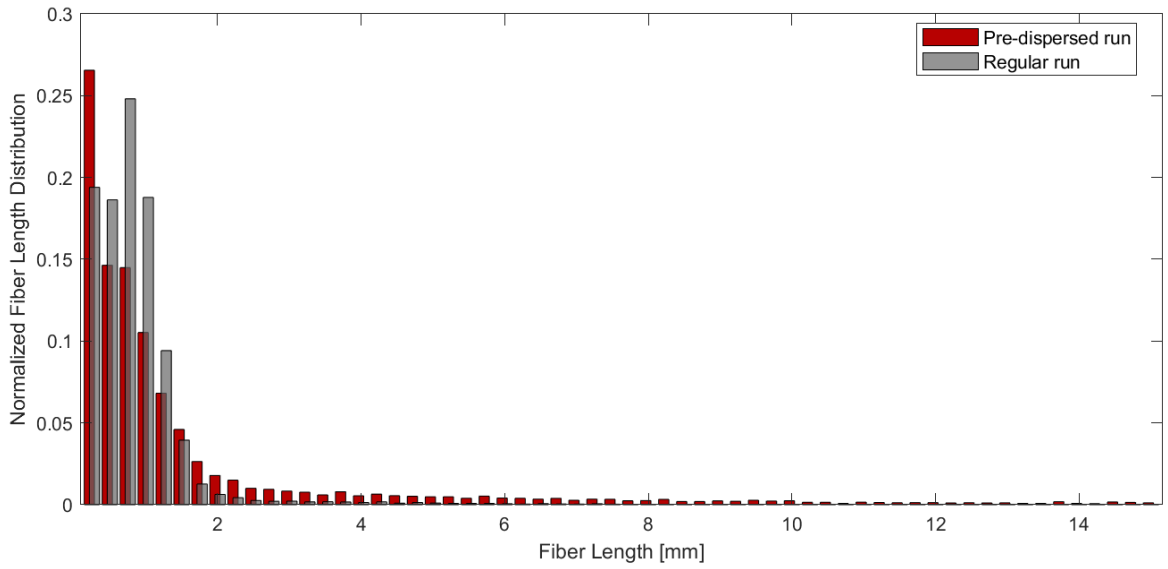

Figure 3.17 Fiber length distribution for pre-dispersion and regular Couette runs

While the peak of each FLD is located around the 1mm mark, leading to a similar L_N value; the FLD of the pre-dispersed run has a long tail reaching values close to the initial length. This means that, by first dispersing the fibers at low levels of stress, the overall degree of attrition was reduced, and very long fibers were retained until the end of the shearing cycle. From these results we can deduce that, even after removing melting effects, the compact bundles of fibers still lead to an increased level of damage.

3.4.2 Impact on attrition rate

The impact of dispersion on the initial rate of damage should be of particular interest since it is at the early stages of dispersion when most fiber damage takes place. In the previous section we mentioned the different damage mechanisms present in the melting zone during plastication. When full bundles are present, damage happens mainly at the ends of the fibers, when the drag flow shears off the tips; but when fibers are fully surrounded by matrix, drag forces cause deformation which leads to damage (Figure 3.18).

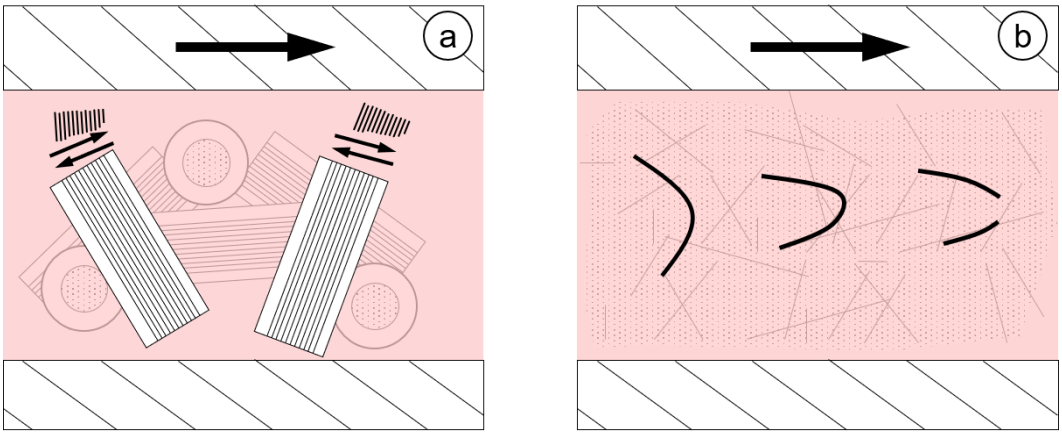

Figure 3.18 Fiber breakage mechanisms under different dispersion stages a) Undispersed fiber bundles, b) Fully dispersed fibers

The attrition rate coefficient as described by Shon et al., is a measurement of how regularly breakage occurs. Therefore, in the presence of two different damage mechanisms, the attrition rate coefficient k_f is bound to transition as the flow condition evolves from a heterogenous mix of bundles and matrix, to a fully dispersed suspension. The data set obtain from the *length decay over time* and the *attrition rate* experiments can help us establish a comparison. From the data summarized in Figure 3.10, the average value for $k_{f,N}$ and $k_{f,W}$ can be determined. These values correspond to the damage conditions illustrated in Figure 3.18,a. From the results shown in Figure 3.13 similar values can be determined for fiber damage in the dispersed suspension. Additionally, since we have identified a linear correlation between k_f and the rate of deformation, by dividing all values by $\dot{\gamma}$ we can determine the impact pre-dispersion has on the attrition rate. Table X1 lists the results of this analysis.

Table 3.5 Fiber breakage rate comparison between dispersed and undispersed fibers

Fiber state	$k_{f,N}/\dot{\gamma}$	$k_{f,W}/\dot{\gamma}$
Pre-dispersed	4.97×10^{-4}	4.66×10^{-4}
Undispersed	14.5×10^{-4}	12.1×10^{-4}

The values corresponding to the number-averaged fiber length are expected to be higher since L_N decreases faster than L_W. More importantly, these results suggest that breakage happens nearly three times more often when the fibers are not dispersed.

The overall impact that dispersion has on the fiber breakage kinetics is illustrated in Figure 3.19. Both the dynamic portion and the steady state fiber length benefit from having well dispersed fibers. These results confirm that various damage mechanisms are present during plastication; each of which leads to different levels of damage.

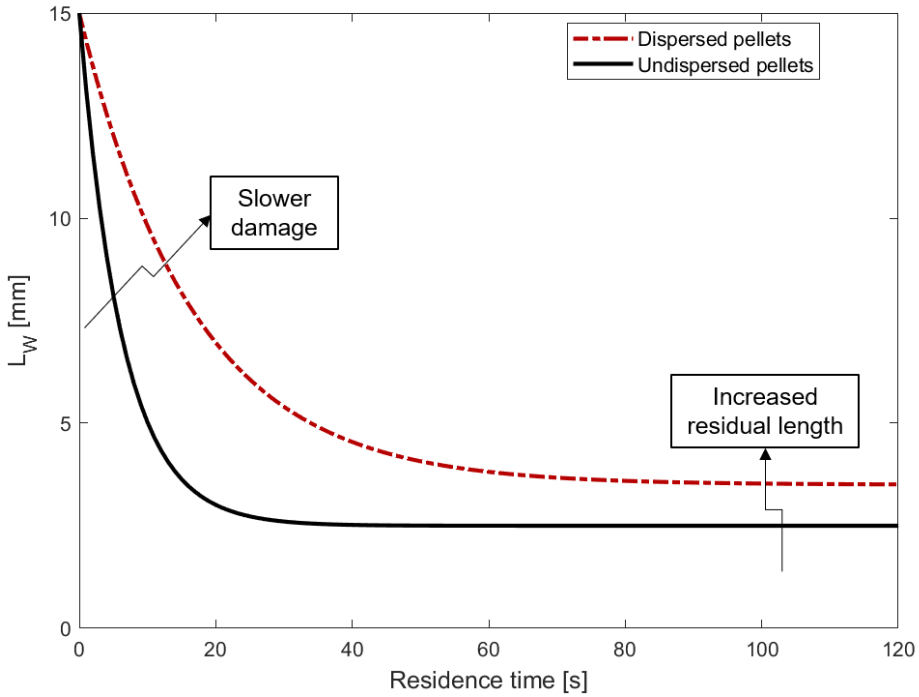

Figure 3.19 Illustration of the impact fiber dispersion has on length reduction over time in the Couette rheometer

These sets of Couette experiments have allowed us to stablish direct correlations between processing and damage. Understanding the external sources of stress and their impact on the level and rate of damage is key in the development of a model that predicts fiber attrition with accuracy. It should be noted that the simple shear flow of the Couette imparts similar stress on all of the fibers. However, the type of flow during injection molding leads to a non-constant stress profile through the thickness of the mold cavity.

This is reflected on the average length of the fibers changing along the thickness direction. Currently there are not methods for measuring difference in fiber length through the thickness of molded samples. Therefore, the next section describes the development and validation of a measuring technique that addresses this issue.

3.5 Measuring fiber length through the thickness of molded components

The characteristic flow pattern during mold filling and the no-slip condition on the mold walls cause fibers to re-orient, producing a distinctive configuration known as the core–shell structure [79, 80]. In this structure, fibers near the mid-plane do not experience strong shearing deformations and usually align transverse to the flow direction (core); large shear strains in the regions adjacent to the core cause fibers to have strong alignment in the flow direction (shells). In moldings with 50% weight fraction (%wt) long fiber reinforced PA66, Bailey and Kraft observed significantly higher fiber length in the core compared to the shell region ($L_{N(core)}$ = 1.46mm, $L_{N(shell)}$ = 0.55mm) [80]. O'Regan and Akay also identified longer fibers in the core region ($L_{N(core)}$ = 0.86mm, $L_{N(shell)}$ = 0.7mm) for 60%wt long-fiber reinforced PA66 samples [81]. The standard technique for sample isolation used in these studies involved selecting a small number of fibers with tweezers after matrix removal. Aside from the risk of short fibers being dropped or fibers breaking, the fiber population in these studies was very low (800–3500 fibers). However, to have statistical confidence, large fiber populations are required, specifically when characterizing LFTs for which the fibers' aspect ratio can vary over two orders of magnitude.

Since matrix removal is usually achieved through pyrolysis, the shortest fibers tend to fall towards the bottom as the matrix melts and burns-off [35]. Therefore, to measure FLD in either the core or the shell, such region should be isolated from the complete sample before the pyrolysis step. As the shell is generally thicker than the core and more

accessible [32], we propose measuring fiber length in the shell and indirectly calculating the fiber length in the core. The extraction of the shell is addressed in Section 3.3. Fiber length in the core can be determined as follows.

For the arbitrary LFT sample A shown in Figure 3.20, the average L_N and L_W are calculated from the complete population of fibers inside the sample's volume. Thus, it is valid to re-formulate equations 2.1 and 2.2 by grouping the addends into sub-volumes B (shells) and C (core). The number average of the entire sample $L_{N(A)}$ can then be expressed as

$$L_{N(A)} = \frac{(\sum N_i l_i)_B + (\sum N_i l_i)_C}{(\sum_i N_i)_A} \qquad 3.5$$

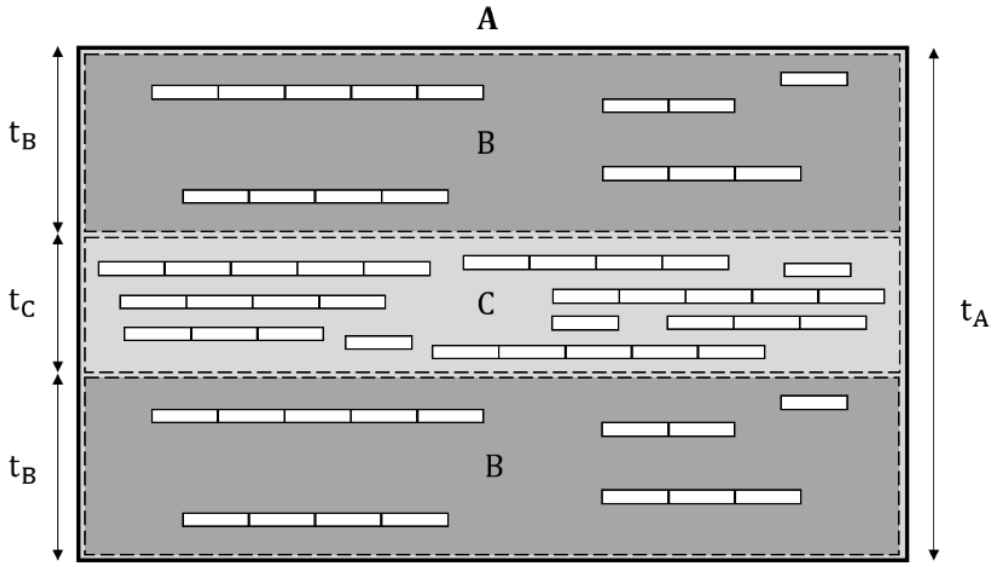

Figure 3.20 Schematic of a core–shell structure

Assuming the sample's width and length are constant, equation 3.5 can be formulated in terms of the local number-average fiber length

$$L_{N(A)} = \frac{L_{N(B)} t_B \phi_B + L_{N(C)} t_C \phi_C + L_{N(B)} t_B \phi_B}{t_B \phi_B + t_C \phi_C + t_B \phi_B} \text{ or } \frac{\sum L_{N(K)} t_K \phi_K}{\sum t_K \phi_K}, \qquad 3.6$$

where the index K represents individual layers along the thickness of the sample. The changes in fiber content (ϕ_K) have to be accounted for in order to satisfy mass conservation; that is, the total fiber length should remain unchanged. Since the objective is determining the length in the core ($L_{N(C)}$), and both the global sample length ($L_{N(A)}$) and the shell sample length ($L_{N(B)}$) can be measured experimentally, equation 3.7 can be solved for $L_{N(C)}$

$$L_{N(C)} = \frac{L_{N(A)}(2t_B\phi_B + t_C\phi_C) - 2L_{N(B)}t_B\phi_B}{t_C\phi_C} \qquad 3.7$$

The weight-average fiber length in the core ($L_{W(C)}$) can be calculated in the same way. This approach requires knowledge of the thickness of each layer and the through-thickness fiber content. This information can be obtained from μCT analysis.

3.5.1 Shell Extraction and Experimental Validation

The mathematical approach to determine the fiber length in the core is described above. However, experimental validation was required before the method could be used to measure the FLD in an actual injection molded part. Since the approach is based on extracting a single shell layer and measuring its FLD, it needs to be assured that the extraction method does not damage the fibers. For this purpose, plates with an artificial core–shell structure were fabricated via compression molding, the core FLD was determined with the mathematical approach, and the result was compared with reference samples. The material employed in this study was a 20%wt long glass fiber reinforced polypropylene (PPGF20, SABIC® STAMAX™).

First, PPGF20 pellets were extruded using a single screw extruder (Extrudex Kunstoffmaschinen, Mühlacker, Germany) and a circular 3mm diameter die, as depicted in Figure 3.21. The extrudate was cut into 50mm strands and placed on a rectangular mold with dimensions 50mm×75mm×1.1mm. The strands were aligned parallel to the shorter side of the mold. The extrudate was compression molded using a hydraulic press

(Carver 3889.1NE0, Carver Inc, Wabash (IN), USA) with heated platen at a temperature of 210°C. The resulting thin plates correspond to the core layer of the artificial core–shell sample (Figure 3.21(2))

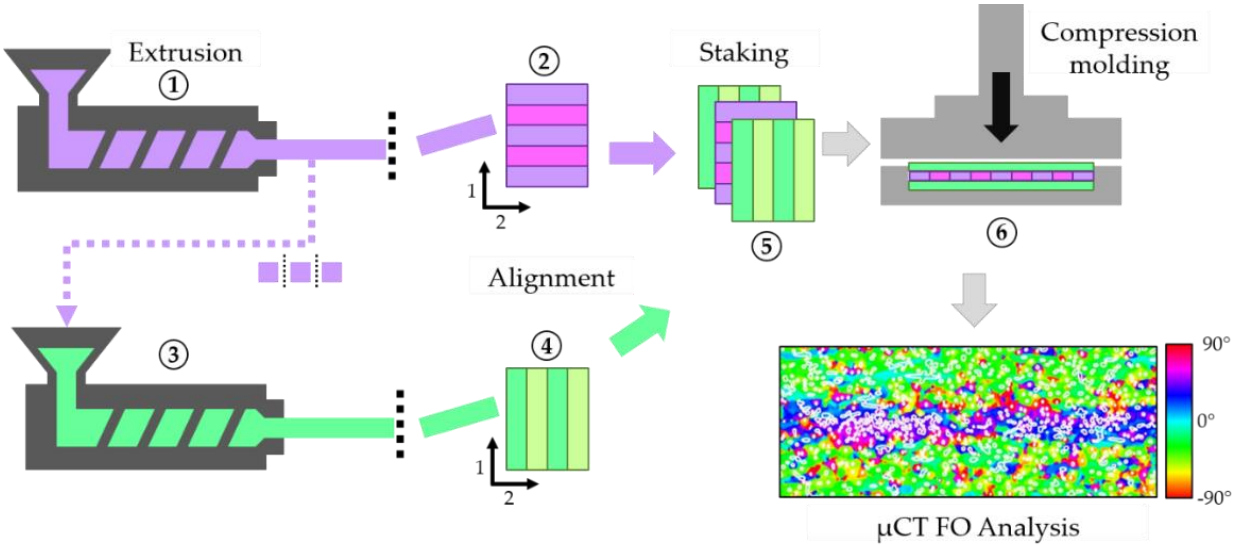

Figure 3.21 Sample preparation method for artificial core–shell plates

To have different lengths for the core and shell, a fraction of the extrudate was pelletized to a length of 3.2mm and re-extruded (3). The new extrudate was cut into 75mm long strands, and compression molded using the same mold; in this case, the strands were aligned perpendicular to the shorter side of the mold. The resulting thin plates correspond to the shell layers of the artificial core–shell sample (4). Each core plate was stacked in between two shell plates (5), and compression molded into a 3mm-thick plate (6). This small compression step aimed to fuse the layers together. For each molded plate variation, four specimens were manufactured in the hydraulic press. From each specimen, two samples were extracted and measured. The average fiber length of the core and shell plates and full stack was recorded to be used as a reference for the later validation (Table 3.6). µCT orientation analysis was performed in four specimens, which showed that distinct core and shell layers in the full stack sample were obtained (Figure 3.21).

Table 3.6 Average fiber length of compression molded plates

Region	LN (mm)	LW (mm)
Shell	0.74	1.55
Core	1.49	5.03
Full stack	0.97	2.90

Using the A_{11} tensor component as guide, the thickness of the shell layer that is to remain after the material removal can be determined (highlighted in red in Figure 3.22,a).

The material removal is a critical step since damage to the fibers in the remaining layer must be avoided. For this step, 30mm disks were cut out of the full stack sample and mounted in resin, in similar fashion to metallographic samples. The mounted samples were carefully grinded in two stages using a polishing disk (Autopolisher Metprep 3 PH-3, Allied High Tech Products Inc, Compton (CA), USA). In the first stage, an aggressive grinding cycle with a 180-grit sanding paper disk was used to remove around 90% of the material. In the second stage, a 600-grit sanding paper disk was used to remove the remaining material until the desired shell layer had been isolated. After the sanding process, the sample was removed from the resin and underwent the fiber length measurement procedure.

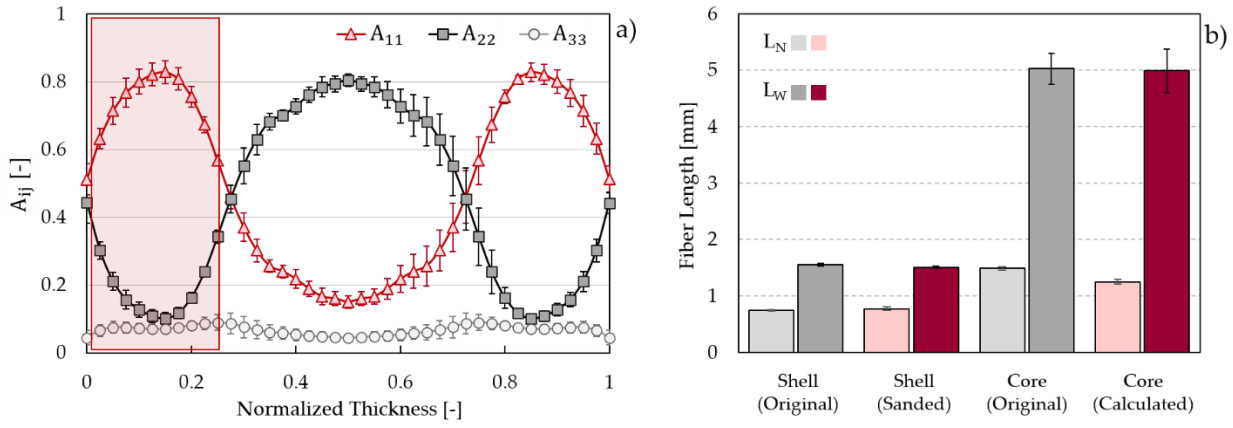

Figure 3.22 Artificial core–shell plate microstructure: (a) through-thickness fiber orientation distribution (FOD); and (b) fiber length values for individual core and shell layers

Results from this experimental validation are shown in Figure 3.22,b. From these length values, it can be concluded that the material removal step does not affect the fiber length in a significant way. The reason the fibers are not excessively damaged is the highly planar fiber orientation in the sample (low A_{33} values) [83, 84].

The main objective of this validation was to establish if the core length can be accurately determined with the approach described in Section 3.5. With this approach, the orientation data are used to find the thickness of each layer. The fiber length of the full stack sample and the sanded shell layer are used in equation 3.7 to calculate the length in the core layer. Figure 3.22,b shows the comparison between the fiber length of the original compression molded core layer and the calculated fiber length in the core layer. Based on these results, it can be concluded that the proposed approach can be used to measure fiber length in the shell and indirectly determine fiber length in the core, provided the off-plane orientation tensor component has a low value.

3.5.2 Injection Molding Plaques

A 130-ton IM machine (SM-130, Supermac Machinery, Gujarat, India) was used to mold a PPGF20 plaque with dimensions 102 mm × 305 mm × 2.85 mm (Figure 3.23). The processing parameters followed the suggested processing guidelines by SABIC® and are listed in Table 3.7.

Table 3.7 Processing conditions for injection molding (IM) trials

Molding parameter	Value
Melt temperature (°C)	250
Mold temperature (°C)	50
Back pressure (bar)	5
Injection time (s)	2
Holding pressure (bar)	300
Holding time (s)	22

Preliminary analysis of microstructure showed well-defined core–shell layers away from the gate, between locations A and B [30]. The FOD profile, FC profile, and global FLD remained unchanged between these two locations.

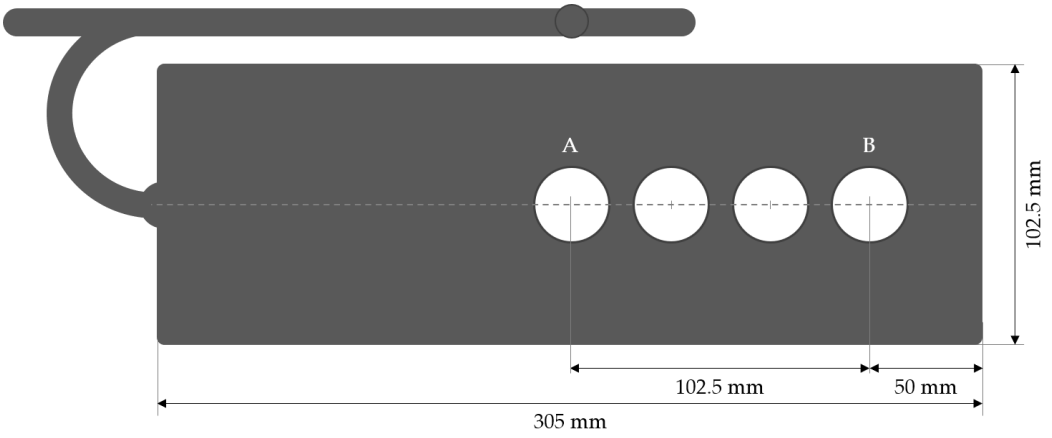

Figure 3.23 Illustration of the plaque geometry and illustration of the sample locations for microstructure analysis.

In total, 16 samples were extracted for length analysis (four samples per plaque, as shown in Figure 3.23). Half of the samples were sanded to extract the shell layer. Additionally, μCT analysis of fiber orientation and fiber concentration was performed in locations A and B for each plaque.

3.5.3 Microstructural Analysis

The simple geometry of the injection cavity leads to a well-defined and predictable microstructure away from the gate region, where the material initially moves following a radial flow [84]. The fiber orientation analysis shows a clear transition between the core and shell regions (Figure 3.24,a). For these particular injection trials, the core region covers about 15% of the sample thickness, which is expected of the PPGF20 material, as it has the lowest fiber content available commercially, and previous work has shown the thickness of the core region decreases with decreasing fiber content [32]. Unlike the artificial core–shell sample, there is a gradual transition in the orientation of the fibers

between the central and outer layers. This can be observed in Figure 3.24,b, which shows the 1-2 plane fiber orientation of section A-A. This section is slightly below the start of the core region, and yet it shows a wide range of colors associated to the fiber orientation.

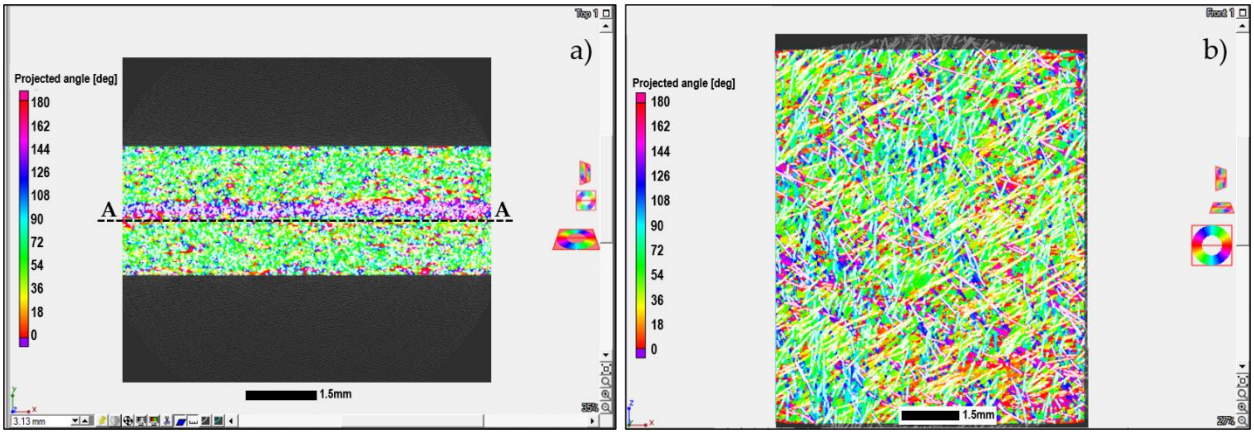

Figure 3.24 Reconstruction of fiber structure from micro-computed tomography (μCT) analysis using VG StudioMAX: (a) 2-3 plane cross section; and (b) 1-2 plane section A-A

Figure 3.25,a shows the diagonal orientation tensor components through the thickness of the plaque. Again, the characteristic core–shell structure is visible, as well as the low values of the A_{33} tensor component. The A_{33} value averaged over the sample thickness of the injection molded sample is 40% lower than the one measured in the artificial core–shell sample. These low values of the off-plane orientation tensor component are required for the length measurement approach to work.

Figure 3.25,b shows the through-thickness fiber weight fraction. This microstructural variable also varies between the central and the outer regions. As it goes through the core region, there is a significant increase in fiber content, which is linked to the high level of alignment and little motion of the fibers in the low shear core region [85].

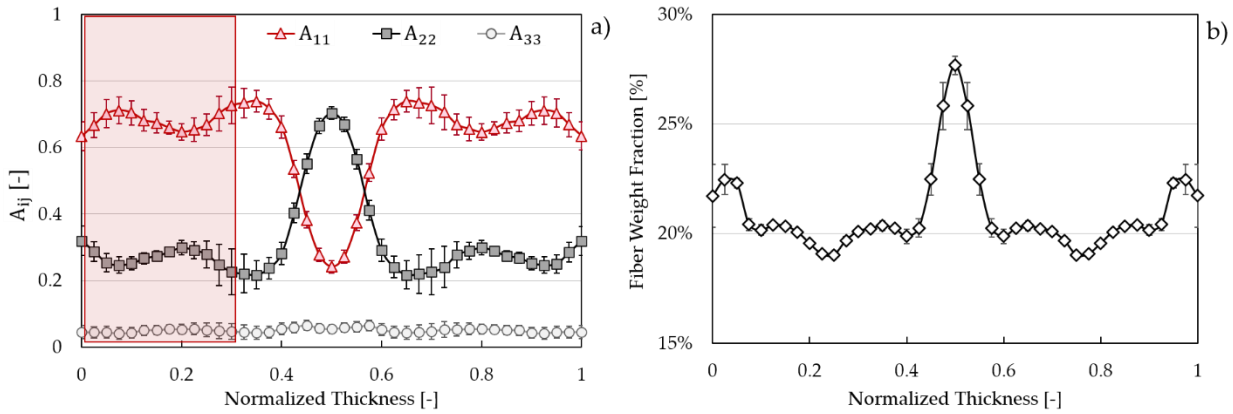

Figure 3.25 Injection molded plaque microstructure: (a) through-thickness FOD; and (b) through-thickness fiber content (FC)

It has been suggested that uneven temperatures in the mold walls result in an unsymmetrical through-thickness microstructure [37, 50]. The injection trials in the present work, however, showed good symmetry and are therefore considered symmetrical with respect to their mid-plane; one side of the plaque is thus a mirror image of the other.

Employing the orientation data, the shell layer to be extracted was identified (highlighted in red in Figure 3.25,a). In this case, the extracted layer was slightly thinner than the shell region. This is to avoid measuring fibers shared by both regions. To account for the gradual transition in the microstructure, rather than calculating an average value for the core region, a distribution was used to recreate the fiber length (equation 3.8). The base line for the distribution is the fiber length measured in the shell. The spread of the distribution (σ) was adjusted to match the core thickness determined from the information in Figure 3.25. A factor (f) was included to scale the height of the distribution's peak until the global fiber length calculated through equation 3.8 matched the experimental measurement.

$$L_N = L_{N(shell)} + \left[f \times e^{-\left(\frac{x-0.5}{\sigma}\right)^2} \right] \qquad 3.8$$

As this fiber length calculation requires the through thickness fiber content values, the fiber content in the shell region was averaged, since small variations of fiber content in the shell do not imply a change in fiber length. The resulting fiber length profiles are presented in Figure 3.26.

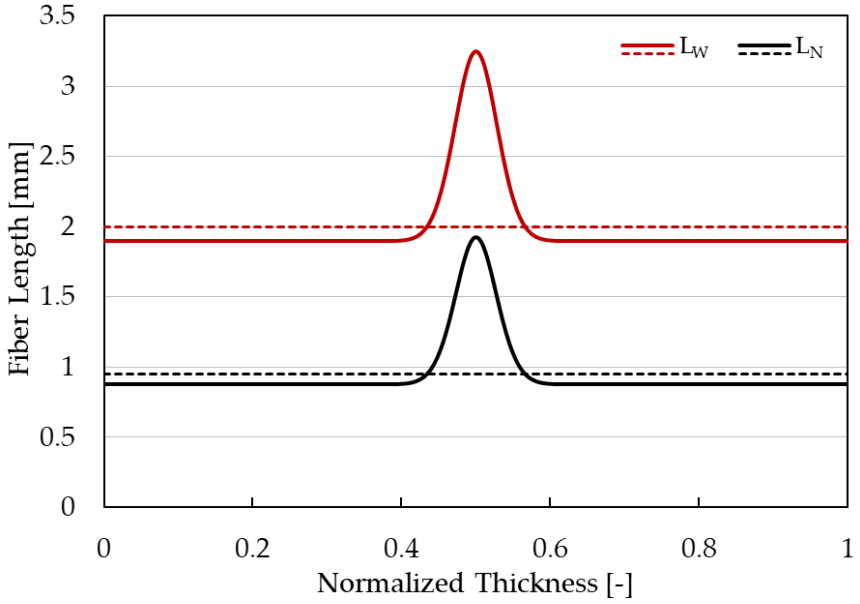

Figure 3.26 Experimentally determined through-thickness fiber length distribution (FLD) for the injection molded plaque. Dashed lines show global fiber length measured over the whole part's thickness

3.5.4 Comparison with Length Prediction Model

While various studies develop empirical correlations to describe fiber attrition [62], [76], very few mechanically based models have been used in mold filling simulations. Currently, the Phelps–Tucker model is the only one implemented in commercial software [60]. This model for fiber attrition is based on buckling failure as the driving mechanism for fiber breakage. The model uses three fitting parameters: ζ is the fiber drag coefficient which impacts the unbreakable length or steady state of the breakage process; C_B is the fiber breakage coefficient, which is a scale factor for the rate of deformation and impacts the transient portion of the breakage process; and S defines the shape of the final FLD.

Moldex3D™ (Version R17, Moldex3D, Zhubei City, Taiwan) was used to run a mold filling simulation of the injection molded plaque. Process parameters were set to match

the processing settings listed in Table 3.7. The Phelps–Tucker model parameters were manually adjusted to find a good agreement with the global fiber length measured experimentally. Additional to the three parameters, the initial fiber aspect ratio needs to be defined. The approximate nominal fiber length of 15mm was used as the initial fiber length, and screw-induced fiber breakage was considered. Model parameters and initial aspect ratio are listed in Table 3.8.

Table 3.8 Input values for Phelps–Tucker model parameters

Parameter	Value
Aspect ratio	700
ζ	1.1
CB	0.015
S	0.25

Figure 3.27 shows the through thickness L_W for both, experimental and predicted data. While the experimental length data were determined based on the thickness of the core region, the predicted length comes from a hydrodynamic stress-based failure criterion. Therefore, the predicted length profile follows the changes of the shear rate (Figure 3.27). Averaging the predicted L_W over the shell gives a length value just 10% lower than the experimental measurement.

If the flat, low shear region in Figure 3.27 can be interpreted as the core, its thickness closely resembles the experimental core thickness. However, this variable is not dependent on the fiber attrition model. Instead, the coefficients of the Cross-WLF viscosity model used for this material are what determines the thickness of the core [86]. The predicted fiber length in the core is constant and its value is greater than the experimental L_W averaged over the core region.

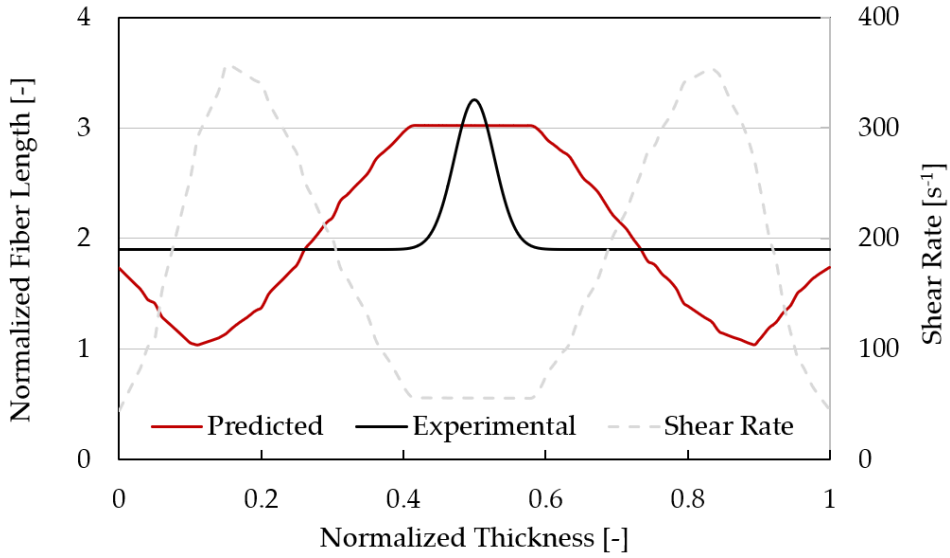

Figure 3.27 Comparison of experimental and predicted through-thickness FLD

By using optimized fitting parameters, we are comparing the through-thickness variation of the FLD, rather than validating the accuracy of the model. The average length obtained with Moldex3D™ default parameters, underpredicted the fiber length in the region. One reason the simulation overpredicts damage with its default parameters, is due to the model's negligence of the fiber concentration effect on the rate and level of fiber damage [60]. Recent experimental studies have shown that damage increases as the nominal fiber content is increased [21, 62].

3.5.5 Impact on Stiffness

The three microstructural variables considered until now have independent impact on the mechanical properties of the bulk material. Translating the microstructural data obtained through mold filling simulations into mechanical properties, is a critical step in the design process when using discontinuous fiber composites. To achieve this, a complex two-phase microstructure is homogenized through different micromechanical approaches to generate effective mechanical constants, that can then be used in traditional FEA simulations [87]. Many micromechanical models for non-dilute composite materials have evolved from a model originally proposed by Mori and Tanaka

[88]. Tandon and Weng [89], for example, used the Mori–Tanaka approach to develop equations for the complete set of elastic constants of a short-fiber composite. Their equations describe the change of the elastic constants as function of aspect ratio and volume fraction.

The through-thickness FOD, FLD and FC were discretized into layers and used to create a representative volume element (RVE) using Digimat–MF, a mean field homogenization tool. For each layer, the tool uses as input the full orientation tensor, the fiber volume fraction, the aspect ratio distribution, and the mechanical properties of each of the phases. The Mori–Tanaka homogenization model was used to determine the stiffness constants for each individual layer and the RVE. The Mori–Tanaka model is accurate in predicting the effective properties of two-phase composites for moderate volume fractions of inclusions (around 25%). Since the maximum volume fraction measured in the sample was below 12%, it is appropriate to use the Mori–Tanaka model for the stiffness analysis.

To evaluate the impact of having through-thickness length data, a reference RVE was created. It had identical fiber orientation and fiber volume fraction, but with constant fiber length over the thickness. Figure 3.28 shows the aspect ratio distribution recreated from the experimental measurements for the global sample and the core and shell, independently. Since the core layer in the injection trials is thin, there is little change in the shape of the distribution between the global and shell data. The core layer in contrast has a considerable shift to the right and a wider spread compared to the global data.

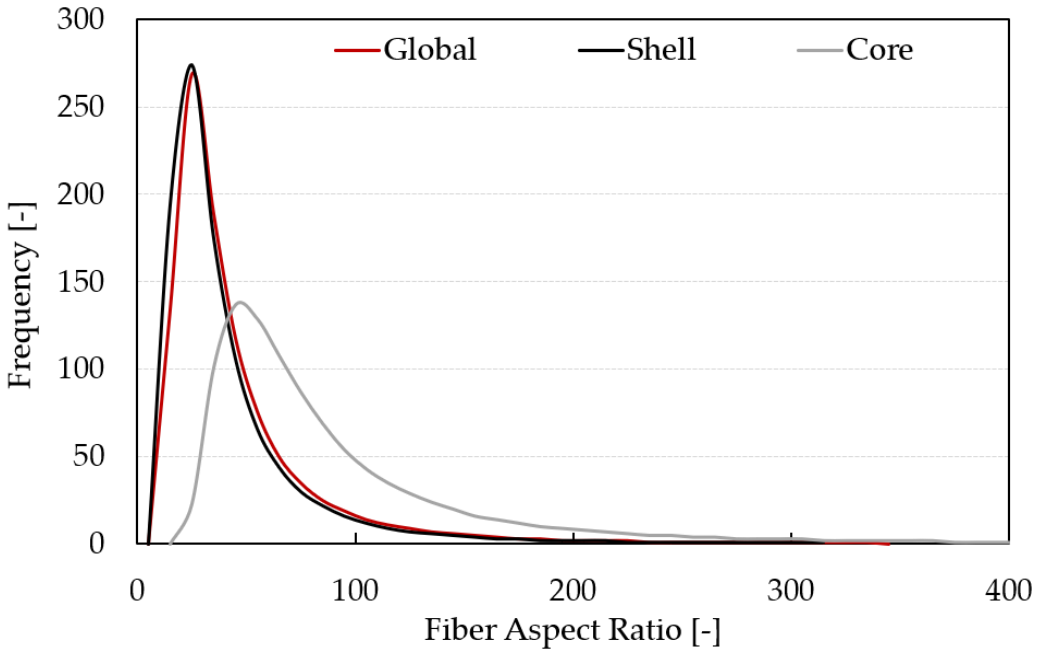

Figure 3.28 Aspect ratio distribution for the global sample, and the core and shell regions

Table 3.9 lists the relevant longitudinal and transverse Young's modulus for the core and shell regions. In the regions marked as "Global", the global FLD was used (red line in Figure 3.28), and the regions marked as "Varying" used the local FLD. As expected, there is negligible change in the longitudinal stiffness in the shell, since the change in the FLD is small. Nguyen et al. performed a sensibility analysis introducing small variations to the shape of the FLD, and they concluded this had little to no impact in the mechanical properties [82]. A comparatively larger change of about 5% is observed in the transverse stiffness in the core region.

Table 3.9 Longitudinal and transverse Young's modulus for the core and shell layers

Region	$\mathbf{E_{11}}$	$\mathbf{E_{22}}$
Shell (Global)	6243	-
Shell (Varying)	6218	-
Core (Global)	-	7418
Core (Varying)	-	7857

Stress–strain curves in the longitudinal and transverse directions for the RVE are plotted in Figure 3.29. The small local change of E_{22} in the core layer is effectively dissolved in the RVE, which shows no significant change of stiffness in either of the directions.

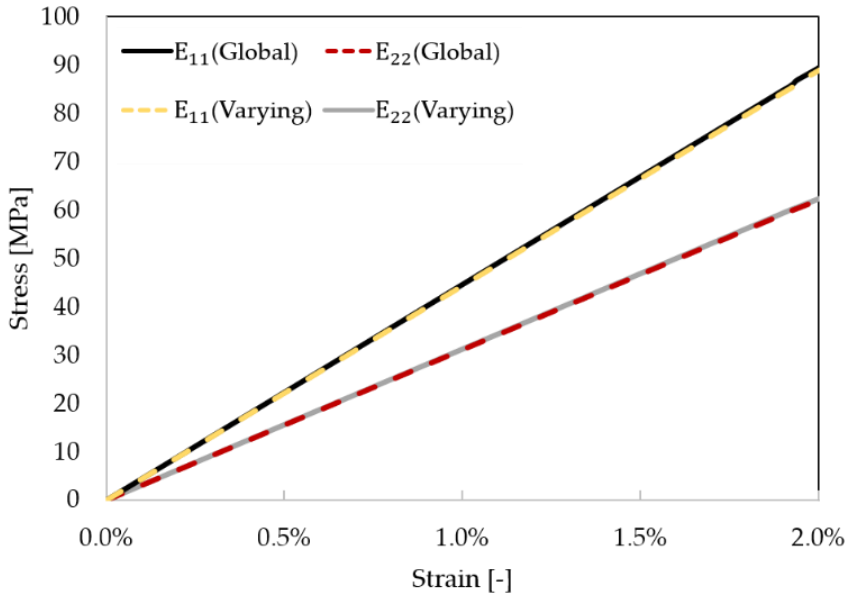

Figure 3.29 Stress–strain curves for representative volume element (RVE) with global fiber length and with varying fiber length.

Since the global average aspect ratio for these injection trials is higher than 50, little change can be expected in the stiffness constants with increasing fiber length. Tandon and Weng theoretical equations show that these stiffness constants (E_{11}, E_{22}) had little variation at aspect ratios above 50. However, obtaining detailed fiber length information is valuable for our simulation efforts (Section 4.3), since this data provides a better point of comparison and validation for the model predicting fiber damage.

4 Modeling Fiber Damage

4.1 Model development

Based on the analysis of the experimental results and reviewed previews work, we now present the main arguments for the development of a new modeling approach for stress induced fiber damage during injection molding of LFT materials.

i. von Turkovich et al. conducted studies on compounding of SFTs employing a single screw extruder [50]. One main conclusion was that fiber content does not have a significant effect on fiber attrition. Partly based on their conclusion, Phelps et al. neglected fiber interactions as a source of damage and defined buckling as the sole mechanism triggering failure [60, 86] However, high stresses and complex flow conditions present during the extrusion process make it hard to confidently establish direct correlations between fiber length and individual factors.

ii. While the hydrodynamic stresses will certainly cause buckling, which might lead to failure in short fibers; in average, much larger deformations are needed to cause breakage of the E-glass fibers commonly used in LFTs (D≈20μm). As shown by Salinas and Pittman, fibers can reach large deformations, far beyond the point of buckling before finally breaking [22]. Additionally, measurements of critical radii via loop test for E-glass fibers showed that very small curvatures can be reached before fracture occurs [64].

iii. The experiments under controlled processing conditions employing the Couette rheometer, showed a significant correlation between fiber volume fraction and the

steady state length [62]. While Moritzer concluded that fiber content impacts both the attrition rate and the steady state length, our results suggest the fiber content has a weak impact on the attrition rate coefficient.

We postulate the average fiber length reduction over time follows an exponential decay towards an equilibrium value as suggested by Shon et al. A state equation can then be written for each length average L_N and L_W. This will allow to reconstruct the fiber length distribution at any point in time.

$$\frac{dL_N}{dt} = -k_{N,f}\left(L_N - L_{N,\infty}\right) \tag{4.1}$$

$$\frac{dL_N}{dt} = -k_{N,f}\left(L_N - L_{N,\infty}\right) \tag{4.2}$$

We now move on to deriving expressions for both parameters of the state equation L_∞ and k_f; understanding that the equilibrium length is reached when external stresses are balanced with the internal resistance of the fibers. While k_f dictates how often failure occurs.

4.1.1 Equilibrium length

As we understand a single fiber undergoes bending deformation caused by the hydrodynamic drag of the moving melt, we represent a fiber at the brink of rupture as a cantilever beam subjected to a distributed load as depicted in Figure 4.1.

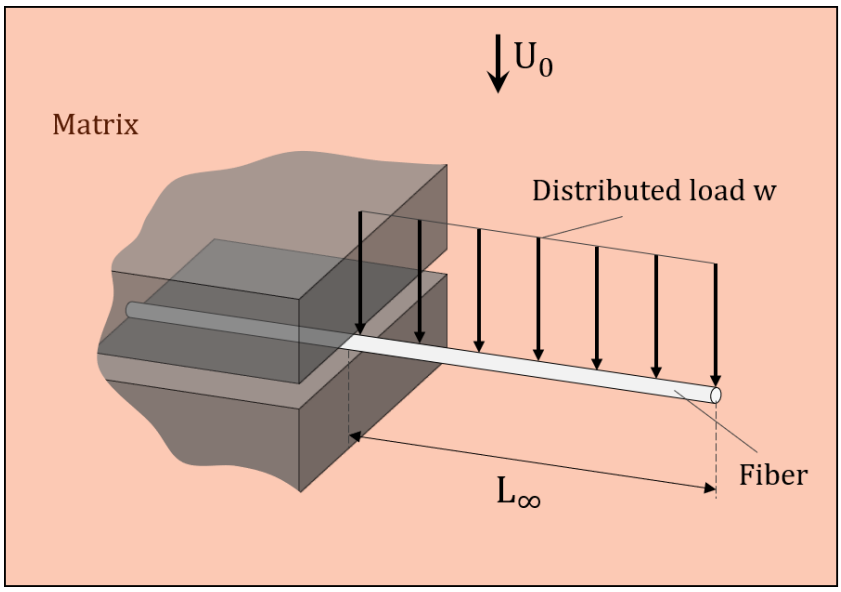

Figure 4.1. Illustration of a fiber experiencing distributed load due to drag force.

This leads to the following expression for the critical length L_∞:

$$L_\infty = \left(\frac{\sigma_{ut} d_f^3}{48\eta_m U_o}\right)^{1/2} \tag{4.3}$$

The characteristic shear rate can be defined as $\dot{\gamma} = U_0/h$, where h is introduced to describe a characteristic distance, such as channel depth, runner size or cavity thickness.

$$L_\infty = \left(\frac{\sigma_{ut} d_f^3}{48\eta_m \dot{\gamma} h}\right)^{1/2} \tag{4.4}$$

Assuming that h is proportional to d_f, $h \propto d_f$,so that:

$$L_\infty \propto \left(\frac{\sigma_{ut} d_f^2}{48\eta_m \dot{\gamma}}\right)^{1/2} \tag{4.5}$$

The proportionality can be resolved by introducing a dimensionless constant, λ, which gives:

$$L_\infty = \lambda\left(\frac{\sigma_u\, d_f^2}{\eta_m \dot{\gamma}}\right)^{1/2} \tag{4.6}$$

The parameter λ, is a material dependent property and a measure of fiber interactions that cause fiber attrition during processing. The parameter is assumed to capture the effects of fiber concentration (fiber-fiber interactions) and fiber-wall interactions. Figure 4.2 shows the parameter λ as a function of fiber content as obtained from the measured $L_{W,\infty}$ values of the Couette rheometer experiments.

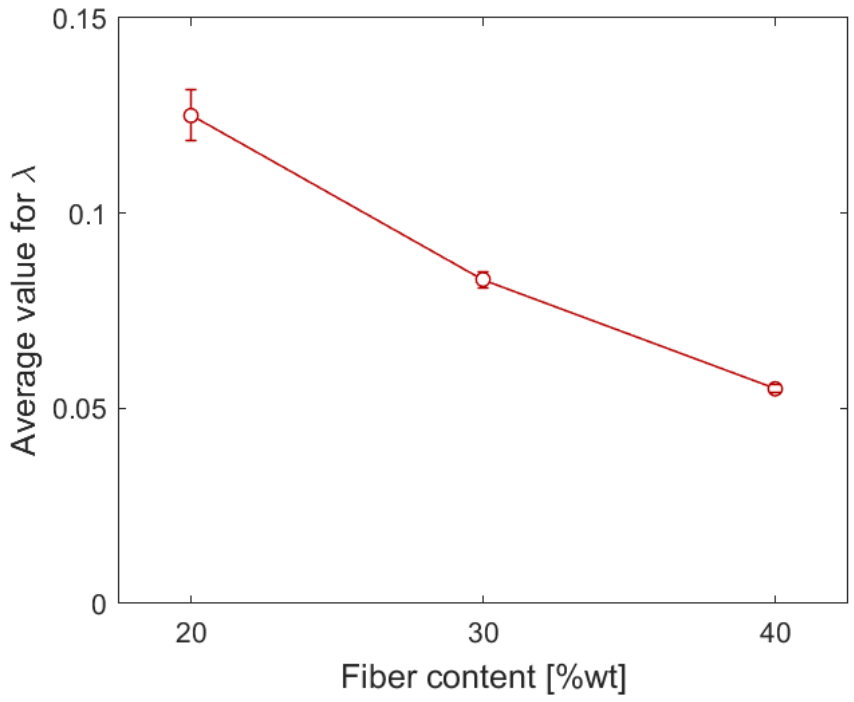

Figure 4.2. Average parameter λ as function of fiber concentration

4.1.2 Breakage rate

The parameter k_f can also be calculated from the Couette rheometer experiments. An analysis of variance applied to k_f to determine its variation with respect to fiber concentration and shear rate is presented in Figure 4.3. While the fiber concentration does not have a statistically significant impact on the breakage rate coefficient, shear rate does.

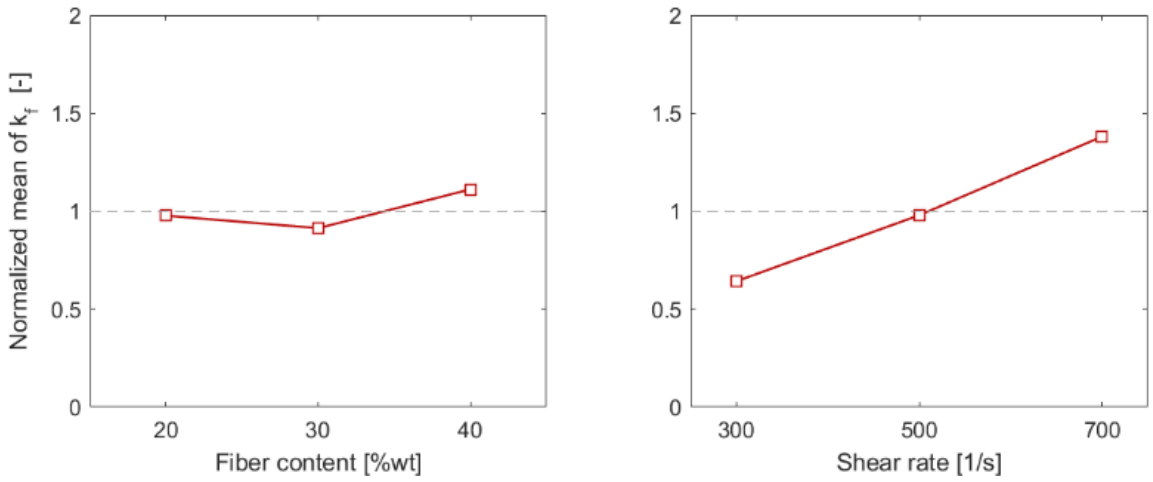

Figure 4.3. Result of the statistical analysis showing main effect plots on k_f

In the current modeling approach k_f represents how often fibers will reach the critical conditions described in the formulation of L_∞. We argue this frequency is proportional to the amount of fiber motion, $k_f \propto \dot{\gamma}$, caused by the flow as described by Forgacs and Salinas. The linear correlation between $\dot{\gamma}$ and k_f shown in Figure 4.3, leads to a straightforward expression for the breakage rate coefficient:

$$k_f = \xi \dot{\gamma} \tag{4.7}$$

4.1.3 Constitutive model

The proposed model uses two fitting parameters: ξ, which scales $\dot{\gamma}$ in the breakage rate coefficient formulation, and λ, which encapsulates the effects of fiber interactions, and is a function of the fiber concentration. An independent set of fitting parameters must be used for the constitutive equations in terms of L_N and L_W. The definition of both parameters in terms of processing conditions and material properties allows for the constitutive equations to be written in terms of the total derivative and implemented in a cavity filling simulation where the flow field information is used to calculate the model constants to predict the fiber length.

$$\frac{dL_N}{dt} + (u \cdot \nabla)L_N = -k_{f,N}(L_N - L_{N,\infty}) \quad 4.8$$

$$\frac{dL_W}{dt} + (u \cdot \nabla)L_W = -k_{f,W}(L_W - L_{W,\infty}) \quad 4.9$$

The FLD can be reconstructed by employing a probability density function (PDF) and optimizing its parameters so the mean and the weighted mean of the distribution match L_N and L_W respectively. To find a distribution that can appropriately capture the shape of the FLD we must consider how the fiber damage kinetics can modify the fiber length population. Ideally, all fibers start with the same length of L_0, this initial condition can be represented as a Dirac delta at location L_0. When breakage starts, small fragments from the fiber tip break first, therefore a second wider peak starts to appear toward the left side of the distribution.

Since a few long fibers can survive the shearing process, the final distribution will be skewed with a long tail toward the longer fiber side. Based on this, a Gaussian distribution would not be suited to represent the FLD. However, there are a number of skewed distributions that can be used. To find an optimum shape, 8 different types of distributions were evaluated versus a FLD obtained from a Couette experiment. In this case, the initial experimental fiber length was 12.5mm, therefore this value delimits the fiber length population. Figure 4.4 and Figure 4.5 show the comparison of the cumulative length distribution (CLD) obtained from the Couette experiment and the recovered CLD for each of the theoretical distributions.

Each of the selected distributions has between 1 and 3 parameters, they usually control the shape, scale, and peak location of the distribution. These parameters are use as the iterative quantities to find the best fit. Table 4.1 lists each distribution and the role of its parameters.

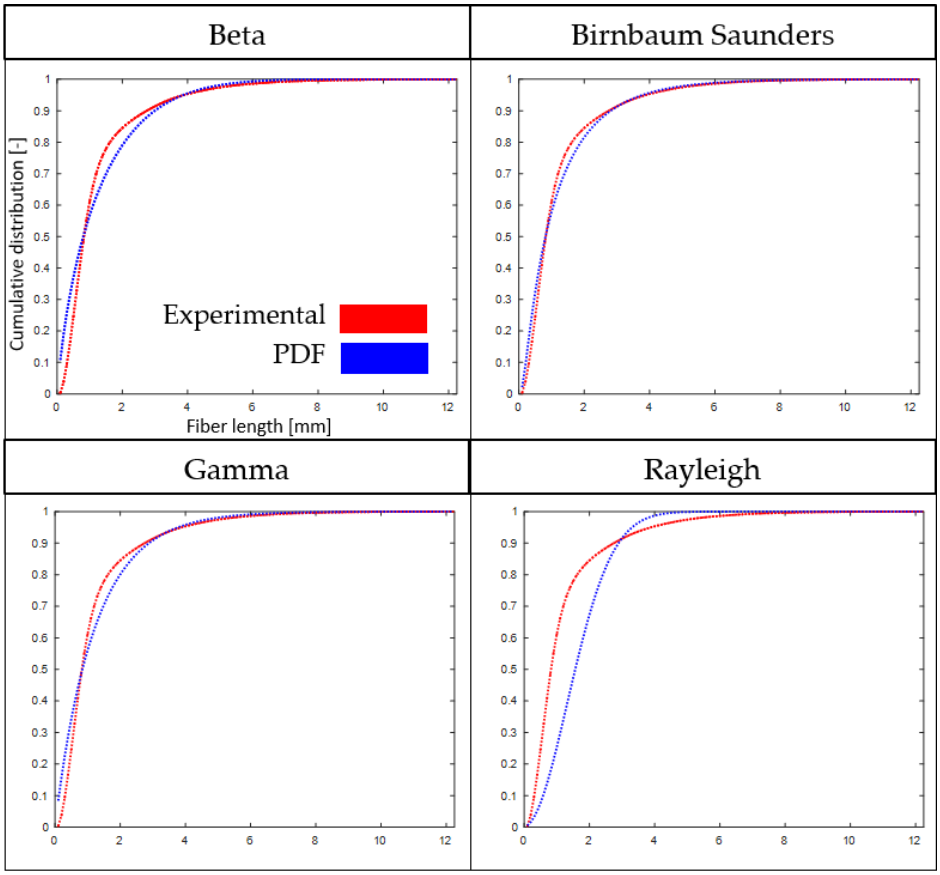

Figure 4.4 Cumulative probability distribution functions compared to experiments fiber length, part 1

Table 4.1 Evaluated probability distribution function parameters and their role

Distribution	Parameter 1	Parameter 2	Parameter 3
Beta	$\alpha > 0$ shape	$\beta > 0$ shape	-
Birnbaum Saunders	γ shape	μ location	$\beta > 0$ scale
Extreme value	ξ shape	μ location	$\sigma > 0$ scale
F	$d_1 > 0$	$d_2 > 0$	← deg. of freedom
Gamma	$k > 0$ shape	$\theta > 0$ scale	-
Rayleigh	$\sigma > 0$ scale	-	-
Weibull	$k > 0$ shape	$\lambda > 0$ scale	-
Burr	$c > 0$ shape	$k > 0$ shape	-

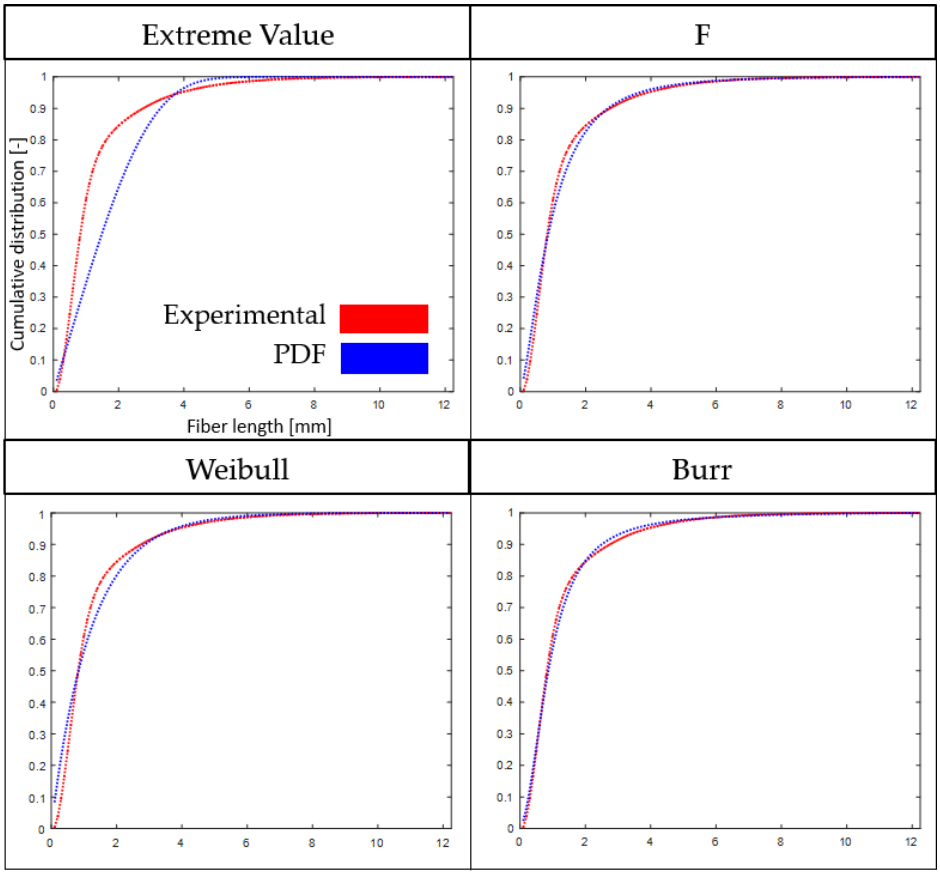

Figure 4.5 Cumulative probability distribution functions compared to experiments fiber length, part 2

Since the target values for the parameter optimization operation were the average values (L_N, L_W), there is a good agreement between the PDFs and the experimental data. As can be observed in Figure 4.6 and Figure 4.7.

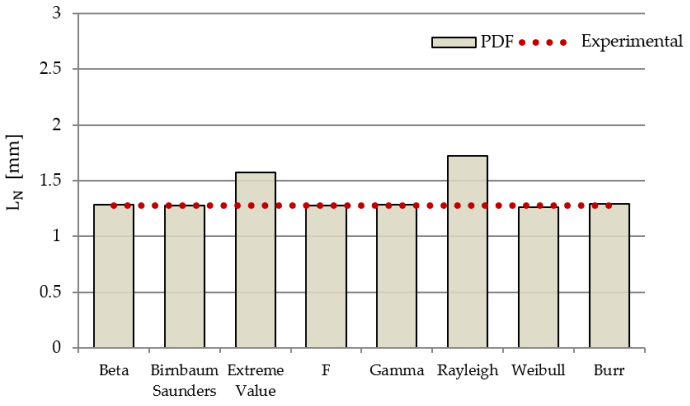

Figure 4.6 Comparison between target L_N and recovered L_N for various PDFs

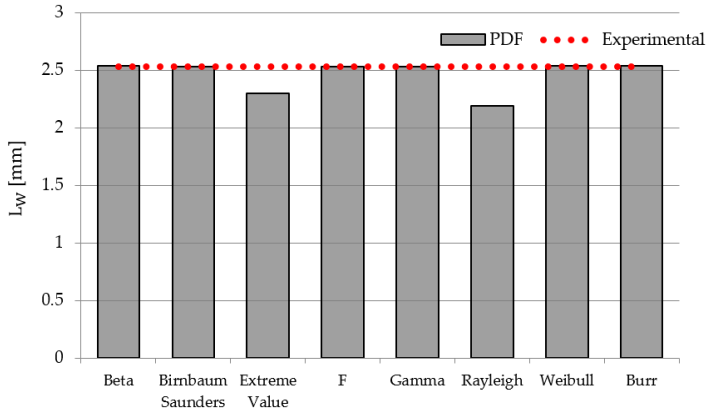

Figure 4.7 Comparison between target L_W and recovered L_W for various PDFs

However, when the evaluation criterion is the point-to-point error represented by the loss function, it becomes clear that Birnbaum Sanders, F and Burr PDFs better capture the experimental values (Figure 4.8).

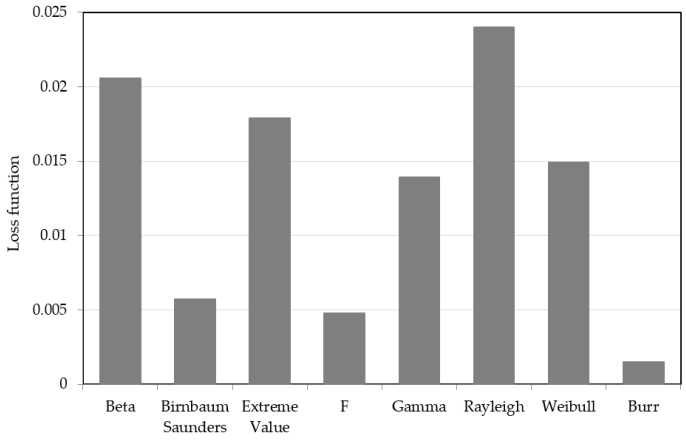

Figure 4.8 Loss function comparison for various PDFs versus experimental data

Based on the loss function analysis and its simplicity, the Burr PDF was selected to recover the FDL. Burr is a continuous probability distribution for a non-negative random variable commonly used in economics. It is expressed as:

$$f(x) = ck\frac{x^{c-1}}{(1+x^{c})^{k+1}} \qquad 4.10$$

For its use in the context of FLD, x is the fiber length, which ranges $0 < x < L_0$.

4.2 Model validation

To test the performance of the proposed fiber attrition model, it will be first compared to fiber length measurements from a Couette experiment, and accuracy in predicting both the attrition rate and the equilibrium length will be evaluated. Since the fiber length measurements from various Couette studies was used to find the fitting parameters $\lambda(\phi)$ and ξ, an independent set Couette experiments will be used as reference for comparison. However, since the initial sample is composed of undispersed bundles, the parameters ξ_N and ξ_W used in this validation corresponds to the values determined from the experiments in section 3.3, where the pellets were initially undispersed at the start of the shearing cycle.

The processing conditions for the reference Couette experiments are listed in Table 4.2.

Table 4.2 Processing conditions for Couette experiment

Parameter	Value
Melt Temperature [°C]	222
Residence time [s]	30-300
Fiber concentration [%wt]	30
Speed [rpm]	160

These processing conditions are rather extreme since the temperature is near the lower bound recommended by the material supplier and the rotational speed was set to the maximum rpm of the Brabender Plasti Corder™ torque rheometer. This places the processing conditions right at the bound of the design space from the fiber breakage DOE.

From the processing conditions listed in Table 4.2; the flow conditions, input for the model can be calculated. Given the geometry of the Couette, the rate of deformation is $\dot{\gamma} = 58.64\ s^{-1}$, the corresponding matrix viscosity is $\eta_m = 135.38\ Pa \cdot s$, the initial length is $L_0 = 15mm$, and the maximum residence time is $t_R = 300\ s$. Finally, since the velocity

profile is constant and there are no changes in the z and θ directions, the convective term in equations 4.8 and 4.9 is not included and the length decays following equation 2.6.

The comparison between experimental and predicted fiber length is presented in Figure 4.9. As expected, the equilibrium length is well captured by the model for both length averages L_N and L_W.

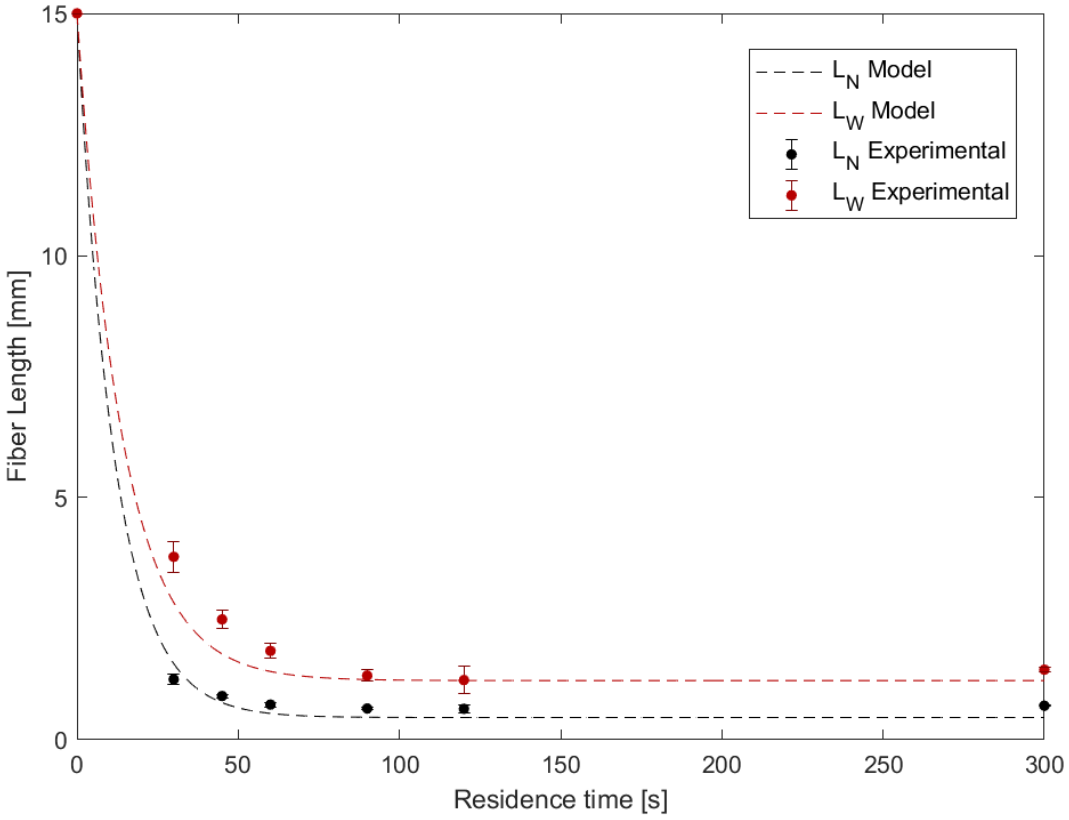

Figure 4.9 Fiber length decay for experiment employing the Couette rheometer and fiber breakage model

It is difficult to establish comparisons in the dynamic portion of the length decay since there are few experimental points. However, we can observe the rate of attrition shows a good agreement for L_W, but it seems to be under predicted for L_N. Normally, L_N values change quickly during shear, this change is difficult to measure, and this is reflected in the estimation of the fitting parameter ξ_N. Nevertheless, the model captures

the overall behavior well. The length averages are now used to recover the FLD, and the resulting Burr PDF is presented in Figure 4.10.

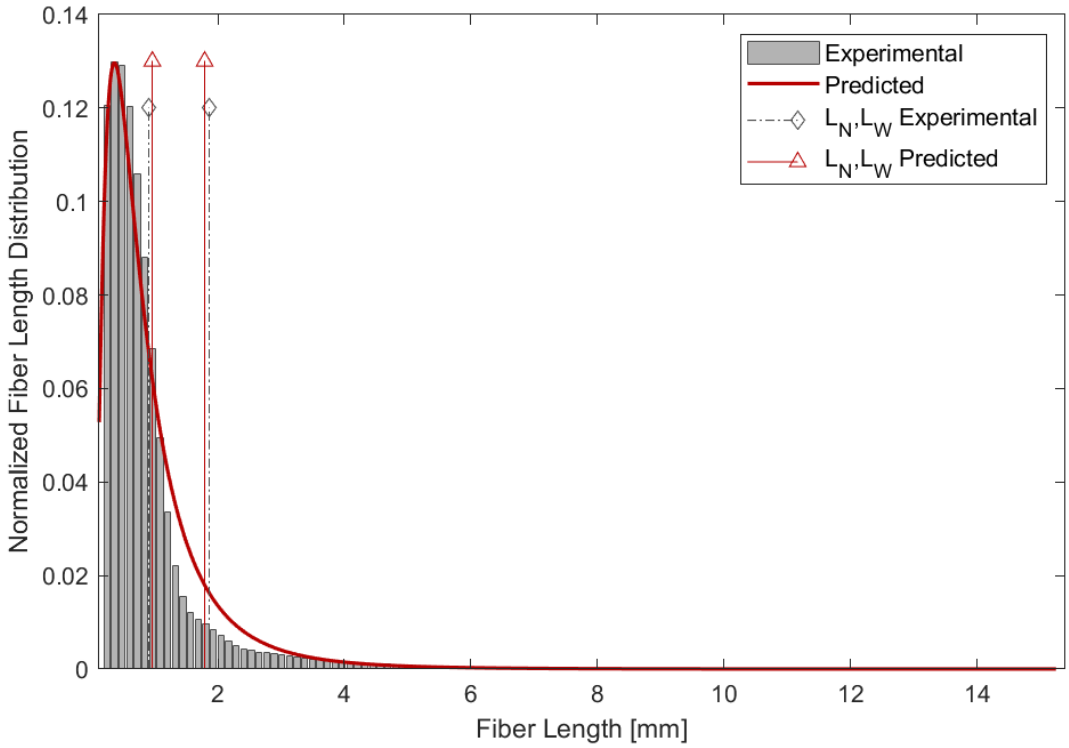

Figure 4.10 Recovered fiber length distribution employing Burr PDF versus experimental distribution

In work by Nguyen et al. a Weibull and a Log-normal PDF were used to reproduce the FLD and yielded elastic constants very close to those obtained from experimental measurements [90]. However, the authors noted that when using probability distributions, the quantity of mid-range fiber lengths is often overpredicted. This can also be observed in our results, as the continuous distribution diverts form the experimental data near the 2mm mark. This discrepancy has little to no effect in the predicted elastic constants, however in can have more impact in the prediction of the ultimate strength and impact strength.

4.3 Computational implementation

We have implemented our fiber length model in conjunction with COMSOL Multiphysics. This software allows to couple, non-Newtonian flow, heat transfer, and multi-phase flow in a single simulation. The mold geometry is a 180mm diameter center-gated disk (Figure 4.11). This geometry is often use in simulation studies as it can be simplified into a 2D axisymmetric problem. We use the suspension viscosity, in place of the matrix viscosity when calculating fiber breakage. This is done to obtain a realistic flow profile during mold filling. The viscosity is calculated using a cross-WLF model, and the model parameters were provided by the material supplier.

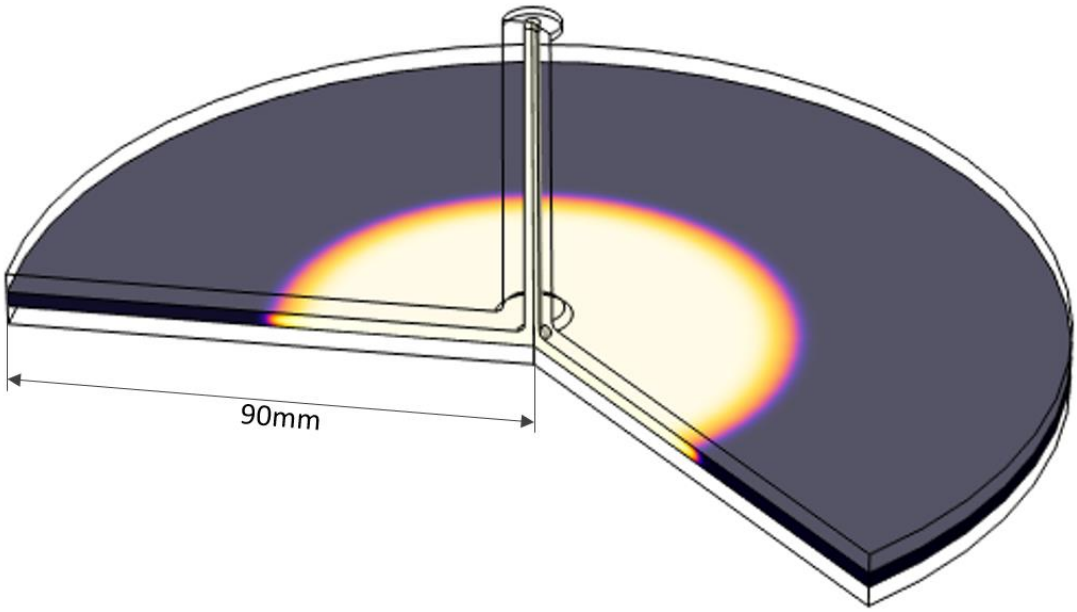

Figure 4.11 3D view of partial filling of center gated disk

At this stage of development, any changes in the suspension's rheology due to changes in fiber length are neglected. This means the fiber length simulation and flow simulation are de-coupled.

The process conditions for the simulation are listed in Table 4.3. Both, melt and mold temperatures are within the range suggested in the processing guidelines. The filling time was selected to produce high levels of shear stress inside the cavity, to causing visible damage to the fibers. The mold thickness was varied from 1.8mm to 3.0mm to evaluate the impact average stress levels have on the fiber breakage phenomena.

Table 4.3 Processing conditions for injection molding (IM) simulation

Parameter	Value
Melt Temperature [°C]	250
Filling time [s]	0.65
Fiber concentration [%wt]	30
Mold temperature [°C]	60
Initial fiber length [mm]	3

After plastication, but before entering the runner system, usual values of fiber length are in the 2- 3mm range. Thus, the initial length was set to mm. Thickness-averaged fiber length was sampled at the entry of the runner system (R) and at 27mm (A), 54mm (B) and 81mm (C) from the gate.

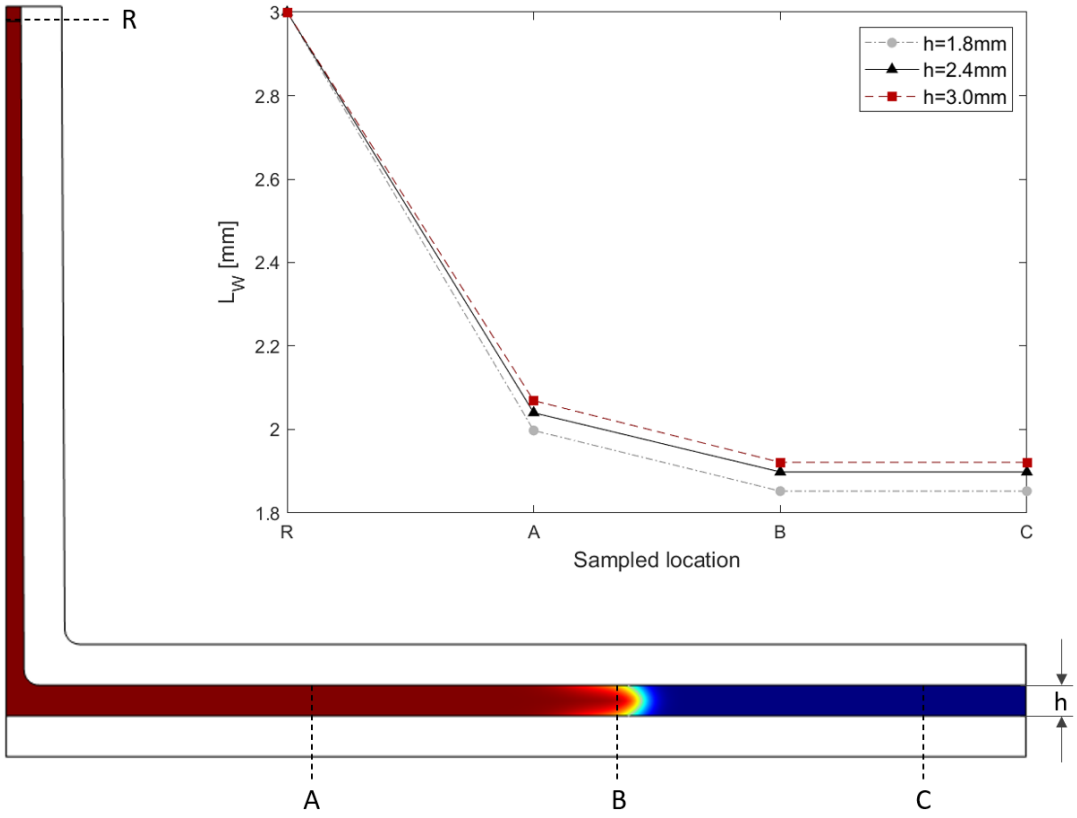

Figure 4.12 Left, 2D view of partial mold filling. Right, average fiber length along mold cavity

Figure 4.12 shows partial filling of the mold and the sampled locations. As expected, most damage occurs in the runner due to the high stresses and presence of longer fibers. Inside of the cavity however, there is little damage, and the fiber length soon reaches and equilibrium value. The change in mold thickness impacts the fiber length as the overall stress increases when the thickness is reduced.

The next step in the simulation efforts is optimizing the model parameters with respect to an actual molded component. This is necessary since the formulation of the model and subsequent parameter optimization were done employing the matrix viscosity η_m. It is understood that changes in fiber length, fiber orientation and fiber concentration all influence the viscosity and flow behavior during mold filling. However, these variables are often modeled independently due to the high computational cost

required to calculate the interaction between them. More importantly, the interaction between these three variables and the viscosity is still an open topic of research.

Since the viscosity model parameters used in simulation software are determined empirically, the flow behavior differs when using η_m and η_s. This means that a final necessary step in the model development is the parameter optimization employing the real flow found during mold filling.

Standard geometry plaques molded with PPGF20 from previous studies (see section 3.5), were used as reference for this analysis. The fiber length was measured in the purge material and in three location along the flow length. Figure 4.13 presents the plaque geometry and sampled locations.

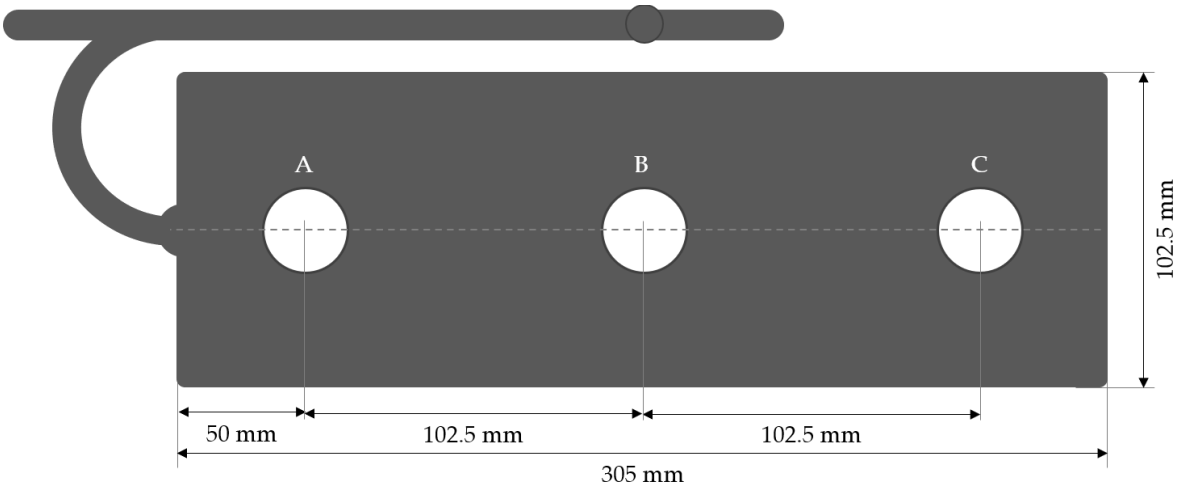

Figure 4.13 Illustration of the plaque geometry and illustration of the sample locations for fiber length analysis

Figure 4.14 shows the results of the fiber length measurement. Again, most damage occurs in the runner system and at the gate. In this case no change in average fiber length was detected in the cavity. Unfortunately, this fact makes it difficult to use these moldings to perform the parameter optimization analysis. However, they are useful to explore some features of the model in conjunction with the flow solver.

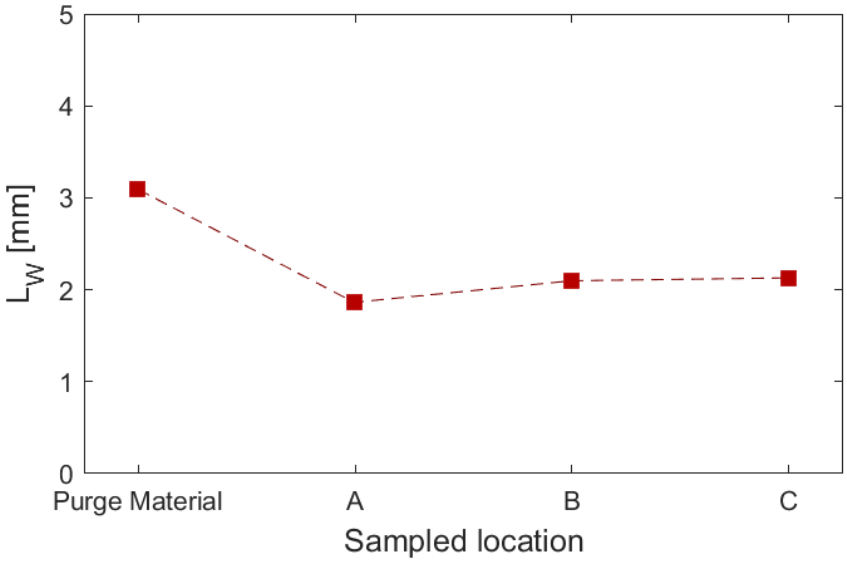

Figure 4.14Fiber length measured along the mold cavity

A 2D isothermal mold filling simulation was performed following the processing conditions listed in Table 3.7. To reduce computation, only the section limited by locations A and C was studied. The average fiber length L_W measure in location A was used as the initial condition for the attrition model. Sampled location A is close enough to the gate region that entry effects still dictate the fiber microstructure. However, for this exercise it is assumed that a fully developed core-shell structure is present at such location. This allows us to use the fiber length distribution measured experimentally as the Dirichlet condition for the inlet boundary as shown in Figure 4.15.

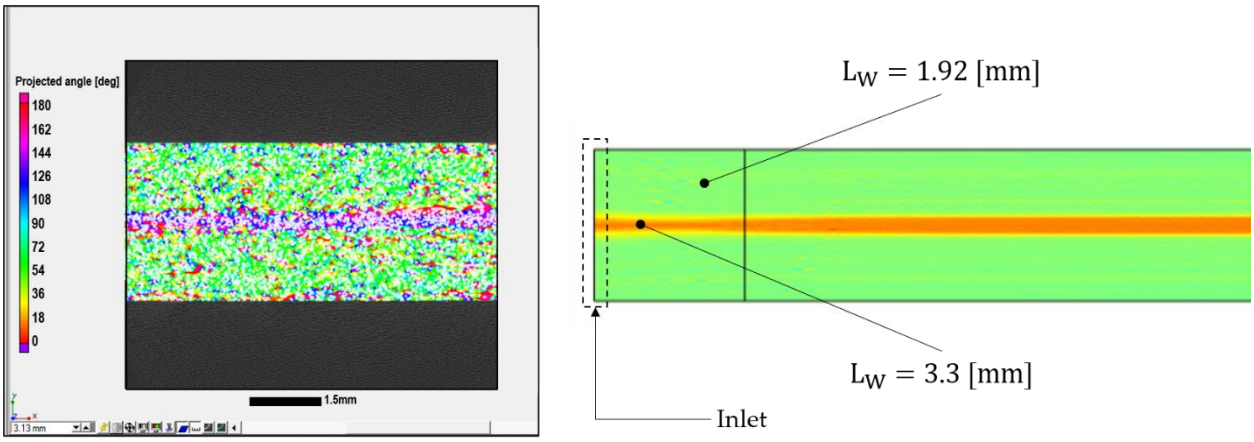

Figure 4.15 Left, μCT orientation analysis. Right, boundary condition for fiber breakage model

Figure 4.16 shows a 2D contour plot of L_W for a sequence of filling times. It can be seen how the long fibers in the core travel nearly unharmed until the flow front; where the fountain flow effect (caused by the No-slip condition) deposits them near the mold wall where stresses are higher and damage increases. There is an accumulation of long fibers at the flow front which could be caused by the fluid's deacceleration near the interface with the air. This phenomenon has been observed in actual moldings where usually high fiber length is found at the end of the cavity [37, 60].

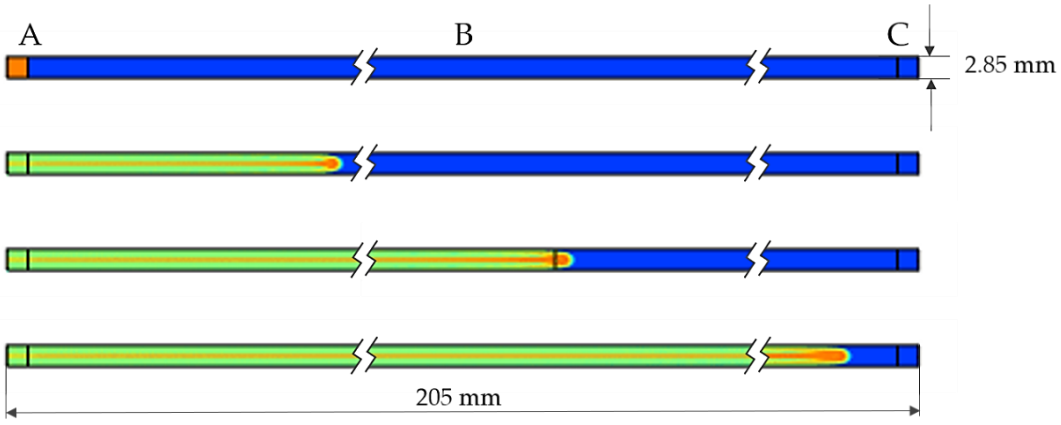

Figure 4.16 Fiber length surface plot for mold filling sequence

Finally, Figure 4.17 presents the fiber length averaged through the thickness of the cavity for locations A, B and C. The fiber length is plotted against filling time. Therefore, L_W is zero until the melt reaches the sampled location. Then, a spike in fiber length is

measured as the flow front with long fibers passes through. And finally, the fiber length decays until reaching a constant value. From the measurements presented in Figure 4.14, we know there is no change in fiber length between the sampled locations. Since the is no change in length, the parameter λ was fitted until all three curves converged to the same value after 2s of filling time.

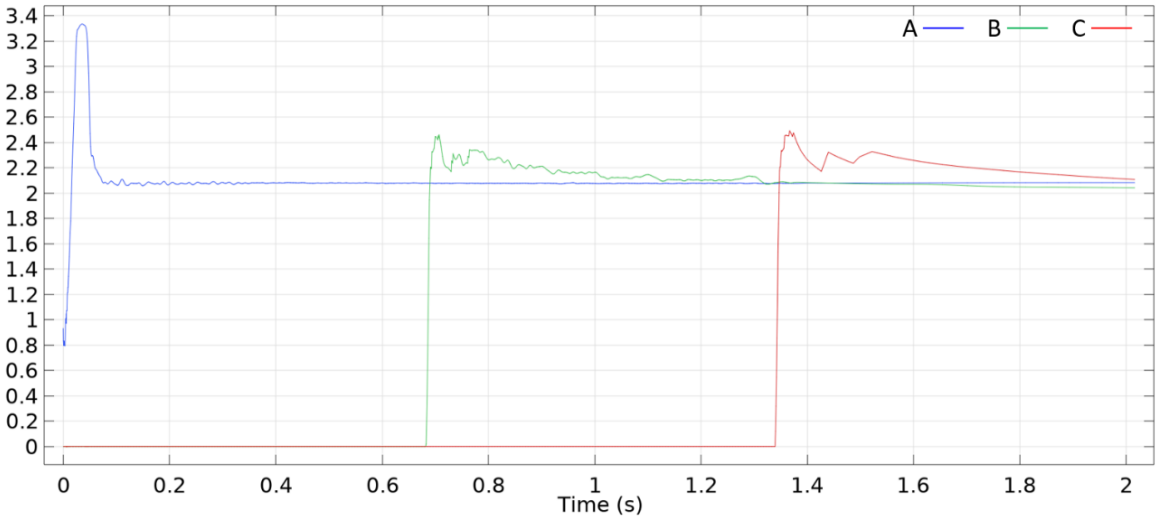

Figure 4.17 Average fiber length as function of filling time for location A, B and C

The value determined experimentally with the Couette rheometer ($\lambda = 0.125$) was used for the initial iteration, which resulted in overpredicted fiber damage. The parameter was slowly incremented until the fiber length matched the experimental value, resulting in $\lambda = 0.873$. The attrition rate coefficient k_f was not considered in this study since no overall change in fiber length occurred in the cavity.

4.4 Conclusions

Fiber breakage under simple shear experiments were conducted employing a Couette rheometer. Fiber Concentration, rate of deformation and viscosity are all factors that impact the kinetics of fiber breakage. Based on the experimental observations a continuum approach is developed to predict the fiber length averages L_N and L_W. A

model for the equilibrium length (L_∞) is deduced, using the concept that fibers break by bending under hydrodynamically-induced forces and fiber-fiber interactions. The breakage rate coefficient (k_f) is associated to fiber motion and therefore modeled proportional to the rate of deformation. Finally, both length averages are used to recover the fiber length distribution employing a Weibull or log-normal PDF.

Some of our experimental results contradict previous assertions on the role fiber-fiber interactions play on the overall phenomena of fiber breakage. Bailey and kraft observed an increase in fiber length with a 20%wt increment in fiber concentration in moldings with PA66 and PP, while von Turkovich et al. concluded fiber concentration had no impact on fiber damage. By using a Couette device to impose simple shear on the suspension our work looks to remove the complexities present during molding and extrusion processes, allowing us to isolate the role that individual factors have on fiber breakage.

There are similarities between the model we have developed, and the approach of Phelps et al. implemented in most molding simulation software. In their work, they derive an unbreakable length, L_∞ (or L_{ub}):

$$L_\infty = \left[\frac{\pi^3 E_f d_f^4}{4\zeta\, \eta_m\, \dot{\gamma}}\right]^{\frac{1}{4}} \qquad 4.11$$

Where ζ is the dimensionless drag coefficient and is used as a fitting parameter. This expression represents an equilibrium between internal resistance of the fiber ($E_f d_f$) and external stresses ($\eta_m\, \dot{\gamma}$), as does our expression(Equation 4.6). However, we assign more weight to the product $\eta_m\, \dot{\gamma}$ on account of the exponent ½ versus ¼ in their model. In their model, the overall rate of reduction of fiber length scales with $C_B \dot{\gamma}$, which is equivalent to our expression $k_f = \xi\dot{\gamma}$. Furthermore, the value obtained for ξ after fitting k_f to the Couette results falls within the range suggested for C_B in previous work [60, 86].

Reducing the number of fitting parameters introduced when developing a model is beneficial since this makes the approach more general and potentially reduces the number of experiments needed to determine such parameters [91]. In this case we achieve this by modeling L_N and L_W independently, each constitutive equation has its set of two fitting parameters that are determined from the experimental data. Additionally, a single length measurement provides data for both sets of model parameters.

In order to do a proper parameter optimization for the filling simulations, moldings with a clear drop in fiber length inside the cavity are needed. Additionally, to evaluate the effect of fiber content on the attrition behavior, such moldings should be performed with various nominal fiber concentrations.

5 Summary

This dissertation presented a fundamental analysis of process-induced fiber damage during LFT processing, with the main goal of developing a modeling approach for this variable. The work focused on two tasks: i) to understand which factors play a role on fiber attrition kinetics and to quantify such impact experimentally, and ii) to develop a model to predict fiber breakage based on material properties and processing conditions.

Chapter 3 focuses on experimental studies aimed to analyze the internal material state and the external conditions that provoke material failure. The unit of analysis, the fiber, is characterized and its strength is quantified to build a fiber failure threshold. Through extensive experimental work employing the Couette rheometer, different stages of the attrition kinetics are studied and correlated to the materials and the process. Additionally, the impact of fiber dispersion on the attrition kinetics was explored. Finally, a novel method to measure fiber length through the thickness of injection molded parts is developed.

Based on key observations from the experimental work, in Chapter 4 a model for predicting fiber length degradation is constructed. The kinetic of the phenomena is divided in steady state and dynamic change. The steady state formulation is deduced from a balance between the fiber's strength and the hydrodynamic drag. The dynamic change is associated to fiber motion under a shearing flow as observe by various researchers. The resulting state equation is validated versus experimental data and implemented in a mold filling simulation using COMSOL Multiphysics.

5.1 Recommendations for future work

Some simulation efforts have been presented as part of the work for this dissertation. However, a key step in the implementation of the fiber breakage model in simulation software is the validation of the prediction in actual molded components. For this, injection molded plaques with varying fiber concentrations and mold thicknesses will be molded. The plastication should be done as carefully as possible so most damage to the fibers occurs inside of the cavity during filling. In this manner, the measured length in the cavity will provide useful data to evaluate both fitting parameters $\lambda(\phi)$ and ξ.

Exploratory studies were performed on the interaction between dispersion and fiber damage for coated pellets. The initial results show interesting behavior; thus, additional repetitions should be performed to have reliable results. Additional factors such as the pellet fabrication method and the nominal fiber concentration should be explored. The information obtained from these studies can help link both fiber breakage and fiber dispersion in the plastication unit where most of the fiber damage occurs.

The Couette rheometer is an excellent tool to study the kinetic of fiber dispersion. As it was done with fiber length a full DOE still needs to be completed in order to determine the impact the main process and material parameter have on the dispersion rate. Important factors that need to be studied are the rate of deformation, temperature, and bundle shape effects.

5.2 Publications

The following articles have been submitted for publication as a result of the research on modeling and simulation of fiber configuration:

- Simon, Sara A.; Bechara Senior, Abrahán; Osswald, Tim. 2020. "Experimental Validation of a Direct Fiber Model for Orientation Prediction" J. Compos. Sci. 4, no. 2: 59. https://doi.org/10.3390/jcs4020059
- Senior, Abrahán B.; Osswald, Tim. 2020. "Measuring Fiber Length in the Core and Shell Regions of Injection Molded Long Fiber-Reinforced Thermoplastic Plaques" J. Compos. Sci. 4, no. 3: 104. https://doi.org/10.3390/jcs4030104
- Chang, Tzu-Chuan; Bechara Senior, Abrahán; Celik, Hakan; Brands, Dave; Yanev, Angel; Osswald, Tim. 2020. "Validation of Fiber Breakage in Simple Shear Flow with Direct Fiber Simulation" J. Compos. Sci. 4, no. 3: 134. https://doi.org/10.3390/jcs4030134
- Susanne K. Kugler, Abrahán Bechara, Héctor Pérez, Camilo Cruz, Armin Kech and Tim A. Osswald. "Data Enriched Lubrication Force Modeling for a Mechanistic Fiber Simulation for Short Fiber-reinforced Thermoplastics" Physics of Fluids [Accepted]
- Bechara, S. Goris, A. Yanev, D. Brands, T.A. Osswald. "Novel modeling approach for fiber breakage during molding of long fiber-reinforced thermoplastics" Physics of Fluids [Under internal review]
- Bechara, A.; Kollert, S.; Onken, J.; Ramirez, D.; Osswald, T.: "Effect of Fountain Flow on Fiber Orientation and Distribution in Fiber Filled Polymers During Mold Filling" Proceedings of the SPE Annual Technical Conference, Las Vegas, NV, 2014

6 References

[1] I. C. on C. Transportation, "https://theicct.org/chart-library-passenger-vehicle-fuel-economy," 2020. .

[2] C. T. Herakovich, *Mechanics of Fibrous Composites*, 1st ed. JohnWiley & Sons, Inc, 1998.

[3] T. A. Osswald, U. Ghandi, and S. Goris, *Discontinous Fiber Reinforced Composites*, 1st ed. Carl-Hanser Verlag, 2020.

[4] J. A. Y. H. Phelps, "Processing-Microstructure models for short- and long-fiber thermoplastic composites," University of Illinois at Urbana-Champaign, 2009.

[5] H. Ning, N. Lu, A. A. Hassen, K. Chawla, M. Selim, and S. Pillay, "A review of Long fibre thermoplastic (LFT) composites," *Int. Mater. Rev.*, vol. 6608, pp. 1–25, 2019.

[6] H. Kishi, N. Nakao, S. Kuwashiro, and S. Matsuda, "Carbon fiber reinforced thermoplastic composites from acrylic polymer matrices: Interfacial adhesion and physical properties," *Express Polym. Lett.*, vol. 11, no. 4, pp. 334–342, 2017.

[7] P. Zhang, Z. Huang, and G. Wang, "Preparation and properties of carbon fiber chiral materials," *J. Wuhan Univ. Technol. Mater. Sci. Ed.*, vol. 23, no. 4, pp. 510–512, 2008.

[8] E. Witten, T. Kruas, and M. Kühnel, "Composites Market Report 2016," *Ind. Verstärkte Kunststoffe*, no. September, pp. 1–46, 2016.

[9] R. Bailey and H. Kraft, "1987-A study of fibre attrition in the processing of long fibre reinforced thermoplastics.pdf," *Int. Mater. Rev.*, vol. 2, no. 2, pp. 94–101, 1987.

[10] J. L. Thomason and M. A. Vlug, "Influence of fibre length and concentration on the properties of glass fibre-reinforced polypropylene: 4. Impact properties," *Compos. Part A Appl. Sci. Manuf.*, vol. 28, no. 3, pp. 277–288, 1997.

[11] T. Vu-Khanh, J. Denault, P. Habib, and A. Low, "The effects of injection molding on the mechanical behavior of long-fiber reinforced PBT/PET blends," *Compos. Sci. Technol.*, vol. 40, no. 4, pp. 423–435, 1991.

[12] V. K. Stokes, L. P. Inzinna, E. W. Liang, G. G. Trantina, and J. T. Woods,

"Phenomenological study of the mechanical properties of long-fiber filled injection-molded thermoplastic composites," *Polym. Compos.*, vol. 21, no. 5, pp. 696–710, 2000.

[13] K. K. Chawla, *Composite materials science and engineering*, vol. 20, no. 3. 1989.

[14] G. J. von Bradsky, R. S. Bailey, A. J. Cervenka, H. . Zachman, and P. S. Allan, "Characterization of finite length composites: Part IV. Structural studies on injection moulded composites," *Pure Appl. Chem.*, vol. 69, pp. 2523–2539, 1997.

[15] B. lauke Shao Yun Fu, *Science and engineering of short fibre reinforced polymer composites*, 1st ed. Woodhead Publisher, 2009.

[16] J. L. Thomason, M. A. Vlug, G. Schipper, and H. G. L. . Krikor, "nfluence of fibre length and concentration on the properties of glass fibre-reinforced polypropylene: Part 3. Strength and strain at failure.," *Compos. Part A Appl. Sci. Manuf.*, vol. 27, no. 11, pp. 1075–1084, 1996.

[17] J. L. Thomason, "The influence of fibre length, diameter and concentration on the impact performance of long glass-fibre reinforced polyamide 6,6.," *Compos. Part A Appl. Sci. Manuf.*, vol. 40, no. 2, pp. 114–124, 2009.

[18] K. Shon, D. Liu, and J. L. White, "Experimental studies and modeling of development of dispersion and fiber damage in continuous compounding," *Int. Polym. Process.*, vol. 20, no. 3, pp. 322–331, 2005.

[19] J. H. Phelps, A. I. Abd El-Rahman, V. Kunc, and C. L. Tucker, "A model for fiber length attrition in injection-molded long-fiber composites," *Compos. Part A Appl. Sci. Manuf.*, vol. 51, pp. 11–21, 2013.

[20] G. H. Elmar Moritzer, "FIBER LENGTH DEGRADATION OF GLASS FIBER REINFORCED POLYPROPYLENE DURING SHEARING," in *SPE ANTEC*, 2016, pp. 647–651.

[21] S. Goris *et al.*, "Experimental study on fiber attrition of long glass fiber-reinforced thermoplastics under controlled conditions in a couette flow," in *Annual Technical Conference - ANTEC, Conference Proceedings*, 2017, vol. 2017-May.

[22] A. Salinas and J. F. T. Pittman, "Bending and Breaking Fibers in Sheared Suspensions," *Polym. Eng. Sci.*, vol. 21, no. 1, pp. 23–31, 1981.

[23] M. M. Rueda *et al.*, "Rheology and applications of highly filled polymers: A review of current understanding," *Prog. Polym. Sci.*, vol. 66, pp. 22–53, 2017.

[24] W. H. Herschel and R. Bulkley, "Konsistenzmessungen von Gummi-Benzollösungen," *Kolloid-Zeitschrift*, vol. 39, no. 4, pp. 291–300, 1926.

[25] T. D. Papathanasiou and D. C. Guell, *Flow-Induced Alignment in Composite Materials*, 1st ed. Wodhead Publishing, 1997.

[26] A. Durin, P. De Micheli, J. Ville, F. Inceoglu, R. Valette, and B. Vergnes, "A matricial approach of fibre breakage in twin-screw extrusion of glass fibres reinforced thermoplastics," *Compos. Part A Appl. Sci. Manuf.*, vol. 48, no. 1, pp. 47–56, 2013.

[27] C. Pérez, "The use of a direct particle simulation to predict fiber motion in polymer processing," University of Wisconsin-Madison, 2016.

[28] M. M. H. Kuroda and C. E. Scott, "Initial dispersion mechanisms of chopped glass fibers in polystyrene," *Polym. Compos.*, vol. 23, no. 3, pp. 395–405, 2002.

[29] E. Lafranche, P. Krawczak, J. P. Ciolczyk, and J. Maugey, "Injection moulding of long glass fiber reinforced polyamide 66: Processing conditions/microstructure/flexural properties relationship," *Adv. Polym. Technol.*, vol. 24, no. 2, pp. 114–131, 2005.

[30] S. Goris, "Characterization of the Process-Induced Fiber Configuration of Long Glass Fiber-Reinforced Thermoplastics," 2017.

[31] R. S. Bay and C. L. Tucker, "Stereological measurement and error estimates for three-dimensional fiber orientation," *Polym. Eng. Sci.*, vol. 32, no. 4, pp. 240–253, Feb. 1992.

[32] S. Goris and T. A. Osswald, "Process-induced fiber matrix separation in long fiber-reinforced thermoplastics," *Compos. Part A Appl. Sci. Manuf.*, vol. 105, pp. 321–333, Feb. 2018.

[33] T. B. Nguyen Thi, M. Morioka, A. Yokoyama, S. Hamanaka, K. Yamashita, and C. Nonomura, "Measurement of fiber orientation distribution in injection-molded short-glass-fiber composites using X-ray computed tomography," *J. Mater. Process. Technol.*, vol. 219, pp. 1–9, May 2015.

[34] T. Baranowski *et al.*, "Local fiber orientation from X-ray region-of-interest computed tomography of large fiber reinforced composite components," *Compos. Sci. Technol.*, vol. 183, no. February, p. 107786, Oct. 2019.

[35] V. Kunc, B. Frame, B. N. Nguyen, C. L. Tucker, and G. Velez-Garcia, "Fiber length distribution measurement for long glass and carbon fiber reinforced injection molded thermoplastics," *SPE Automot. Compos. Div. - 7th Annu. Automot. Compos. Conf. Exhib. ACCE 2007 - Driv. Perform. Product.*, vol. 2, pp. 866–876, 2007.

[36] J. H. Phelps and C. L. Tucker, "An anisotropic rotary diffusion model for fiber

orientation in short- and long-fiber thermoplastics," *J. Nonnewton. Fluid Mech.*, vol. 156, no. 3, pp. 165–176, Feb. 2009.

[37] S. Goris, T. Back, A. Yanev, D. Brands, D. Drummer, and T. A. Osswald, "A novel fiber length measurement technique for discontinuous fiber-reinforced composites: A comparative study with existing methods," *Polym. Compos.*, vol. 39, no. 11, pp. 4058–4070, Nov. 2018.

[38] M. Teßmann, S. Mohr, S. Gayetskyy, U. Haßler, R. Hanke, and G. Greiner, "Automatic Determination of Fiber-Length Distribution in Composite Material Using 3D CT Data," *EURASIP J. Adv. Signal Process.*, vol. 2010, no. 1, p. 545030, Dec. 2010.

[39] P. Pinter, B. Bertram, and K. A. Weidenmann, "A Novel Method for the Determination of Fibre Length Distributions from µCT-data," *6th Conf. Ind. Comput. Tomogr.*, no. iCT, pp. 1–8, 2016.

[40] D. Salaberger, K. A. Kannappan, J. Kastner, J. Reussner, and T. Auinger, "Evaluation of Computed Tomography Data from Fibre Reinforced Polymers to Determine Fibre Length Distribution," *Int. Polym. Process.*, vol. 26, no. 3, pp. 283–291, Jul. 2011.

[41] A. Miettinen *et al.*, "Non-destructive automatic determination of aspect ratio and cross-sectional properties of fibres," *Compos. Part A Appl. Sci. Manuf.*, vol. 77, pp. 188–194, Oct. 2015.

[42] T. Köpplmayr *et al.*, "Influence of fiber orientation and length distribution on the rheological characterization of glass-fiber-filled polypropylene," *Polym. Test.*, vol. 32, no. 3, pp. 535–544, May 2013.

[43] P. A. Hessman, T. Riedel, F. Welschinger, K. Hornberger, and T. Böhlke, "Microstructural analysis of short glass fiber reinforced thermoplastics based on x-ray micro-computed tomography," *Compos. Sci. Technol.*, vol. 183, no. April, p. 107752, Oct. 2019.

[44] J. Kastner, B. Plank, and D. Salaberger, "High resolution X-ray computed tomography of fibre- and particle-filled polymers," in *18th World Conference on Nondestructuve Testing*, 2012, no. April, pp. 16–20.

[45] S. Goris, T. Back, A. Yanev, D. Brands, D. Drummer, and T. A. Osswald, "A novel fiber length measurement technique for discontinuous fiber-reinforced composites: A comparative study with existing methods," *Polym. Compos.*, vol. 39, no. 11, pp. 4058–4070, Nov. 2018.

[46] H. Wang, "Accurate length measurement of multiple cotton fibers," *J. Electron.*

Imaging, vol. 17, no. 3, p. 031110, Jul. 2008.

[47] I. Manas-Zloczower and D. L. Feke, *Dispersive Mixing of Solid Additives*. 2009.

[48] H. J. Wolf, "Screw plasticating of discontinuous fiber filled thermoplastic: Mechanisms and prevention of fiber attrition," *Polym. Compos.*, vol. 15, no. 5, pp. 375–383, 1994.

[49] P. Ren and G. Dai, "Fiber dispersion and breakage in deep screw channel during processing of long fiber-reinforced polypropylene," *Fibers Polym.*, vol. 15, no. 7, pp. 1507–1516, 2014.

[50] R. von Turkovich and L. Erwin, "Fiber fracture in reinforced thermoplastic processing," *Polym. Eng. Sci.*, vol. 23, no. 13, pp. 743–749, 1983.

[51] M. Rohde, A. Ebel, F. Wolff-Fabris, and V. Altstädt, "Influence of processing parameters on the fiber length and impact properties of injection molded long glass fiber reinforced polypropylene," *Int. Polym. Process.*, vol. 26, no. 3, pp. 292–303, 2011.

[52] A. Inoue, K. Morita, T. Tanaka, Y. Arao, and Y. Sawada, "Effect of screw design on fiber breakage and dispersion in injection-molded long glass-fiber-reinforced polypropylene," *J. Compos. Mater.*, vol. 49, no. 1, pp. 75–84, 2015.

[53] K. Kimura, Y. Itamochi, and H. Tomiyama, "The Evaluation of Mixing Characteristics of Dulmage Screw," *Adv. Mater. Res.*, vol. 747, pp. 769–772, Aug. 2013.

[54] D. O'Regan and M. Akay, "The distribution of fibre lengths in injection moulded polyamide composite components," *J. Mater. Process. Technol.*, vol. 56, no. 1–4, pp. 282–291, 1996.

[55] G. B. Jeffery, "The motion of ellipsoidal particles immersed in a viscous fluid," *Proc. R. Soc. London. Ser. A, Contain. Pap. a Math. Phys. Character*, vol. 102, no. 715, pp. 161–179, Nov. 1922.

[56] J.M. Burgers, "On the motion of small particles of elongated form supended in a viscous fluid," Delft, 1938.

[57] O. L. Forgacs and S. G. Mason, "Particle motions in sheared suspensions. X. Orbits of flexible threadlike particles," *J. Colloid Sci.*, vol. 14, no. 5, pp. 473–491, 1959.

[58] O. L. Forgacs and S. G. Mason, "Particle motions in sheared suspensions. IX. Spin and deformation of threadlike particles," *J. Colloid Sci.*, vol. 14, no. 5, pp. 457–472, 1959.

[59] S. H. Bumm, J. L. White, and A. I. Isayev, "Glass fiber breakup in corotating twin screw extruder: Simulation and experiment," *Polym. Compos.*, vol. 33, no. 12, pp. 2147–2158, 2012.

[60] J. H. Phelps, A. I. Abd El-Rahman, V. Kunc, and C. L. Tucker, "A model for fiber length attrition in injection-molded long-fiber composites," *Compos. Part A Appl. Sci. Manuf.*, vol. 51, pp. 11–21, Aug. 2013.

[61] H. Chen, M. Cieslinski, P. Wapperom, and D. G. Baird, "Long fiber (glass) breakage in capillary and contraction flow," *Annu. Tech. Conf. - ANTEC, Conf. Proc.*, no. 3, pp. 546–550, 2015.

[62] E. Moritzer and H. Gilmar, "Fiber Length Degradation of Glass Fiber Reinforced Polypropylene During Shearing," in *SPE ANTEC*, 2016, pp. 647–651.

[63] T. Sasayama, M. Inagaki, and N. Sato, "Direct simulation of glass fiber breakage in simple shear flow considering fiber-fiber interaction," *Compos. Part A Appl. Sci. Manuf.*, vol. 124, no. May, p. 105514, Sep. 2019.

[64] T.-C. Chang, A. Bechara Senior, H. Celik, D. Brands, A. Yanev, and T. Osswald, "Validation of Fiber Breakage in Simple Shear Flow with Direct Fiber Simulation," *J. Compos. Sci.*, vol. 4, no. 3, p. 134, Sep. 2020.

[65] Frederick T. Wallenberger and N. E. Weston, *Natural Fibers, Plastics and Composites*. 2004.

[66] S. Wang *et al.*, "An improved loop test for experimentally approaching the intrinsic strength of alumina nanoscale whiskers," *Nanotechnology*, vol. 24, no. 28, p. 285703, Jul. 2013.

[67] D. Sinclair, "A Bending Method for Measurement of the Tensile Strength and Young's Modulus of Glass Fibers," *J. Appl. Phys.*, vol. 21, no. 5, pp. 380–386, May 1950.

[68] S. Wang, Z. Shan, and H. Huang, "The Mechanical Properties of Nanowires," *Adv. Sci.*, vol. 4, no. 4, p. 1600332, Apr. 2017.

[69] P. K. Jarvela, "Bending strength and static fatigue of glass fibre in different atmospheres by fibre loop test," *J. Mater. Sci.*, vol. 19, no. 8, pp. 2481–2487, Aug. 1984.

[70] H. Pham, Ed., *Springer Handbook of Engineering Statistics*. London: Springer London, 2006.

[71] D. Gross, W. Hauger, J. Schröder, W. A. Wall, and J. Bonet, *Engineering Mechanics 2*. Berlin, Heidelberg: Springer Berlin Heidelberg, 2018.

[72] A. Öchsner, *Theorie der Balkenbiegung*. Wiesbaden: Springer Fachmedien Wiesbaden, 2016.

[73] Horst Werkle, *Finite Elemente in der Baustatik*. Wiesbaden: Vieweg, 2008.

[74] J. M. G. Stephen P. Timoshenko, "Theory_of_elastic_stability_by_S._Timoshenko_and_J.M._Gere__1963_.pdf." p. 280, 1961.

[75] SABIC, "Processing guides: SABIC STAMAX," 2016.

[76] K. Shon, D. Liu, and J. L. White, "Experimental Studies and Modeling of Development of Dispersion and Fiber Damage in Continuous Compounding," *Int. Polym. Process.*, vol. 20, no. 3, pp. 322–331, Sep. 2005.

[77] V. B. Gupta, R. K. Mittal, P. K. Sharma, G. Mennig, and J. Wolters, "Part I : Reduction in Fiber Length During Processing," *Polym. Compos.*, no. 1, pp. 8–15, 1989.

[78] G. J. von Bradsky, R. S. Bailey, A. J. Cervenka, H. G. Zachmann, and P. S. Allan, "Characterization of finite length composites: Part IV - Structural studies on injection moulded composites (Technical Report)," *Pure Appl. Chem.*, vol. 69, no. 12, pp. 2523–2540, Jan. 1997.

[79] S. Toll and P.-O. Andersson, "Microstructure of long- and short-fiber reinforced injection molded polyamide," *Polym. Compos.*, vol. 14, no. 2, pp. 116–125, Apr. 1993.

[80] R. Bailey and H. Kraft, "A Study of Fibre Attrition in the Processing of Long Fibre Reinforced Thermoplastics," *Int. Polym. Process.*, vol. 2, no. 2, pp. 94–101, Nov. 1987.

[81] D. O'Regan and M. Akay, "The distribution of fibre lengths in injection moulded polyamide composite components," *J. Mater. Process. Technol.*, vol. 56, no. 1–4, pp. 282–291, Jan. 1996.

[82] B. N. Nguyen *et al.*, "Fiber Length and Orientation in Long-Fiber Injection-Molded Thermoplastics — Part I: Modeling of Microstructure and Elastic Properties," *J. Compos. Mater.*, vol. 42, no. 10, pp. 1003–1029, May 2008.

[83] R. S. Bay and Charles L Tucker, "Fiber Orientation in Simple Injection Moldings . Part II : Experimental Results," *Polym. Compos.*, vol. 13, no. 4, pp. 332–341, 1992.

[84] T. A. Osswald and G. Menges, "Material Science of Polymers for Engineers," in *Materials Science of Polymers for Engineers*, 3rd ed., München: Carl Hanser Verlag GmbH & Co. KG, 2012, pp. I–XIX.

[85] J. H. Phelps, "Processing-Microstructure Models for Short- and Long-Fiber Thermoplastic Composites," University of Illinois at Urbana-Champaign, 2009.

[86] M. R. Kantz, H. D. Newman, and F. H. Stigale, "The Skin-Core Morphology and Structureproperty Relationships in Injection-Molded Polypropylene," *J. Appl. Polym. Sci.*, vol. 16, pp. 1249–1260, 1972.

[87] C. L. Tucker III and E. Liang, "Stiffness predictions for unidirectional short-fiber composites: Review and evaluation," *Compos. Sci. Technol.*, vol. 59, no. 5, pp. 655–671, Apr. 1999.

[88] S. V. Lomov, Y. Abdin, and A. Jain, "Mori-tanaka methods for micromechanics of random fibre composites," *ICCM Int. Conf. Compos. Mater.*, vol. 2015-July, no. August, 2015.

[89] G. P. Tandon and G. J. Weng, "The effect of aspect ratio of inclusions on the elastic properties of unidirectionally aligned composites," *Polym. Compos.*, vol. 5, no. 4, pp. 327–333, Oct. 1984.

[90] B. Nghiep Nguyen, S. K. Bapanapalli, V. Kunc, J. H. Phelps, and C. L. Tucker, "Prediction of the Elastic—Plastic Stress/Strain Response for Injection-Molded Long-Fiber Thermoplastics," *J. Compos. Mater.*, vol. 43, no. 3, pp. 217–246, Feb. 2009.

[91] F. Dyson, "A meeting with Enrico Fermi.," *Nature*, vol. 427, no. 6972, p. 297, Jan. 2004.